UNIVERSITY OF CALIFORNIA
SANTA CRUZ

INTEGRATED OPTOFLUIDIC PLATFORM FOR HIGH THROUGHPUT BIOMOLECULE DETECTION AND MANIPULATION

A dissertation submitted in partial satisfaction
of the requirements for the degree of

DOCTOR OF PHILOSOPHY

in

ELECTRICAL AND
COMPUTER ENGINEERING

by

Mohammad Julker
Neyen Sampad

June 2024

The Dissertation of Mohammad Julker Neyen Sampad is approved:

_____
Professor Holger Schmidt, Chair

_____
Professor Nobuhiko Kobayashi

_____
Professor Shiva Abbaszadeh

_____
Peter Biehl

Vice Provost and Dean of Graduate Studies

Table of Contents

List of Figures

List of Tables

Abstract

Mohammad Julker Neyen Sampad

Integrated optofluidic platform for high throughput biomolecule detection and manipulation

Recent outbreaks of infectious diseases underscore the urgent need for ultrasensitive, high-throughput, and versatile sensors to diagnose and contain them at their early stage, thereby mitigating their immense threat to public health and preventing disruption to social and economic growth worldwide. Optofluidic biosensors can offer highly sensitive single molecule detection and precise particle manipulation by combining optics with microfluidics in a single platform. A specially designed anti-resonant reflecting optical waveguide (ARROW) based optofluidic platform offers compatibility for enabling optical interaction with biomarkers and small molecules in their native low-refractive index fluidic environment. Further integration with highly selective bioassays, electronics, and signal processing techniques can improve the performance of these platforms. The goal of this thesis is to develop integrated optofluidic platforms for low complexity, remote-controllable, high-throughput, and ultrasensitive biosensing at clinically relevant biomarker concentrations. First, we explore the potential of integrating programmable fast electronics such as field programmable gate array (FPGA) for enhancing detection throughput of the MMI waveguide-based ARROW optofluidic platform. With this framework, salient experimental parameters such as target concentration and detection rate are extracted

in real-time, demonstrating a highly accurate (99%) detection scheme with fluorescent nanobeads covering the entire clinically relevant range (femto to attomolar) of particle concentrations. Subsequent validation with real-time fluorescence detection of single bacterial plasmid DNA at attomolar concentrations indicates the platform's potential as a point-of-care diagnostic tool. Next, a cloud-based, Internet of Things (IoT)-enabled polydimethylsiloxane (PDMS) optofluidic platform is demonstrated for the remote operation of automated bio sample preparation and detection. This platform offers a user-friendly and intuitive workflow for on-chip liquid handling and serves as a valuable collaboration and training tool for remote access from anywhere across the globe. The rest of my thesis will discuss solid-state nanopores, essentially nanoscopic holes in thin insulated membranes, as label-free single-molecule analysis tools integrated with the optofluidic platform. When combined with a modified solid-phase extraction (SPE) bioassay, the platform offers specificity and amplification-free rapid biomarker quantification at ultra-low concentrations. The optofluidic platform allows optical trapping of target-enriched microbeads near the nanopore detector, followed by a thermal release assisting the electrophoretic target capture process. This optical trapping enhanced nanopore capture rate enhancement (TACRE) process demonstrates ~2000x enhancement factor compared to the diffusion-limited nanopore capture process. Also, this high-throughput method enabled the successful detection of SARS-CoV-2 RNAs from human nasopharyngeal swabs covering entire clinically relevant concentrations. Next, this method was modified to detect Zika and SARS-CoV-2 RNAs from non-human primate biofluids in a longitudinal infection study. This direct

detection method demonstrates qRT-PCR-like performance without requiring any intermediate complex bioreactions. The versatility of the TACRE assay in analyzing six different types of biofluids and the practicality of this platform as a sensitive molecular diagnostic tool are also manifested. Finally, the integrated nanopore-optofluidic platform was utilized to characterize organoid-derived exosomes, an important biomarker for monitoring intercellular communication. This thesis concludes with a report on another application of the high-throughput and sensitive TACRE platform in monitoring the ENO-1 gene marker, a key regulatory enzyme in glycolysis, from organoid-derived exosome cargo, showing promise for further application in the clinical evaluation of cell growth and health in cell culture.

To my parents late Dr. Joaherul Islam and Dr. Farida Yeasmin.

As well as to Salina Islam (abla), Bazlur Rashid Litu (tow), late Eng. Abdur Razzaque (kaku), and Sultana Nasrin EP kaki.

Acknowledgements

This work and my journey through my PhD program have reached fruition thanks to the unwavering support and insightful discussions of many individuals.

First and foremost, I express my deepest gratitude to my supervisor, Professor Holger Schmidt, whose continuous support, guidance, and encouragement have been invaluable throughout my studies. I thank him for being the driving force and role model throughout my graduate study, pushing me towards becoming a better researcher.

I extend my thanks to Professor Aaron Hawkins and his group for their dedication to fabricating and enhancing the devices used in my research. I am also grateful to Professor Jean Patterson for her support with the infected non-human primate samples. Special appreciation goes to the Braingeneers group, particularly Professor David Haussler, Professor Sofie Salama, Professor Mircea Teodorescu, and Dr. Mohammed Mostajo-Radji, for their insightful discussions, feedback, and contributions to the advancement of my work.

I owe a debt of gratitude to my first mentor, Dr. Md. Mahmudur Rahman, and I look forward to future collaborations in "vai-brother business". I would like to express my gratitude to Dr. Han Zhang for being an excellent friend, colleague, and a great mind to discuss with. I can’t say enough about the support and help I have received from Dr. Tom Yuzvinisky. It has been my pleasure to work with S. M. Saiduzzaman Abir, a great mind and young researcher. Special thanks to my long-term friend- Ayemon Baraka, Arafat Kabir Sun, and Rakibul Islam Chowdhury Shimanto for our long phone

call discussions ranging from electronics to life issues. I have learned many things from my fellow lab mates over my grad life, special mentions to Dr. Gopikrishnan Gopalakrishnan Meena, (soon to be Dr.) Md. Nafiz Amin Aditya, Dr. Alexandra Stambaugh, Dr. Vahid Ganjalizadeh, Dr. Tyler Sano, Horace Zhang. I had the opportunity to collaborate with Dr. Zach Walker, Tanner Wells, Spencer Seiler, Matt Elliott, Quinn Brail, and Stephanie Mdaki. I am grateful to these great minds and researchers from whom I learned about diverse topics.

I would like to thank the current and previous members of the Applied optics group – Dr. Ruiting Xu, Sujung Kim, Ravipa Losakul, Zoë Weber-Porter, Helio Ramollari, Dr. Aadhar Jain, Dr. Weigang Yang, Dr. Jennifer Black, Dr. Cassidy Berk, Dr. Mike Jaris, Yucheng Li, Donguk Choi, Luis Bautista, for their collaboration, valuable discussion and creating a fun and friendly work environment.

I am grateful to the Bangladeshi community at UCSC, specially to my friend (local guardian) Sushmita Joardar, Mizanur Rahman, Sazia Anar, Reefat Inum, Kamrun Nahar Shushama. I will miss those late night jolsa and good homemade foods. I would always remember my good times at Santa Cruz west cliff, Rio Del Mar, Capitola, UCSC coastal science campus whether walking, running, riding my bicycle, or driving my car while listening to my “nanopore” special soundtrack.

Finally, and most importantly, I thank my mother for her endless love, worries and motivation to finish my degree. “The goat completed the race in a muddy racetrack after finishing all the blood”.

Chapter 1 Introduction

In recent decades, the world has witnessed the alarming impact of viral and bacterial pathogens on public health, leading to widespread pandemics [1], [2]. While vaccines and antibiotics have been pivotal in preventing and treating many infectious diseases, the emergence of new viral strains and antibiotic-resistant bacteria presents significant challenges [3], [4]. Most of the currently available viral and antibacterial strain detection methods target specific nucleic acid biomarkers [5]. While PCR is the current gold standard in this field for being highly specific and sensitive, it is complex and requires expensive reagents, central laboratory infrastructure, and well-trained personnel [6], [7]. This underscores the urgent need to develop new generations of portable diagnostic technologies with high sensitivity, speed, and accuracy.

Optofluidic devices could be the most promising solution, combining innovations in microfluidics and optical biosensing fields into a single chip-scale platform [8]–[10]. Among the optofluidic biosensors, ARROW-based platforms have shown efficient and amplification-free detection of single or multiplexed fluorescently tagged targets in clinical samples [11]–[13]. Although ARROW optofluidic devices are mostly used as a standalone optical biosensor, they can also be utilized for particle manipulation, i.e., size-based sorting, transportation, and trapping by exploiting optical forces [14], [15]. Moreover, the performance of these devices can be enhanced by integrating fast programmable electronics [16], [17], robust signal-processing algorithms [18], biofluid processing units [19], and other label-free single-molecule analysis techniques such as nanopores [20].

Primate models, including marmosets and baboons, provide invaluable insights into the progression of infections and are crucial for advancing vaccine research [21], [22]. Similarly, organoid 3D culture systems hold immense importance in various fields such as neuroscience and cancer research due to their ability to closely mimic the in vivo microenvironment, allowing for more accurate disease modeling, drug screening, and personalized medicine approaches [23], [24]. Integrating these integrated optofluidic diagnostic devices with these models can offer simple and non-invasive POC diagnostics, research tools for assisting in the development of these models, and many other fields.

This thesis describes five major research contributions that enhance the throughput and performance of the integrated optofluidic biomarker detection and biofluid processing platforms. The platforms target sensitive bacterial (E. Coli), viral (SARS-CoV-2, Zika), and exosome biomarker detection for point of care molecular diagnosis at clinical concentrations. The organization of this thesis follows accordingly: chapters 2 to 4 will concentrate on different programmable electronics integration to optofluidic single molecule detection for enhanced performance and better accessibility, and chapters 5 to 8 discuss how optofluidic particle manipulation schemes can be integrated with a solid-state nanopore based label-free single molecule detection process to increase its throughput and lower the limit of detection.

Chapter 2 will cover the basic working principle of ARROW waveguides and MMI waveguides for optofluidic biosensing. Then a brief description of silicon and PDMS based optofluidic platform fabrication will be provided. The chapter will end with a

brief introduction to the pneumatically controlled PDMS microvalves based sample preparation platform, which facilitates contamination-free particle delivery to the optical sensing region. Chapter 3 describes a field programmable gate array (FPGA) integrated optofluidic platform to enable live on-chip monitoring of single particle fluorescence analysis at high accuracy. This chapter shows real-life application of this rapid sample-to-answer scheme for detecting single antibacterial resistance genes at attomolar concentration in amplification-free manner. Chapter 4 shows a cloud-based internet enabled PDMS microfluidic sample preparation platform that can automatize fluorescent labeling and sample manipulation on a single chip for optical biomarker detection. Being integrated with IoT, this platform can be easily accessed from a remote location and an intuitive and user-friendly operation was achieved by designing a custom programming language. Finally, this powerful IoT controlled microfluidic system was then utilized as a project-based learning tool for training underserved Hispanic students in Bolivia in initial concepts of computer programming. Chapter 5 will first introduce the optofluidic particle manipulation schemes and experimental design for on-chip particle pre-concentration implementation. Then, the working principle of nanopore biosensing, and integration with existing optofluidic platforms will be demonstrated. Chapter 6 covers optical trapping-assisted label-free and amplification-free detection of SARS-CoV-2 RNAs covering the clinically relevant concentration range. This scheme combines magnetic bead based specific nucleic acid extraction and optical target enriched microbead delivery to the nanopore sensing region for high-throughput purely electrical single molecule counting. This method

showed 2000x detection rate enhancement compared to conventional diffusion limited nanopore capture process. In chapter 7, this optical assisted enhanced nanopore detection was utilized for sensitive detection of Zika and SARS-CoV-2 viral RNAs from infected non-human primate models. For a superior performance, a 20μm long particle isolation region was added to the microfluidic channel for isolating optically trapped microbeads and a 300nm thin nanomembrane was selectively fabricated on the chamber for easier nanopore integration. Two separate month long longitudinal viral load monitoring studies with this direct and calibration-free optofluidic-nanopore platform showed comparable performance to the gold standard qRT-PCR method even without any amplification step. Finally, chapter 8 will focus on another type of biomarker, organoid derived exosome for liquid biopsy. The chapter will first cover whole exosome detection from organoid culture media supernatant with a solid-state nanopore and then an enhanced detection of metabolic-gene, Enolase-1 from exosomal cargo. This demonstration illustrates the promising potential of integrated optofluidic-nanopore platform towards ultra-sensitive clinical diagnosis of biofluids.

Chapter 2 Background on optofluidic biosensor and PDMS microfluidic control device

This chapter will discuss the underlying principles of optofluidic biosensing and automatic microfluidic bio sample processing units. I will begin with a brief introduction of optofluidics and gradually proceed towards development of an Anti-Resonant Reflecting Optical Waveguide (ARROW) based optofluidic platform explaining its essential building blocks. Finally, a brief description of the working principle and fabrication steps of a PDMS based automatic microfluidic sample preparation device will be provided.

2.1 Optofluidics

Optics plays a pivotal role in the field of biomolecule analysis by enabling non-invasive and highly sensitive molecular characterization and quantification methods [25]. Optical sensing methods such as imaging, microscopy, spectroscopy etc. based on total internal reflection, absorption, fluorescence, scattering, wave interference are constantly being used across the world to probe the biomolecules of interest [26], [27]. Optical single molecule analysis (SMA) is valuable in understanding the biochemical and biophysical aspects of biological entities, ranging from DNA and proteins to more complex cellular structures [28]–[30].

Microfluidics, on the other hand, takes advantage of miniaturized systems and involves manipulating small volume fluids within microchannels [31]. Microfluidic techniques

allow sample purification, transportation, and mixing in a single enclosed platform, reducing the required sample and reagent volume and minimizing sample contamination [32], [33]. This introduces the idea of a lab-on-chip (LOC) system where it would be possible to automatically perform multiplexed laboratory chemical analysis on a small, inexpensive, portable, and disposable system using as little volume of biofluid as a single drop (~50µL) [34], [35].

Optofluidic technology integrates two powerful systems, optics and microfluidics, in a single platform offering biomolecule analysis in its native fluidic environment [8], [10], [36], [37]. A typical optofluidic platform combines microfluidic sample preparation and delivery methods with sensitive optical real-time monitoring techniques for rapid sample to answer scheme [19], [38]. Furthermore, these optofluidic platforms can be integrated with other technologies, such as fast and programmable electronics to increase throughput, modality, and accessibility [16], [17]. The versatility and simplicity of integrated optofluidic devices make them promising candidates for point-of-care testing and molecular diagnostic application [39].

2.2 Slab waveguide

A symmetric planar dielectric slab waveguide is the simplest optical waveguide that has been explored for optical biosensing and for making compact lab-on-chip devices. The waveguide structure is formed by sandwiching a thin film of higher refractive index dielectric material (core) between two semi-infinite regions of lower refractive index material (cladding)[40]. Fig. 2.1 shows a similar symmetric slab waveguide with

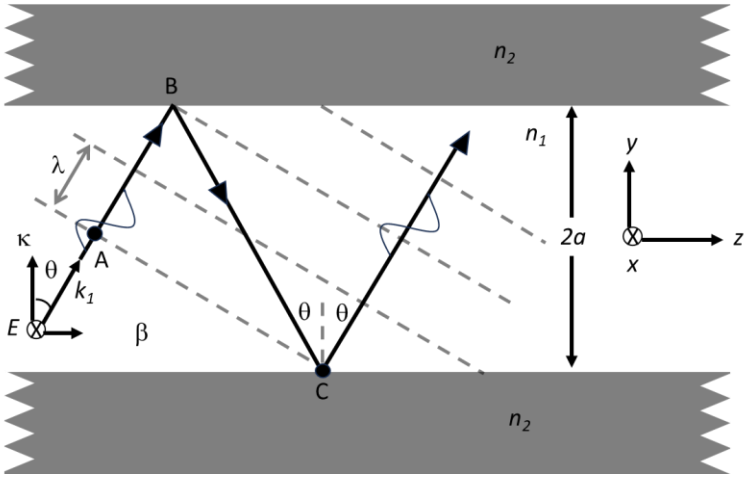

Fig. 2.1 Light propagation through a slab waveguide. (Adapted from [40].)

a core region of thickness $d = 2a$ and refractive index n_1, where the refractive index of the cladding region is n_2 $(n_1 > n_2)$. The light propagates along the length of the waveguide in a zig-zag fashion by the principle of total internal reflection (TIR) occurring at the dielectric interfaces. Efficient guiding of the coupled light inside the whole length of the waveguide requires constructive interference among the wavefronts of the light waves, otherwise the wave will be destroyed.

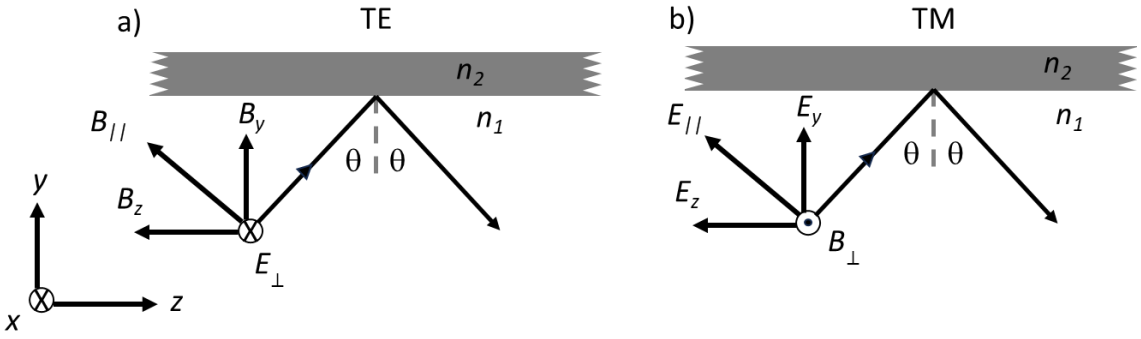

Fig. 2.2 a) Transverse electric field (TE) and b) transverse magnetic field (TM) modes. (Adapted from [40].)

For the symmetric planar slab waveguide, the condition for constructive interference inside the core layer can be calculated based on the incidence angle of the incoming

light ray $\boldsymbol{\theta}$, phase change between the incoming and the reflected wavefront $\boldsymbol{\phi}$ as shown in eq. 2.1.

$$\boldsymbol{k_1[2dcos\theta] - 2\phi = m(2\pi)} \tag{2.1}$$

where, $\boldsymbol{k_1 = 2\pi n_1/\lambda}$ is the wavevector inside the core with components $\boldsymbol{\beta = k_1 sin\theta}$ and $\boldsymbol{\kappa = k_1 cos\theta}$ along the parallel and transverse direction to the wave propagation, $\boldsymbol{\lambda}$ is the free space wavelength.

The eq. 2.1 shows that only a certain value of $\boldsymbol{\theta}$ can satisfy the constructive interference condition for a certain value of *m* (mode number, m = 0, 1, 2, …) and thus it can propagate along the waveguide. We can derive the waveguide condition in eq. 2.2, in which $\boldsymbol{\phi_m}$ is a function of $\boldsymbol{\theta_m}$.

$$\left[\frac{\boldsymbol{2\pi n_1(2a)}}{\boldsymbol{\lambda}}\right]\boldsymbol{cos\theta_m - \phi_m = m\pi} \tag{2.2}$$

Light is an electromagnetic wave with synchronized oscillations of electric and magnetic field, we can consider two of the various possible scenarios while the incident light interacts with the dielectric boundaries. First, the electric field of the light wave is perpendicular to the plane of incidence (fig. 2.2 a), namely Transverse Electric field (TE) mode, or the magnetic field of the light wave is perpendicular to the plane of incidence (fig. 2.2 b), namely Transverse Magnetic field (TM) mode. The phase change originating from the TIR event depends on the polarization of the field and the value is different between TE and TM mode for the same incidence angle. For the TE mode the expression of $\boldsymbol{\phi_m}$ can be written as-

$$\tan\left(\frac{\boldsymbol{\phi_m}}{\mathbf{2}}\right) = \frac{\left[\sin^2\boldsymbol{\theta_m} - \left(\frac{\boldsymbol{n_2}}{\boldsymbol{n_1}}\right)^2\right]^{\frac{1}{2}}}{\boldsymbol{cos\theta_m}} \tag{2.3}$$

2.2.1 Waveguide modes

The supported mode angles $\boldsymbol{\theta_m}$ for a slab waveguide must satisfy the TIR condition, i.e., $\sin\boldsymbol{\theta_m} > \boldsymbol{sin\theta_c}(=\frac{\boldsymbol{n_2}}{\boldsymbol{n_1}})$. So, it is possible to calculate the maximum value of mode number for a certain slab waveguide's geometrical parameter indicated in eq. 2.4.

$$\boldsymbol{m} \leq (\boldsymbol{2V} - \boldsymbol{\phi})/\boldsymbol{\pi} \tag{2.4}$$

$$\text{Where, } \boldsymbol{V} = \frac{\boldsymbol{2\pi a}}{\boldsymbol{\lambda}}\left(\boldsymbol{n_1^2} - \boldsymbol{n_2^2}\right)^{\frac{1}{2}} \tag{2.5}$$

So, a careful design of geometric parameters of the slab waveguide and a choice of refractive index difference between the core and cladding region can allow only a single mode propagation (m < 1) along the length of the waveguide.

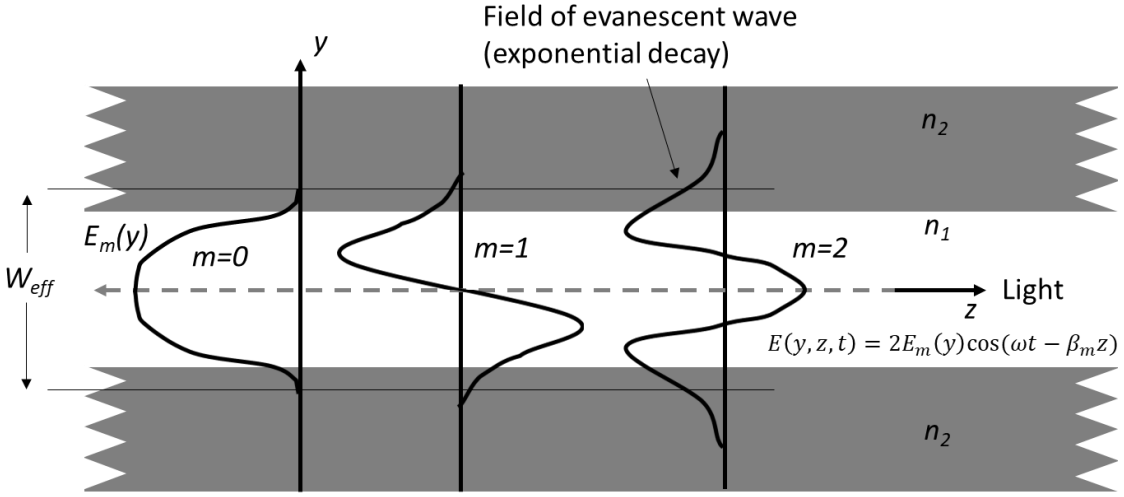

Fig. 2.3 Slab waveguide with mode field parameter. (Adapted from [40].)

A waveguide can allow multiple modes to propagate along the length of the waveguide as shown in eq. 2.4, and when two waves interfere constructively inside the waveguide, the resultant wave's electric field in the core can be written as –

$$E(y,z,t) = 2E_0 \cos\left(\kappa_m y + \frac{\phi_m}{2}\right) \cos\left(\omega t - \beta_m z + \frac{\phi_m}{2}\right) \quad (2.6)$$

$$E(y,z,t) = 2E_m(y) \cos\left(\omega t - \beta_m z + \frac{\phi_m}{2}\right) \quad (2.7)$$

The second part of the eq. 2.7 indicates the resultant wave that will travel along the z-axis while the first part of the equation indicates a standing wave pattern along the y axis. Fig. 2.3 shows the first three modes (m = 0, 1, 2) electric field distribution along the y axis while traveling along the waveguide with increased evanescent wave penetrating the cladding layer in the higher order mode.

2.3 Multimode interference waveguide

If a very wide waveguide is coupled with a single mode waveguide, the allowed modes inside the wider waveguide will interfere with each other and create well defined replica of the input beam at certain spots along the propagation direction. This forms the underlying principle of multimode interference (MMI) waveguide. For a symmetric input, the MMI pattern only depends on the waveguide dimension, and the incident light wavelength. It is possible to derive a general condition for designing MMI waveguide and a detailed analysis can be found in reference [41]. To briefly describe the MMI concept, we will first consider a step-index waveguide (refractive index of core and cladding equal to n_c and n_{cl} respectively) like the one shown in fig. 2.3 with width W and length L. The allowed number of lateral modes within this waveguide for

a coupled light beam with wavelength λ can be calculated using eq. 2.4 where the V-number will be-

$$V = \frac{W\pi}{\lambda}(n_c^2 - n_{cl}^2)^{\frac{1}{2}} \tag{2.8}$$

The relationship among the lateral wavenumber (k_{yv}), the propagation constant (β_v) and free space propagation constant (k) can be written as-

$$k_{yv}^2 + \beta_v^2 = k^2 n_c^2 \tag{2.9}$$

$$\text{Where, } k_{yv} = (V+1)\pi/W_{ev} \tag{2.10}$$

The effective widths of these modes (W_{ev}) can be approximated by the effective width corresponding to the fundamental mode (W_{e0}) for a high contrast waveguide (n_c >> n_{cl}).

$$W_{ev} = W_{e0} = W + \left(\frac{\lambda}{\pi}\right)\left(\frac{n_{cl}}{n_c}\right)^{2\sigma}(n_c^2 - n_{cl}^2)^{-\frac{1}{2}} \tag{2.11}$$

where, σ = 0 for TE and 1 for TM mode respectively. Applying binomial expansion on eq. 2.9 we can obtain-

$$\beta_v = kn_c - \frac{(v+1)^2\pi\lambda}{4W_{e0}^2 n_c} \tag{2.12}$$

The beat-length of the two lowest order modes can be written as-

$$L_\pi = \frac{\pi}{\beta_0 - \beta_1} = \frac{4n_c W_{e0}^2}{3\lambda} \tag{2.13}$$

The optofluidic device discussed later in this thesis work uses single mode waveguide (2D mode profile) coupled to the center of the MMI waveguide for launching light. For

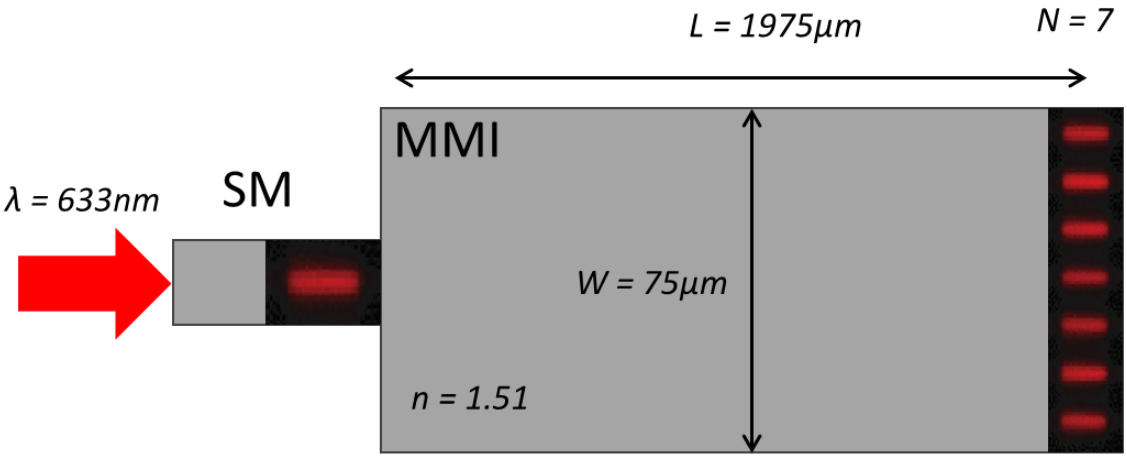

Fig. 2.4 Multimode interference pattern.

this symmetric input case, the *N* number of self-images of the input beam can be obtained at a distance *L* related to the beat-length according to eq. 2.14.

$$L = \frac{3pL_{\pi}}{4N} \tag{2.14}$$

$$N\lambda = \frac{n_c W_{e0}^2}{L}\text{; considering, p = 1} \tag{2.15}$$

For a 633nm laser light coupled to a 75µm wide MMI waveguide with n_c = 1.51 and n_{cl} = 1.44, we can calculate, $W_{e0} = W$ + 0.45µm. As our optofluidic device operation range covers visible light (λ = 400-700nm) and the geometric width of the waveguide is very large compared to the penetration depth the fundamental mode, we can consider $W_{e0} = W$ and rewrite the eq. 2.15 as-

$$N\lambda = \frac{n_c w^2}{L} \tag{2.16}$$

Fig. 2.4 shows N = 7 distinct spot pattern generated at a distance L = 1975µm inside the 75µm wide MMI waveguide when coupled with a 633nm laser light.

2.4 ARROW (Anti-Resonant Reflecting Optical Waveguide) principle

Biomolecules are typically suspended in, stored within, and transferred through water-based buffer solutions to replicate the physiological pH conditions in which they are naturally present. So, it is necessary to develop a waveguiding mechanism where the light will propagate and interact with biomolecules suspended in lower refractive index core i.e., water (n = 1.33) while being surrounded by higher refractive index solid oxide i.e., SiO_2 (n = 1.47) walls. The TIR principle fails here as the core has a lower refractive index than the cladding. The Anti-resonant reflecting optical waveguide (ARROW) principle can overcome this challenge by creating a Fabry-Perot etalon surrounding the liquid channel [42]. A stack of alternating layers of materials with refractive indices n_{L1} and n_{L2} with thickness t_{L1} and t_{L2} can be designed so the total phase shift of the light propagating in these layers meet the anti-resonant condition i.e., the layers effectively act as a reflector. For an ARROW channel with thickness d_c and refractive index n_c, a generalized solution for each layer thickness as shown in eq. 2.17 can be obtained by setting $n_{L1} > n_c$ and n_{L2} so the phases due to reflection in the first layer will be zero.

$$t_i = \frac{(2N-1)\lambda}{4\left(n_i^2 - n_c^2 + \frac{\lambda^2}{4d_c^2}\right)^{\frac{1}{2}}} \tag{2.17}$$

Here, N = 1, 2, 3,…. For typical ARROW optofluidic liquid channel, $d_c \gg \lambda$, and so $\frac{\lambda^2}{4d_c^2} << 1$. Eq. 2.17 can be re-written as

$$t_i = \frac{(2N-1)\lambda}{4(n_i^2 - n_c^2)^{\frac{1}{2}}} \tag{2.18}$$

For an ARROW liquid core channel with n_c = 1.33, and thickness d_c = 5μm surrounded by alternating layers of Ta_2O_5 (n_{L1} = 2.1) and SiO_2 (n_{L2} = 1.47), the thickness of the layers can be calculated as t_{L1} = 97nm and t_{L2} = 253nm considering N = 1 and design wavelength λ = 633nm.

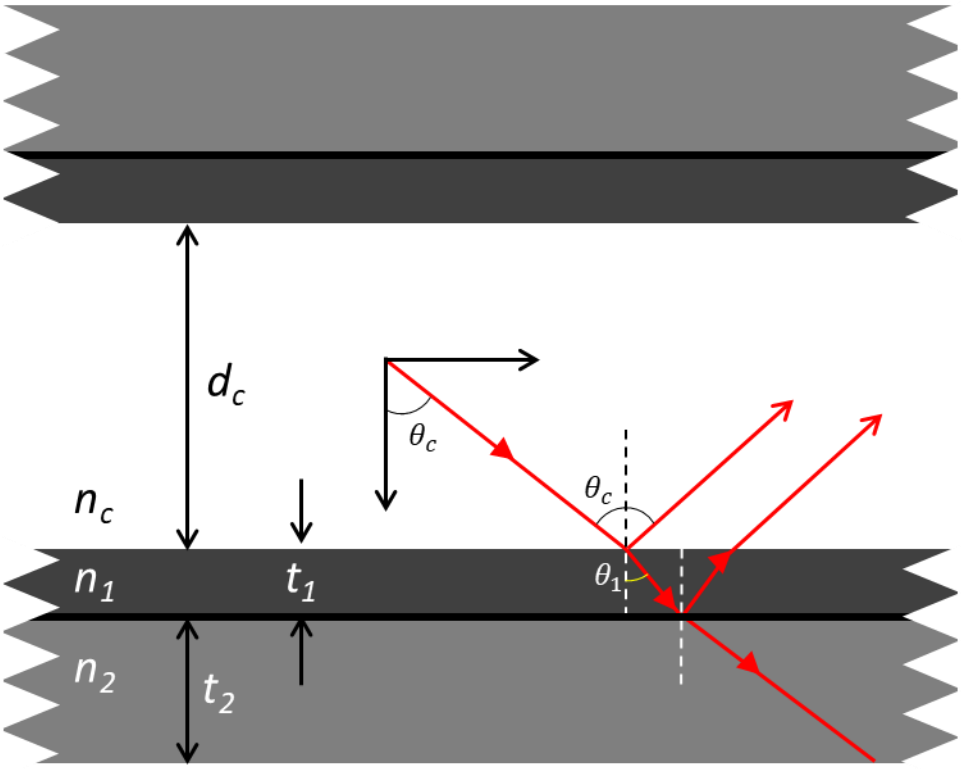

Fig. 2.5 ARROW principle and layers.

2.5 ARROW optofluidic device fabrication

A step-by-step schematic representation of an ARROW optofluidic device fabrication process is illustrated in fig. 2.6 based on ref [43]. The ARROW optofluidic devices were fabricated at Brigham Young University (BYU) on a 100mm diameter, <100>

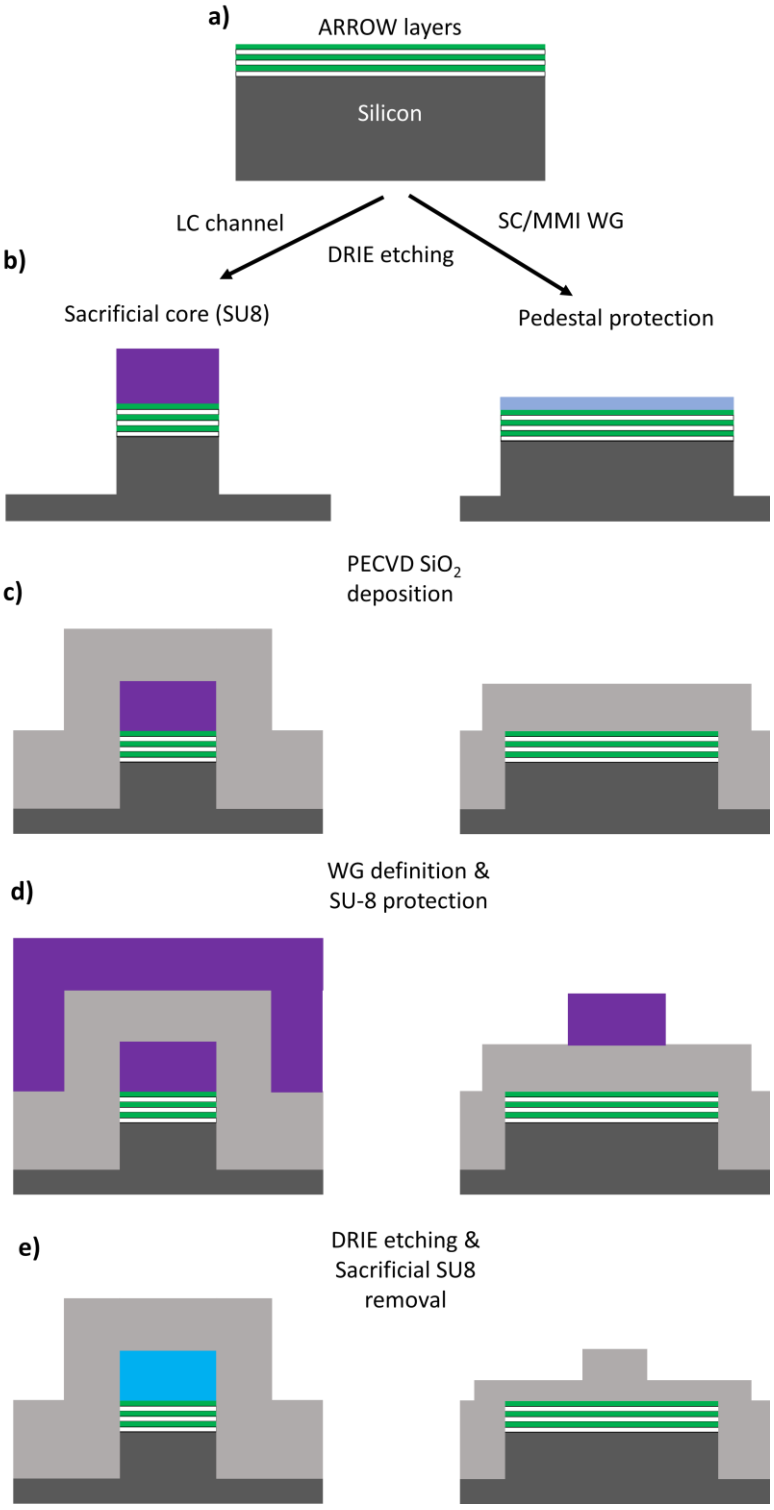

Fig. 2.6 ARROW optofluidic device fabrication steps. (Adapted from [43].)

oriented Si substrate. A sequence of alternating dielectric layers of SiO_2 (n = 1.47) and

Ta_2O_5 (n = 2.107) with respective thicknesses of 265nm and 102nm was created via sputtering over the substrate to form the ARROW layer (fig. 2.6a). SU-8 photoresist was spun on top of the ARROW layer and then patterned to form the 5µm x 12µm (height x width) sacrificial layer for the microfluidic channel and then a self-aligned pedestal protection layer for SC WG is formed. The photoresist pattern was then hard baked at 250°C for 5 min. Afterwards, a self-aligning pedestal was formed by reactive ion etching (RIE) (fig. 2.6b). A 6µm thick low stress PECVD Silicon oxide layer was deposited on top of the SU-8 pattern to form the wall of the microfluidic channel (fig. 2.6c). The 5µm tall solid-core waveguide intersecting the microfluidic channel was fabricated by reactive ion etching (RIE) using patterned SU-8 as waveguide definition layer (fig. 2.6d). The two ends of the microfluidic channel were opened by removing the oxide with wet etching, then a mixture of strong acids was used to remove the SU-8 to create the hollow microfluidic channel (fig. 2.6e).

2.6 Single molecule analysis in ARROW optofluidic platform

Fig. 2.7a shows a schematic of an ARROW optofluidic device with intersecting liquid core (LC) channel and MMI waveguide for fluorescence based single molecule analysis. As described previously, the MMI waveguide has predesigned dimension (L = 1975µm and W = 75µm) for creating a known number of excitation (N = 7) spots when coupled with a 633nm wavelength laser light according to the eq 2.16. Usually, a single mode fiber is butt coupled to the MMI waveguide for launching the laser light. Two metal reservoirs are glued to both ends of LC channel for introducing fluorescently labeled particles by applying negative pressure. Once the fluorescently labeled particles

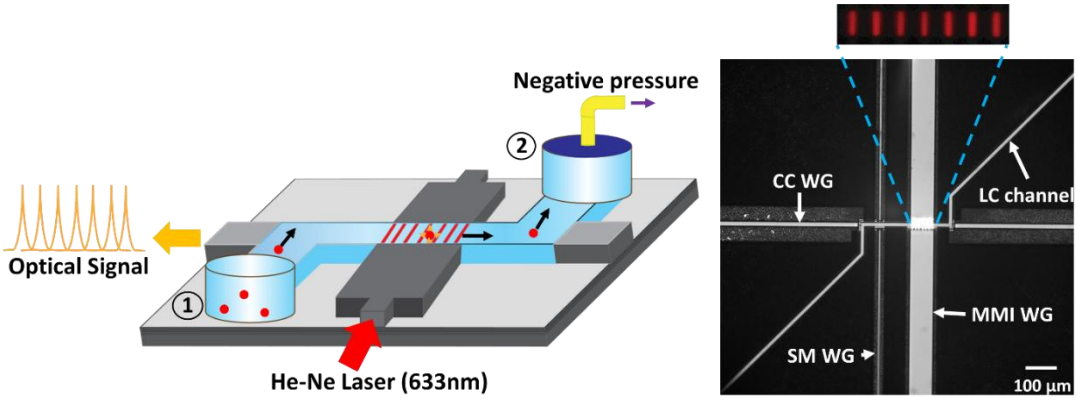

Fig. 2.7 a) Schematic, b) top-down image of MMI waveguide-based ARROW optofluidic single molecule analysis platform.

enter the excitation region, they emit fluorescence signal that guides through the LC channel according to the ARROW principle towards the collection waveguide. The collected fluorescence signal gives seven distinguishable peaks in time domain as shown in yellow trace. Fig. 2.7b shows a top-down light microscope image of the device and the inset shows the spatial distribution of the 7 bright spots when the LC channel is filled with a 25% quantum dot solution in deionized (DI) water. It is possible to get different number of excitation spots by changing the design length of the MMI waveguide and so, it is possible to do spatial multiplexed detection of biomarkers with multiple LC channels intersected with the same MMI waveguide at different lengths. Previously, a 3x spatial multiplexed detection of bacteria plasmid (pUC19-KPC, pUC19-NDM and pUC19-VIM gene) was successfully performed in our lab by using a 75µm wide MMI waveguide (n_c = 1.46) with liquid channels intersecting at L_1 = 1676µm, L_2 = 2243µm and L_3 = 3350 µm for creating N_1 = 11, N_2 = 8 and N_3 = 5 spots respectively when excited with a single wavelength 556nm light beam [44].

This MMI waveguide based multi-spot excitation scheme can also be used for wavelength division multiplexed detection of several biomarkers flowing in the same LC channel. For example, the same MMI waveguide with dimension L = 1975μm and W = 75μm can produce $N_1 = 6$, $N_2 = 7$, and $N_3 = 8$ spots at the intersected LC channel region when excited with $\lambda_1 = 738$nm, $\lambda_2 = 633$nm, and $\lambda_3 = 556$nm wavelength light. With careful fluorescent label design, it is possible to obtain 7x multiplexed detection of nucleic acid targets using this scheme [45]. Finally, these two multiplexing techniques can be combined to perform spatial-spectral multiplexed detection biomarkers on a single chip [46].

2.6.1 Particle concentration estimation

MMI waveguide-based ARROW optofluidic device can offer highly sensitive, high-throughput flow-based biomarker quantification from bio samples with minimal sample processing. Eq. 2.19 shows the formula to calculate the target concentration by analyzing the collected fluorescence signal.

$$C = \frac{N}{t}\left(\frac{particle}{s}\right) x \frac{1}{\bar{v}}\left(\frac{s}{m}\right) x \frac{1}{dh}(m^{-2}) x \frac{1}{10^6}\left(\frac{m^3}{mL}\right) \tag{2.19}$$

where, N is the total number of detected events within the experimental run time t, and $\bar{v}$ is the average flow velocity calculated by eq. 2.20.

$$\bar{v} = \frac{\sum_{i=1}^{i=N} \frac{W}{\Delta t_i}}{N} \tag{2.20}$$

Parameters d, h, and W are independent of experiment type as shown in fig. 2.8. These equations consider that only a single particle resides inside the excitation volume (= Wdh) during the experiment time which is called the digital regime of operation. Each MMI spot has an approximate excitation volume of 69fL with 15.4μW average excitation power considering a laser light with fiber end power 4mW is coupled to it. The calculated maximum limit of particle concentration for the digital operation regime is 2.78×10^8 particle/mL. Usually, target biomarker concentration in relevant clinical sample i.e., SARS-CoV-2 RNA copies in saliva stays within 10^2 – 10^6 particle/mL which is completely covered by the digital regime of the MMI waveguide-based quantification platform [47].

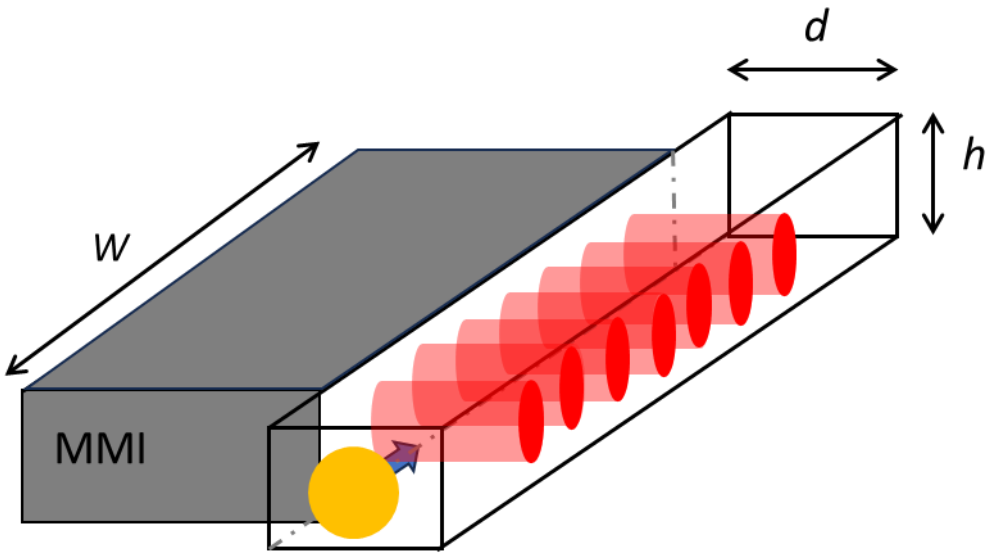

Fig. 2.8 MMI waveguide excitation volume.

2.7 PDMS based automatic microfluidic sample processing platform

Previously, we have discussed Si-based optofluidic device for on-chip fluorescently labeled biomarker detection process where the bio sample pre-processing, dilution and tagging is performed off-chip in 500µL ~ 1500µL volume tubes and vials. Due to the solid structure of the Si and SiO_2 structures, it is necessary to adopt elastic and flexible material for on-chip low volume liquid handling and manipulation applications. In our research lab, we have used Polydimethylsiloxane (PDMS) as flexible polymer for developing addressable microvalves and 3D structures. PDMS is cheap, chemically inert, biocompatible and it can be molded and shaped for rapid prototyping by soft-lithography process [48], [49].

Different types of microvalve structure have been explored by researchers over the years [50]–[54], such as push-down, membrane and lifting gate (see fig. 2.9). All these microvalve structures have pneumatic layer that can be controlled from outside and depending on the applied pressure, it can deform the membrane and control the fluid flow through the microfluidic channel. In this thesis, we will be focusing on the lifting gate microvalve structure where the fluidic channel is normally closed at atmospheric pressure or at applied positive pressure. Once negative pressure is applied, the membrane will lift-up and allow fluid flow from left to right. With an array of microvalves, it is possible to guide fluid to a certain direction as well as mix different samples together. Previous studies with such a microvalve array have demonstrated on-chip fluid control and mixing for labeling lambda DNA and complex bioassays [38].

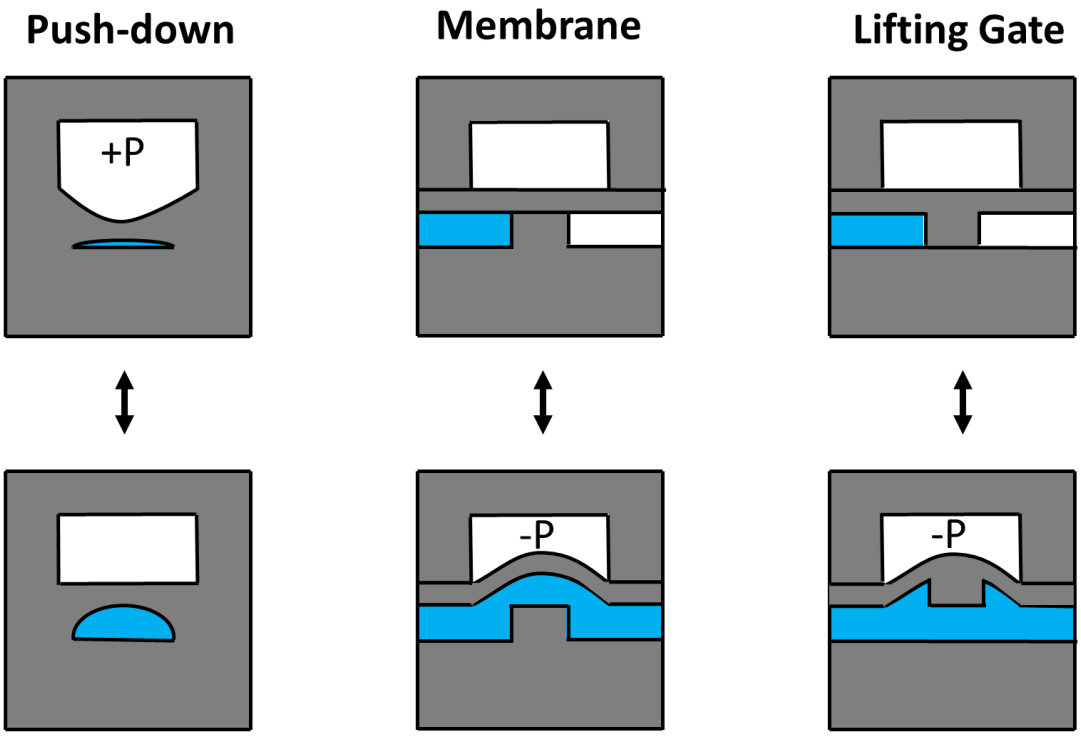

Fig. 2.9 Different valve configurations for PDMS microfluidic sample manipulation platform. (Adapted from [54])

Also, it is possible to change the refractive index of PDMS by changing the ratio of base to the curing agent, and thus it is possible to design a TIR based slab waveguide using a higher refractive index PDMS layer surrounded by lower refractive index PDMS, or air pocket [55]. Moreover, a carefully designed stack of cladding layer can be used to form a liquid core waveguide for biosensing application. A combined PDMS based platform performing both microfluidic sample processing and optical detection has been demonstrated in [56]. All these platforms use fiber-coupled laser light source for optical excitation, which introduces optical coupling losses. This issue can be overcome by integrating an on-chip controllable laser source such as optofluidic DFB dye laser to the PDMS platform [57]. Finally, a complete lab-on-chip system

combining three aspects, i.e., sample preparation, laser, and optical detection was implemented for Zika viral nucleic acid detection [58].

2.7.1 Fabrication of PDMS based automatic microfluidic sample processing platform

First, the microfluidic features designed in AutoCAD software are commercially printed in either Mylar transparency mask for 10µm or larger feature size or in a chrome mask for ~1µm precision. Next, an SU-8 master mold is created in four major steps. First, spin coating SU-8 on 100mm Si wafer, then expose the wafer to UV light in a mask aligner to transfer the features. Afterwards, a development solution is used to wash out the unexposed SU-8 material. Finally, a 5-minute hardbake step at 200°C completes the master mold creation. As shown in fig. 2.10, two different SU-8 master molds for fluidic and pneumatic layer are prepared. Drop casting of 10:1 (base : curing agent) PDMS creates 3mm thick pneumatic layer where spin coating of 10:1 PDMS creates 100um thin layer for valve and microfluidic channel structure. To create a 3D structure, first pneumatic layer is peeled from the Si-wafer and plasma bonded with the

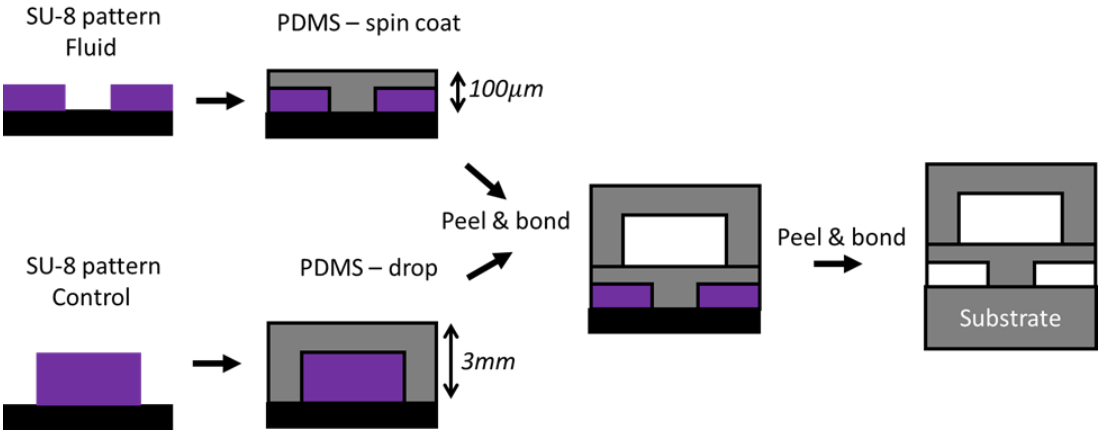

Fig. 2.10 Schematic of PDMS microfluidic sample preparation platform fabrication.

fluidic layer. Finally, the combined pneumatic control and fluidic layer is peeled from the Si-wafer and plasma bonded with blank PDMS substrate for enclosing the channel.

Chapter 3 Real-time single biomarker analysis and monitoring with FPGA integrated ARROW optofluidic platform

The development of highly sensitive, rapid, and compact point of care (POC) diagnostic platforms has been prioritized by researchers across the world for instant screening of infectious diseases, aiming to effectively contain the spread [59], [60]. The Integrated optofluidic platform shows excellent promise in this field by combining highly specific microfluidic sample processing and ultra-sensitive optical analysis on a single device [61]. The advanced optofluidic single molecule analysis platform based on multimode interference waveguide and anti-resonant reflecting optical waveguide (ARROW) principle has been utilized to detect single nucleic acid, proteins, viral particles at clinically relevant concentration enabling early diseases diagnosis [12], [13], [46], [62]. However, complex signal post-processing steps involving bulk computing resource are required to interpret the raw fluorescence signal generated from this highly sensitive ARROW optofluidic platform. This increases the sample to answer time and limits field-deployability of the platform for point-of-care (POC) application. One possible solution to overcome this signal-processing overhead is to integrate compact chip-scale, fast and programmable electronics with the ARROW device for live monitoring and flow analysis of fluorescently labeled biomarkers. This chapter will discuss design, characterization, and implementation of a novel field-programmable gate array (FPGA) integrated optofluidic platform with real-time signal

processing capability for fluorescent nanobeads and optically tagged antibiotic resistant bacterial plasmid DNA detection at clinically relevant concentration [17].

3.1 FPGA integrated ARROW optofluidic platform design

Fig. 3.1 shows a schematic view of an FPGA integrated ARROW optofluidic platform. At the heart of this platform there is an MMI waveguide-based ARROW device as previously described in section 2.6. The collected fluorescence signal from a labeled particle is a cluster of 7 uniformly distributed peaks in the time domain corresponding to the multiple excitation spots created inside the liquid core channel when excited by a 633nm laser light. The collected fluorescence signal is filtered and connected to an avalanche photodetector (APD) capable of single photon detection (SPCM-AQR-14-FC, PerkinElmer Optoelectronics). The APD outputs a 2.5V high 30ns wide transistor-transistor logic (TTL) pulse for each detected photon. In a usual post-processing based experiment, the APD is connected with a Time-Correlated Single Photon Counting (TCSPC) and Multi-Channel Scaling (MCS) device (TimeHarp 260, Picoquant) which

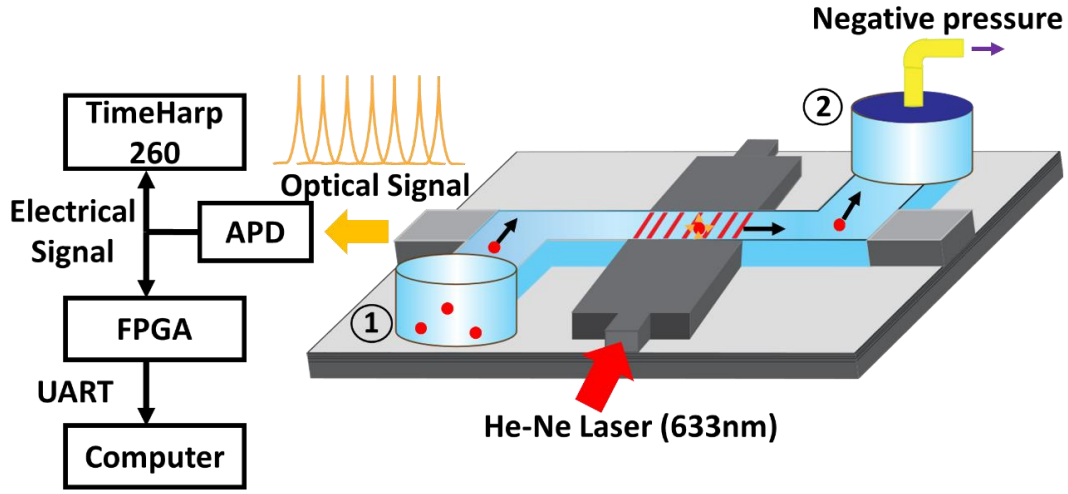

Fig. 3.1 Schematic view of an FPGA integrated ARROW optofluidic platform.

is operated by a commercial software installed in a desktop computer. The software stores the photon arrival time in a binary file that can be decoded and utilized for signal post-processing. This process highly depends on the speed and the workload division of the central processing unit (CPU) of the computer it is installed in, and it is challenging to configure the software for accessing the photon arrival time information in real-time for customizable application.

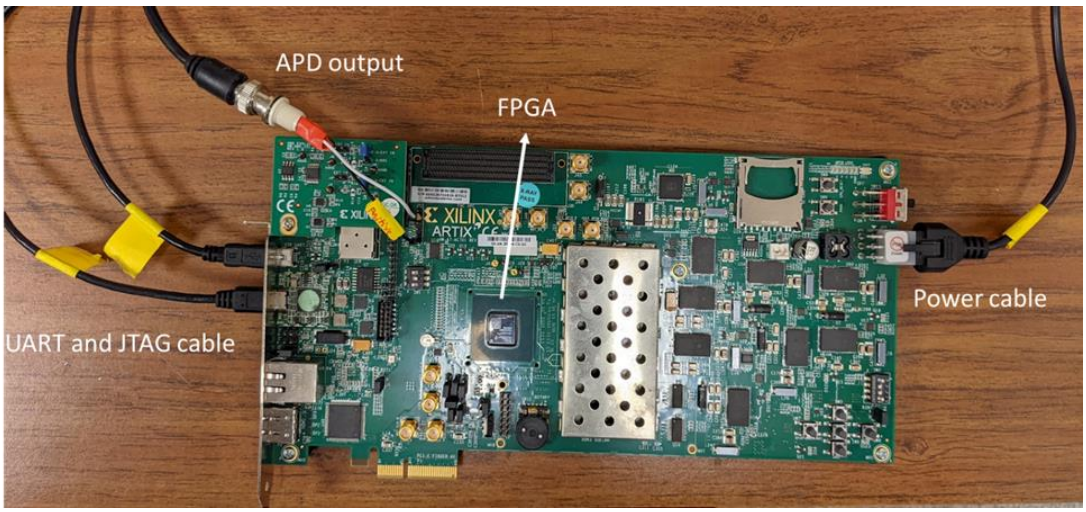

Fig. 3.2 Electrical wiring and connections for FPGA circuit.

On other hand, the proposed real-time analysis scheme connects the APD with an FPGA which is programmed in custom written Verilog code for acquiring and analyzing fluorescence signals for obtaining salient features from the detected signal and calculating useful experimental parameters. We have chosen FPGA as it offers easy and cheap chip-scale integration with high processing speed, and reconfigurability [63]. The FPGA transfers calculated results through the Universal Asynchronous Receiver-Transmitter (UART) communication protocol while the experiment is still running. For this proof-of-concept experiment, a terminal emulator (Tera Term Version 4.101, open

source) installed in a portable laptop computer is used which can be easily replaced by an LCD monitor for future POC application. Fig. 3.2 shows connection and wiring of the Xilinx Artix-7 FPGA AC701 Evaluation Kit for developing the integrated platform.

3.2 Real-time fluorescence signal analysis workflow

The custom written Verilog program can be visualized as three independently performing blocks, counter, processor, and communication block as shown in fig. 3.3 working in parallel with priority listing high to low going from left to right. All blocks communicate with each other by handshaking signals and there is a common 90MHz clock indicating the processing timescale of ~11ns.

The counter block senses the level of TTL pulse in each clock cycle and counts the number of cycles the TTL pulse stays at the high level (2.5V) within a user defined period called beginning time. The counted value is proportional to the fluorescence signal intensity. The binning time is chosen carefully so the fluorescence signal is properly sampled and reconstructed. For oversampled cases the signal level will be very low and the difference between consecutive data points will not be significant compared to the signal noise level. For the experiments described in this chapter, 100μs binning time is chosen. After the binning time, the counter block triggers an enable signal to the processor block and sends the binned photon count as soon as the acknowledgment signal is received back. While the data is being transferred, the counter block starts counting for the next binning time stamp without any delay.

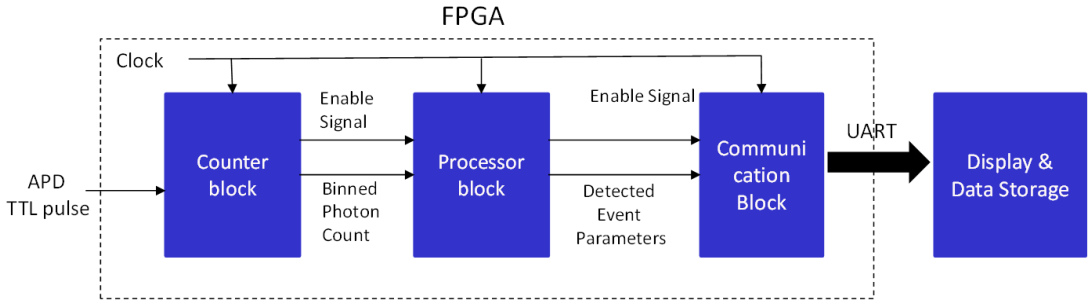

Fig. 3.3 Simplified block diagram of the real-time fluorescence signal analysis workflow.

The processor block is the brain of this real-time analysis workflow. To understand its workflow, we need to first analyze the possible features from a fluorescence signal trace for a single particle detection event as shown in fig. 3.4. Normally, without the presence of any target particle, the binned photon count stays within a background level. Once a target particle flows through the excitation spots, the binned photon count starts to increase and goes beyond the start threshold value. The photon count falls below the end threshold if the particle stays between two consecutive bright spots or completely passes through the excitation volume. We can think of this signal as a cluster of seven individual peaks. For the end of event case, the photon count stays near the background level before another particle enters the excitation volume. The processor block extracts the detection time tag *t[i]*, and cluster width $\Delta t[i]$ for a detection event *i* as experimental parameter.

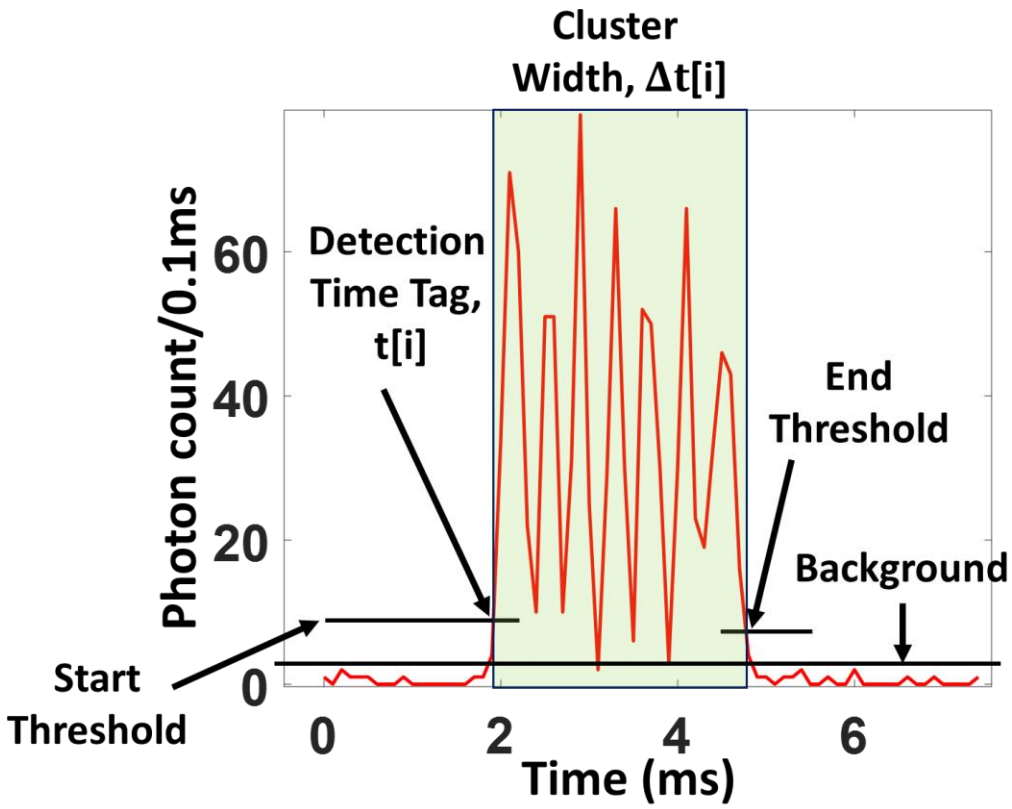

Fig. 3.4 100µs binned fluorescence signal from a single particle detection event in MMI-ARROW device.

The Verilog code for the processor block is written based on finite state machine (FSM) model and a simplified version is shown in fig. 3.5. Once the block is enabled, it checks binned photon count against a user defined threshold and if the threshold is crossed the block calculates height and width of each single peak inside the cluster. The processor block is fast enough to finish necessary mathematical operations before the next binned data comes within 100µs. At the end of each peak, the intensity level goes down (sometimes below the end threshold), but it rises within a couple of microseconds. However, for an end of cluster event, the intensity level stays below the end threshold for a long time (in the order of milliseconds). To confirm the end of a detected event,

the code waits for 1ms and compares binned photon count to the background level. The chosen wait time is larger than the usual time difference between consecutive peaks inside a cluster and smaller than the time difference between two consecutive detection events for digital regime of operation. After the confirmation of a successful detection event, the processor block sends an enabled signal to the communication block.

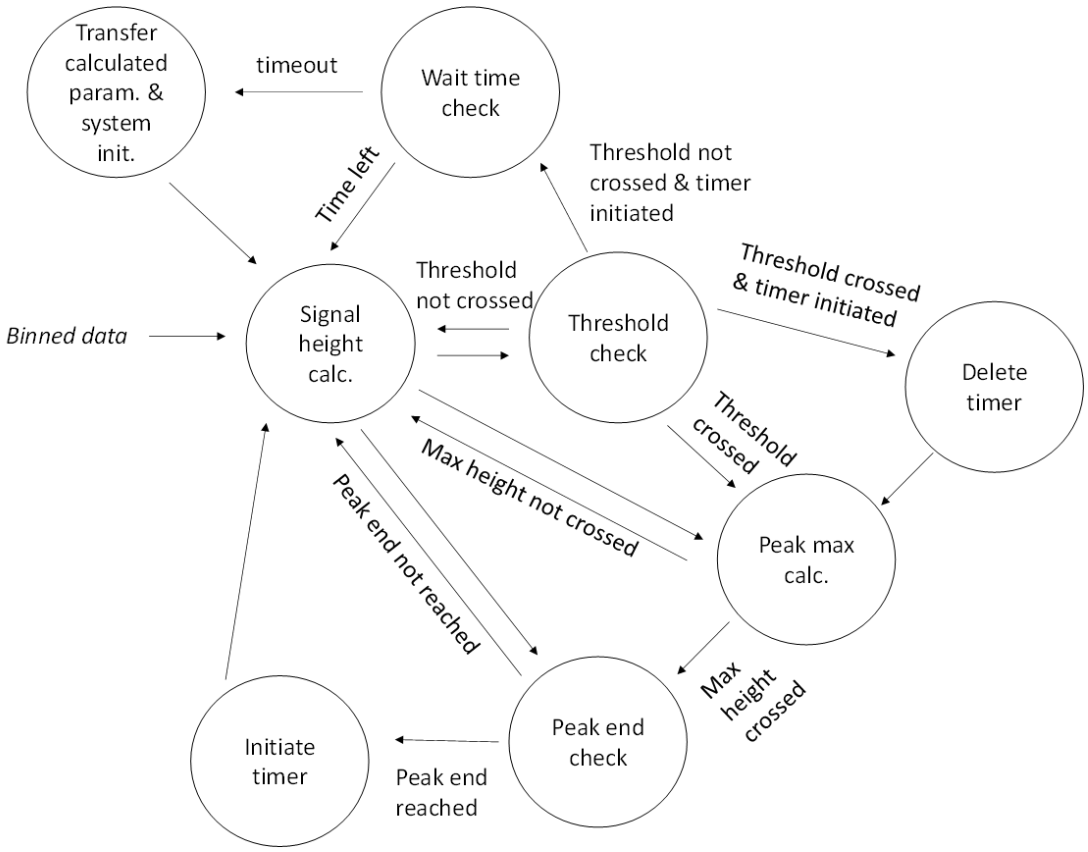

Fig. 3.5 Simplified FSM flow diagram for the processor block.

The communication block receives the experimental parameters from each successfully detected event such as detection time tag *t[i]*, and cluster width *Δt[i]*. Using the experimental parameters and user defined MMI excitation volume (= WA = Wdh) it calculates cumulative mean target concentration *C(i)* for live analysis. Eq. 2.19 and 2.20 is modified for FPGA based real-time application such as-

$$v(i) = \frac{W}{\Delta t(i)} \tag{3.1}$$

$$c_i(i) = \frac{i}{v(i)\ A\ t(i)} \tag{3.2}$$

$$C(i) = \frac{\left[\sum_{j=1}^{j=i} c_i(j)\right]}{i} \tag{3.3}$$

Here, i is the total number of detected events from the start of the experiment to the current timepoint $t(i)$. $v(i)$ is the instantaneous particle velocity, which is later used to calculate the instantaneous particle concentration $c_i(i)$. Four important parameters i.e., the number of detected particles, time tag of the detection event, MMI signal cluster width and calculated cumulative mean concentration of the target particle, are compressed in base64 encoding scheme and transferred to the emulator terminal by UART communication protocol without interrupting the performance of the other two blocks. It takes ~271.26μs to display 25 characters line resulted from a detection event in the terminal window for a chosen UART baud rate of 921,600/s. With rapid signal processing and data transfer, the total time delay from the signal acquisition to the result display lies within few milliseconds, demonstrating real-time operation. It is also possible to connect the FPGA with a custom written LabVIEW program to display the calculated results as well as record the experimental information to a file or cloud-based database.

3.3 Performance analysis of FPGA integrated ARROW optofluidic platform

First the performance of the FPGA integrated ARROW optofluidic platform is compared to the well-established TimeHarp260 card and MATLAB based post-processing scheme. To do so, 200nm diameter fluorescent beads (FluoSpheres TM, 625/645nm Crimson) at $3.4x10^6$/mL concentration were flown through the microfluidic channel. Fig. 3.6 shows 100μs binned fluorescence signal after MATLAB based post-processing analysis, indicating particle detection events in blue dot (top panel) and corresponding real-time detection confirmation spikes (black spike) generated by FPGA programmed with similar detection threshold value. The black dashed lines show good one to one correspondence among the first four detected events in both post-processing and real-time analysis scheme. A quantitative comparison considering MATLAB based post processing analysis as ground truth shows FPGA based real-time analysis method accurately detected 99% of the events within 472 total events with only 5 missing peaks. The missing peaks can result from low signal to noise ratio in case of a particle flowing close to the channel wall away from the excitation volume. This issue can be resolved by applying 3D hydrodynamic focusing of particles inside

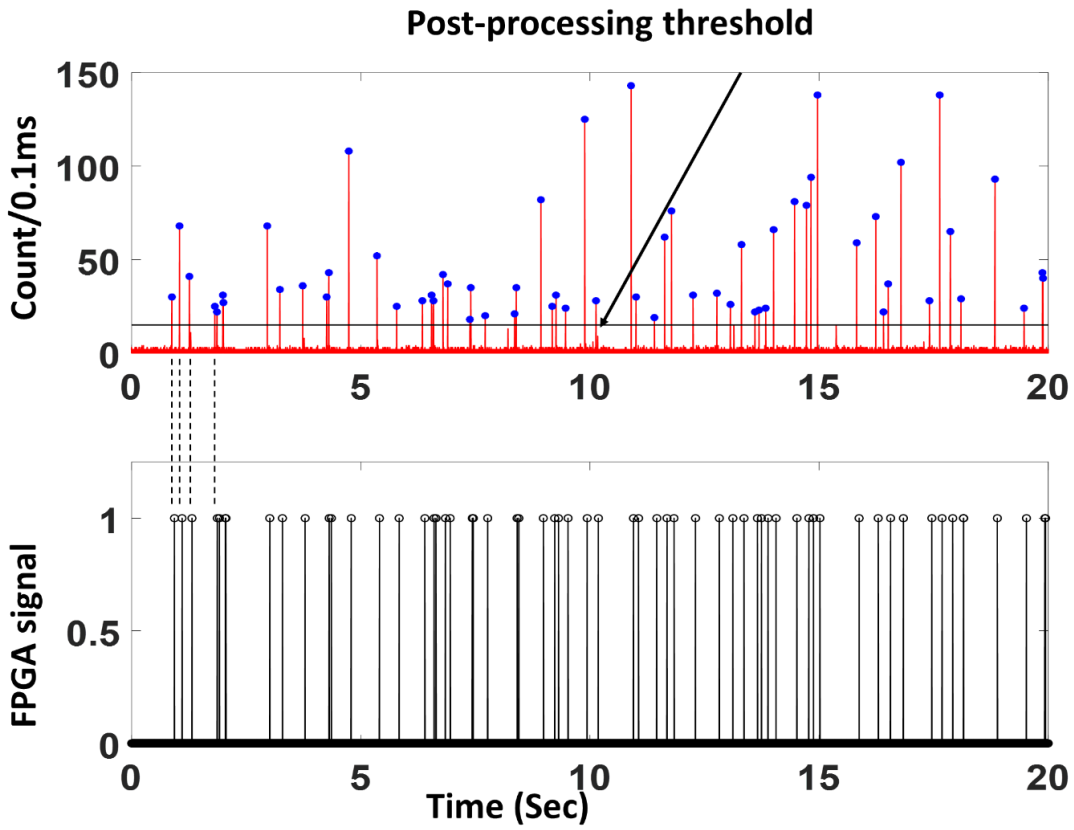

Fig. 3.6 200nm diameter fluorescent crimson bead detection in real-time (bottom) and comparison with post-processing analysis (top) (bead concentration: 3.4×10^6/mL).

the channel [64] and adopting a dynamic threshold approach based on real-time background noise level instead of a user defined fixed one. Further performance analysis such as target concentration analysis, settling time analysis, particle detection rate and frequency analysis will demonstrate reliability and repeatability of this FPGA based real-time analysis platform.

3.3.1 Real-time target concentration analysis

As described in section 3.2 and eq. 3.3, FPGA based real-time analysis scheme can calculate the target concentration while the experiment is running. Fig. 3.7a shows time

progression of a live cumulative mean concentration calculation from two separate experimental analysis with 200nm fluorescent particles prepared at concentration $3.4x10^6$/mL (black trace) and $3.4x10^5$/mL (red trace). The calculated cumulative mean concentration value starts with initial value as zero and stabilizes as the experiment progresses with an increasing number of detected events. At the end of the experiment, the cumulative mean concentration value calculated for the last detected particle can be approximated as the average concentration value calculated from the eq. 2.19, where $i = N$ and $t(i) = t$. Fig. 3.7b displays very good agreement between the calculated average concentration in real-time and the expected particle concentration. The error bar indicates standard error of mean. The detected concentration values are consistent with increasing deviation towards smaller concentration values due to a smaller number of particle detection events and the calculated values are slightly lower than the input concentration possibly due to human error generated from pipetting error and

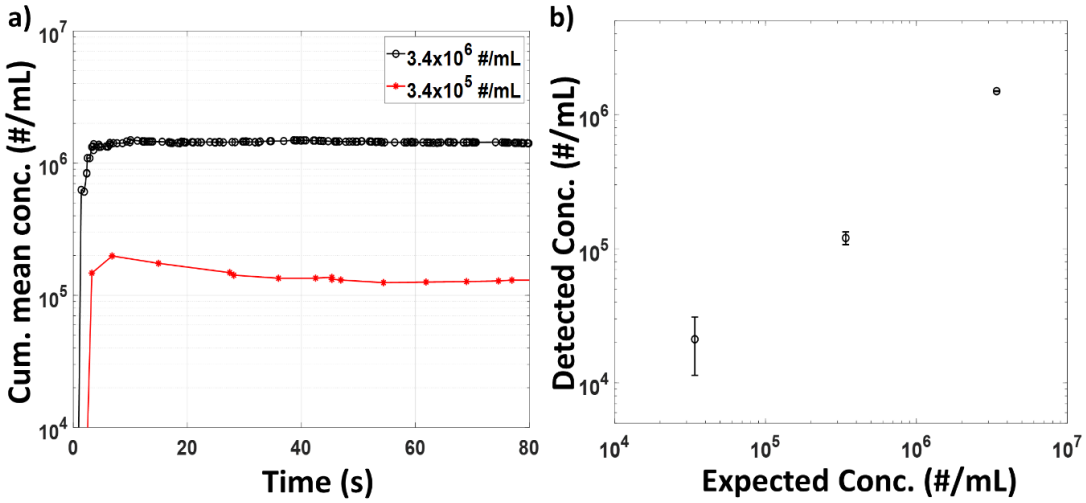

Fig. 3.7 a) Real-time particle concentration detection by FPGA based analysis with 200nm fluorescent beads. b) Real-time calculated vs expected target concentration.

systematic error generated from low fluorescence signal generated from the particles flowing near the channel walls. The resulting deviation at the low concentration level could be resolved by running the experiment for longer time by setting a minimum number of detected events (M) which is required for a reliable statistical analysis.

3.3.2 Settling time analysis

The minimum required number of events (M) for a reliable statistical analysis can be calculated by defining a settling time (t_s) such that all calculated relative concentration deviation for individual events based on eq. 3.4 will be within ±5% range after this time.

$$\frac{dC(i)}{C(i)} = \frac{C(i) - C(i-1)}{C(i)} \tag{3.4}$$

Here, *C(0) = 0*. Fig. 3.8 visualizes the idea of settling time by plotting the detected events with relative concentration deviation more than ±5% in red symbol and less than ±5% in green symbol versus experiment time. It is evident from the analysis that after t_s = 3.571s, all events were detected with relative concentration error within the predefined range. This experiment was performed with 200nm fluorescent beads at $3.4x10^6$/mL concentration.

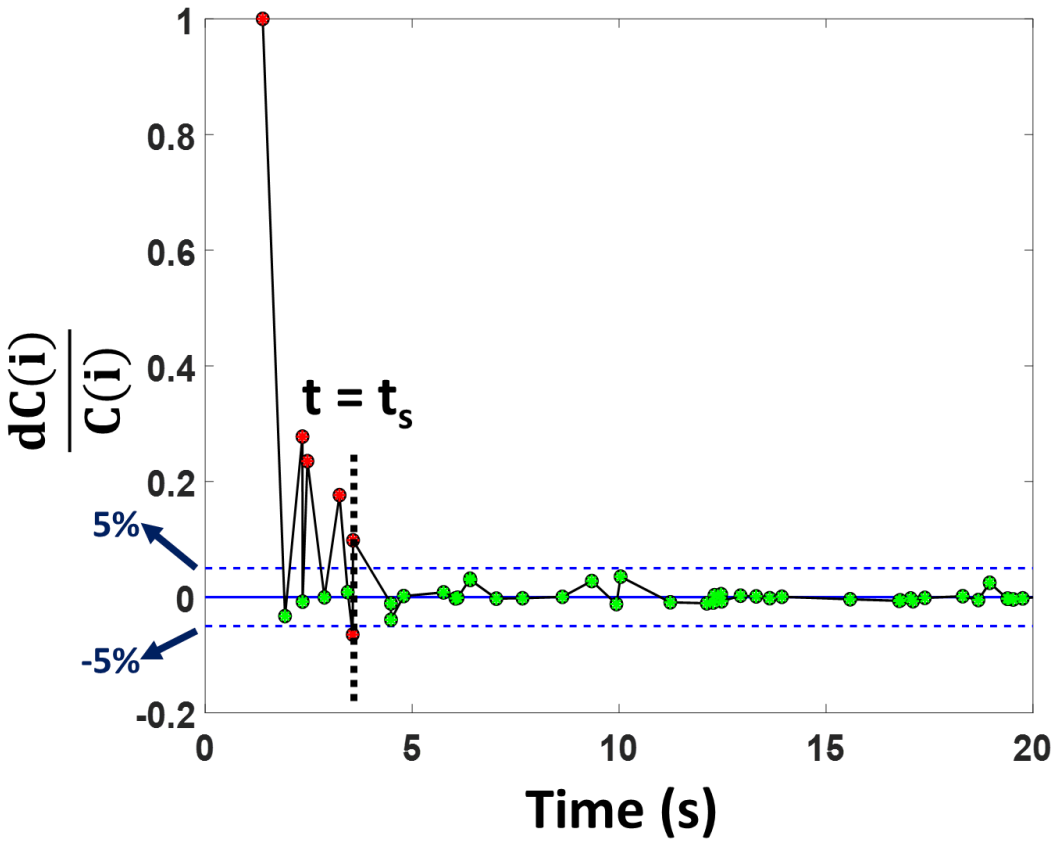

Fig. 3.8 Graphical representation of settling time (t_s) with experiment runtime.

Now, we can set for $i \geq M$ when $\frac{dC}{C} \leq \pm 5\%$. For constant volumetric flow velocity consideration, *v(i) = constant*. Now eq. 3.4 can be written as-

$$\frac{dC(M)}{C(M)} = 1 - \left(\frac{M}{M-1}\right)\left[\frac{\sum_1^{M-1} \frac{i}{t(i)}}{\sum_1^{M} \frac{i}{t(i)}}\right] = 1 - U(M) \cdot V(M) \qquad (3.5)$$

$$0.95 \leq U(M) \cdot V(M) \leq 1.05 \qquad (3.6)$$

As U(M) and V(M) both are functions of M, it is hard to find an exact solution for eq. 3.6. However, U(M) is independent of experimental results (see fig. 3.9a), thus it is possible to find a range of V(M) for each M that corresponds to relative concentration error value within ±5% (see fig 3.9b). Settling time for this analytical equation can be

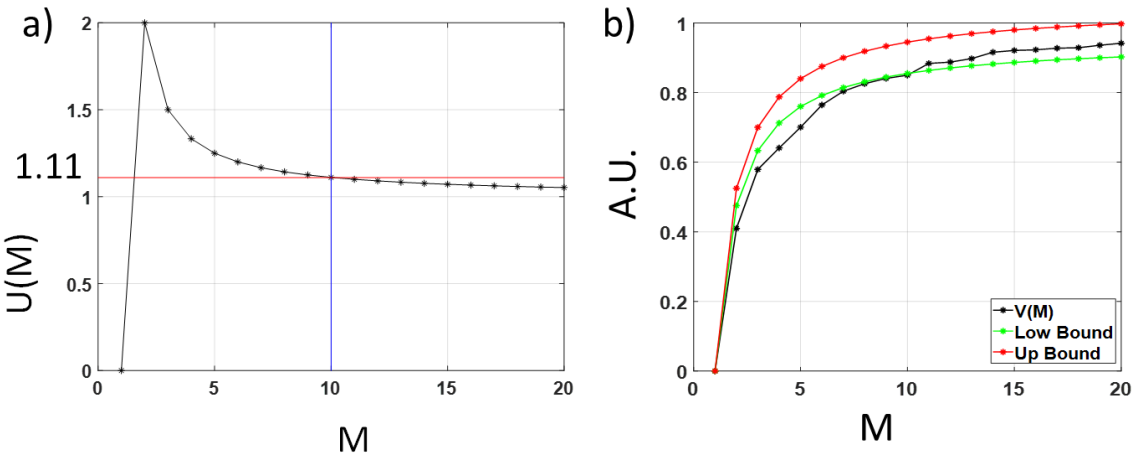

Fig. 3.9 a) U(M) and b) V(M) vs M with upper and lower bound.

calculated as $t_s = t(M)$. Fig. 3.10 shows settling time calculated from FPGA based real-time experiments and from analytical eq. 3.6 with constant volumetric flow velocity assumption. The plot shows higher settling time for lower target concentration as event detection rate is slower at lower target concentration. From both analytical and experimental observations, the most striking behavior of the value for M can be derived that it always remains within an upper limit, here 15, irrespective of the target concentration. So, with adjustment of the experimental time, it would be possible to get a minimum of 15 successfully detected events for a reliable real-time target concentration calculation. The calculated settling time using constant volumetric velocity yields lower settling time compared to the experimental one, as in reality the flow velocity inside the rectangular microfluidic channel is not uniform.

3.3.3 Continuous flow monitoring

The next characterization step is to observe the particle detection rate change in real-time with experimental conditions such as change of vacuum pressure. Sudden

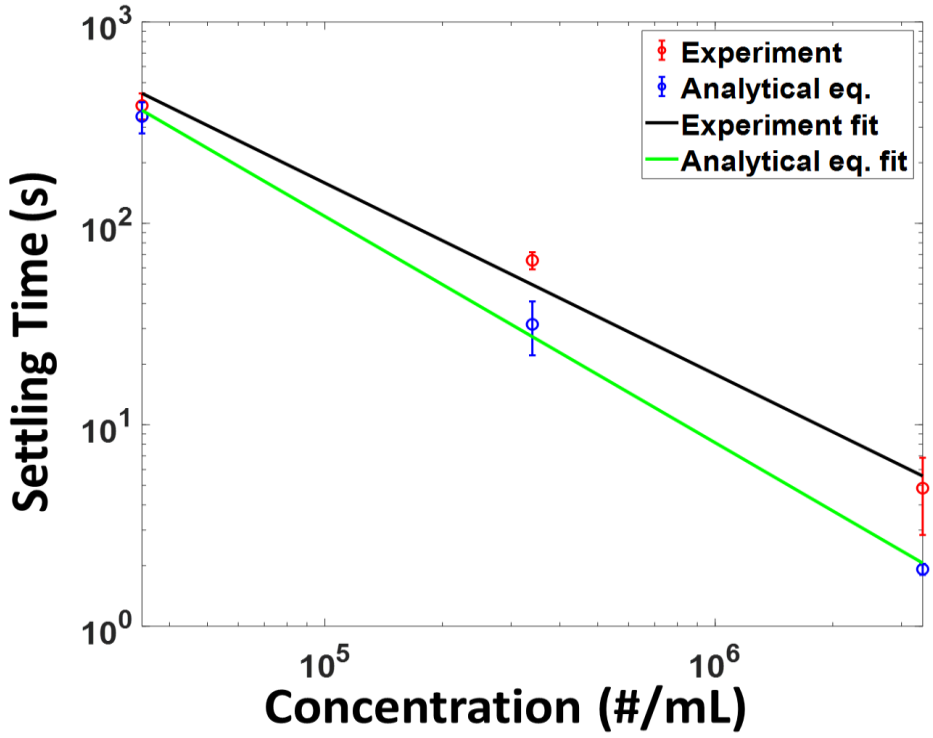

Fig. 3.10 Settling time calculated from real-time FPGA experiment and from analytical equation at different target concentration with linear fit, $R^2 = 0.98$ and $R^2 = 0.99$ respectively.

fluctuation in driving force can result from bad sealing or clogged channel because of unwanted residue or precipitation deposition from the target sample. The FPGA based real-time particle analysis platform can sense abrupt change in the particle detection rate or flow velocity and inform researcher so valuable reagents can be saved and the experimental setup can be fixed quickly. Fig. 3.11a shows cumulative number of detected particles vs experiment run time at two different target concentrations, where the slope indicates the detection rate. It is evident that for lower target concentration, the detection rate goes down as well as the time difference between two consecutive particle detection events increases and becomes erratic. Fig. 3.11b shows a clear indication of lower event detection rate when the vacuum pressure is changed from -

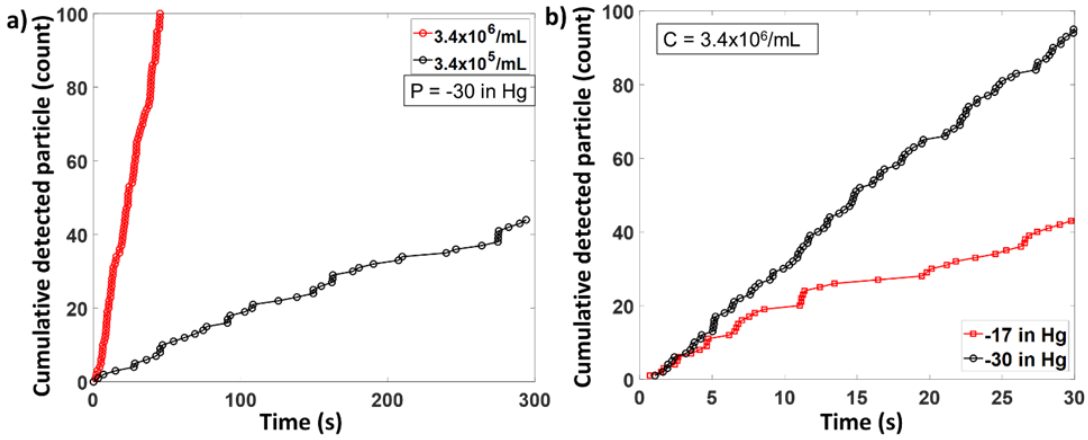

Fig. 3.11 Event detection rate change with a) target concentration and b) with change in applied vacuum pressure.

30 in Hg to -17 in Hg while keeping the target concentration same as 3.4x10^6/mL. These results demonstrate the applicability of FPGA based real-time flow monitoring as an internal feedback unit for a futuristic self-correcting system.

3.3.4 Event frequency analysis

The final characterization study was performed by statistically analyzing the time difference between two consecutive particle detection events. Ideally, the target particles flowing through the microfluidic channel under vacuum pressure should follow the Poisson process where the probability of a particle detection event is independent of all previous events. The probability distribution function of a particle arriving δt time later the previous particle can be written as -

$$P(\delta t) \propto e^{-\lambda \delta t} \tag{3.7}$$

Where, λ is the mean event detection frequency or detection rate. Fig. 3.12 shows 0.1s binned histogram of the time difference between two successive events during three separate experimental trials with 200nm fluorescent beads at 3.4x10^6/mL

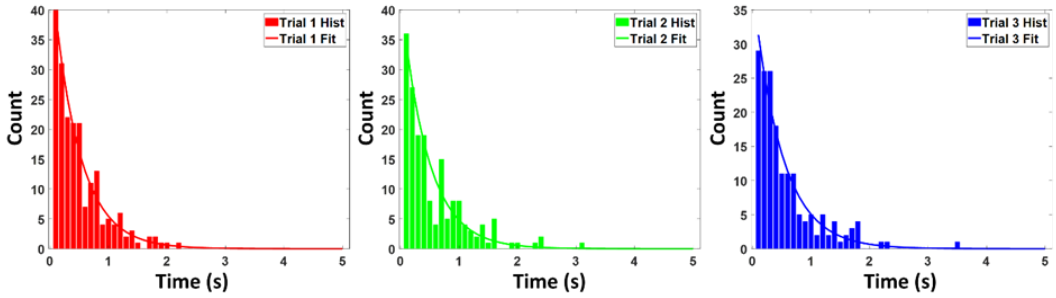

Fig. 3.12 Event frequency analysis with 200nm fluorescent beads at 3.4x10^6/mL concentration.

concentration. Each histogram follows Poisson process and can be fitted to exponential decay demonstrated in eq. 3.7, with λ = 2.9192/s, 2.31/s and 2.033/s respectively.

3.4 Real-time quantification of antibiotic resistant NDM-plasmid DNA

This well characterized FPGA integrated MMI-waveguide based ARROW optofluidic platform is next tested with fluorescently labeled bio molecule as a real-life molecular diagnostic application. Compared to fluorescent beads, optically tagged biomolecules are less bright, but the MMI waveguide-based ARROW optofluidic device is sensitive enough to offer reliable event detection even at clinically relevant concentrations [44]. In this study we targeted antibiotic resistant pUC19-New Delhi metallo-β-lactamase (NDM) gene in plasmid DNA which is liable for making NDM-1 enzyme that turns bacteria resistant to antibiotics such as carbapenem [4]. A rapid and reliable detection method such as FPGA integrated real-time optofluidic single particle analysis can help the healthcare system by offering short turnaround time.

The details of bacterial plasmid sample preparation is described in [44]. Briefly, 7mL of whole blood sample is spiked with *E. Coli* bacterial cells (5x10^6 CFU/mL) with

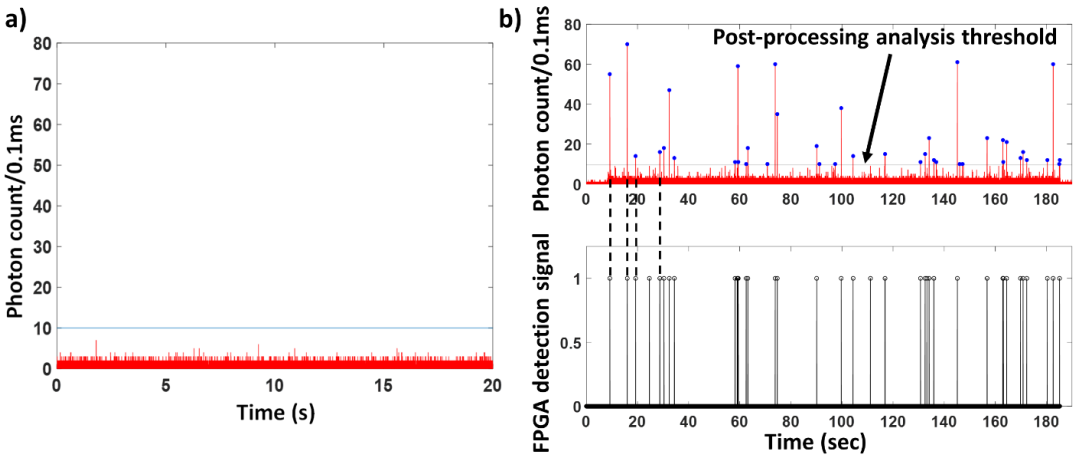

Fig. 3.13 Optically labeled NDM plasmid DNA detection. a) Negative control shows no observed fluorescence spike. b) MATLAB based post-processed fluorescence signal is compared with FPGA based real-time event detection confirmation spikes.

pUC19-NDM plasmid for mimicking a clinical sample. The target bacterial cells were separated using a spinning hollow disc and then the NDM-plasmids were sequence specifically captured and washed inside aptamer modified porous microfluidic channel. As the initial clinical sample went through multiple microfluidic operations with non-trivial losses and unknown transfer efficiency, the plasmid concentration in the eluted solution is different compared to the initial bacterial cell concentration. The plasmid sample was stained with 1µM Syto62 (Ex/Em: 649/680) intercalating dye which gives fluorescence signal only when it is bound to nucleic acid. A negative control experiment is performed beforehand to validate the functionality of the intercalating dye. Fig. 3.13a shows collected optical signal time trace when 1xPBS buffer with no nucleic acid was mixed with 1µM Syto62 dye and excited with 633nm laser light. For analysis threshold indicated in blue line, no false signal was detected by the FPGA based live analysis scheme.

When the stained plasmid sample with unknown concentration was run through the microfluidic channel, fluorescence spikes confirming detection event were obtained as shown in fig. 3.13b. A good one to one correspondence between MATLAB based post-processing signal analysis (top panel, detected event marked with blue dot) and FPGA based live event confirmation spikes (bottom panel, detected event marked with black spike) is demonstrated. A comparative study between the event detection time tag from post-processing analysis and real-time FPGA based analysis shows ~80.6% of the events are detected within a relative error band of ±5ms (see fig. 3.14a). This error can result from latency in the electric circuitry, or slight mismatch between the binning time starting point resulting in different signal shape and height. For low SNR fluorescence signal generated from optically stained biomolecule suspended in water-based buffer, a possible solution can be obtained by using a higher refractive index bio-compatible buffer as demonstrated in [65]. Finally, the FPGA based platform calculated NDM plasmid DNA concentration in real-time and the calculated average concentration was

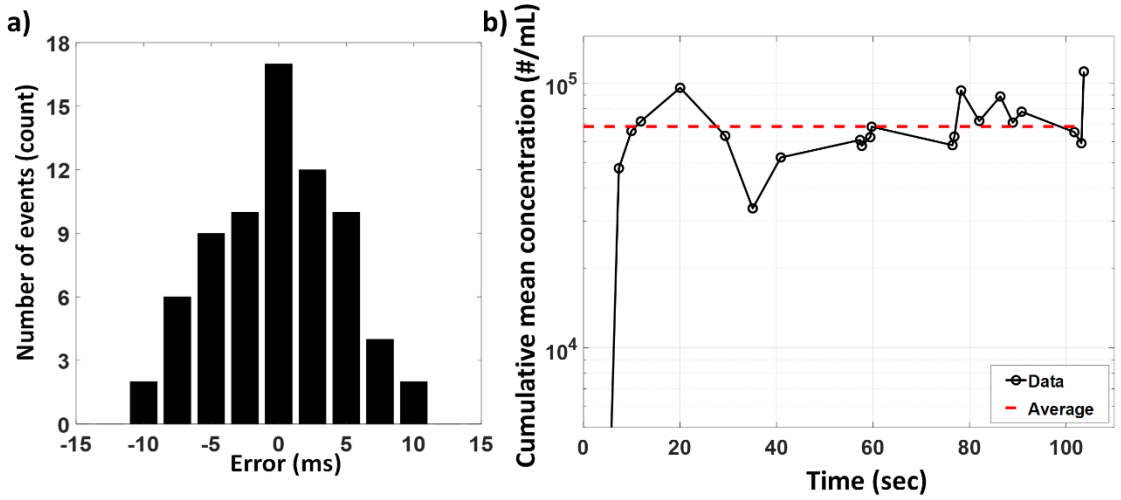

Fig. 3.14 a) Relative detection time error histogram and b) live concentration detection of bacterial plasmid DNA for FPGA based analysis.

$6.8x10^4$/mL (113aM) indicated by red dashed line in fig. 3.14b. This successful real-time analysis and quantification of both fluorescent beads and optically tagged biomolecules shows promise of a complete live bio-sample analysis tool with short turnaround time applicable for POC application.

Chapter 4 Internet of Things (IoT) for integrated remote operation of optofluidic analysis

The Internet of Things (IoT) allows secure communication and management of physical devices, sensors, and actuators, allowing seamless integration of different types of "things" in a single information network [66], [67]. Recent advances in affordable internet connected devices, and cloud computing enables IoT to be applied in personalized healthcare systems, such as smart and wearable sensors, ECG, and heart rate variability monitoring [68]–[73]. Moreover, various scientific research areas, especially life science are now utilizing the amazing capabilities of various IoT systems for remotely coordinating and managing massively parallelized experiments for achieving high throughput, facilitating secure data transfer and real-time cloud computation based rapid analysis [74], [75].

Actively controlled microfluidic sample processing allows various bioassay preparation steps on a miniature scale for single molecule analysis [19], [76], [77]. A PDMS based pneumatically controlled microfluidic lifting valve array is one such platform that has demonstrated excellent applications in processing complex bio samples and reconfigurable operation by manipulating nanoliter volumes of liquid [78]–[80]. Recent addition of optofluidic on-chip lasers and fluorescence detection on the same microfluidic device opened a door for enabling biofluid processing, optical labeling, microfluidic motion control, on-chip configurable laser source, fluorescence signal detection, and quantification in a single lab-on-chip (LOC) biosensor [58].

However, in case of a massively parallel detection scheme, controlling individual LOC devices one by one is not feasible. Integrating programmable electronics can solve this issue by automating the sample to answer process and sequentially performing time sensitive tasks without human error [56], [81]. Furthermore, IoT systems can be developed to create a network of coordinated microfluidic LOCs for real-time monitoring, remote accessibility and efficient data transfer [82]. This can also offer collaboration among scientific laboratories facilitating resource sharing beyond physical boundaries. LOC devices are also useful as a project-based learning (PBL) tool, where students can work through predesigned projects in biochemical and biomedical science and engineering fields and develop scientific critical thinking as well as technical skills [83], [84]. Being small in size, flexible, reusable, biocompatible, easily reconfigurable for different molecular diagnostic experiments, and requiring small reagent volume, LoC technologies can drastically reduce the costs of performing PBL experiments [85], [86]. Moreover, IoT connected optofluidic LOC can enable training students from underserved communities across the world [87].

In this chapter, first a functional integration of PDMS based programmable microfluidic valve array, i.e., automaton with an IoT framework is demonstrated for remote controllability. Then an elegant application of this IoT enabled optofluidic lab-on-chip platform is shown as a remote classroom learning tool for training programming concepts to Latinx life sciences students.

4.1 Cloud controlled optofluidic lab-on-chip platform design

Fig 4.1 shows a schematic of the cloud controlled lab-on-chip system comprising three basic components- a) local IoT device, b) MQTT broker, and c) Remote IoT device. Each component will be discussed briefly now.

4.1.1 local IoT device: Raspberry Pi controlled microfluidic automaton

The local IoT device stays inside the laboratory. Here, it consists of the microfluidic automaton (PDMS lab-on-chip device, solenoid valves, electronic relay), and an internet connected Raspberry Pi. The PDMS LOC device is based on pneumatically controlled lifting valves. A general description and fabrication method of such a system is described in section 2.7. The pneumatic control was obtained by connecting a stack of 3 port solenoid valves (SMC S070M-6DC-32) with the pneumatic inlets in the PDMS based lab-on-chip device. The solenoid valve is essentially a 2x1 multiplexer

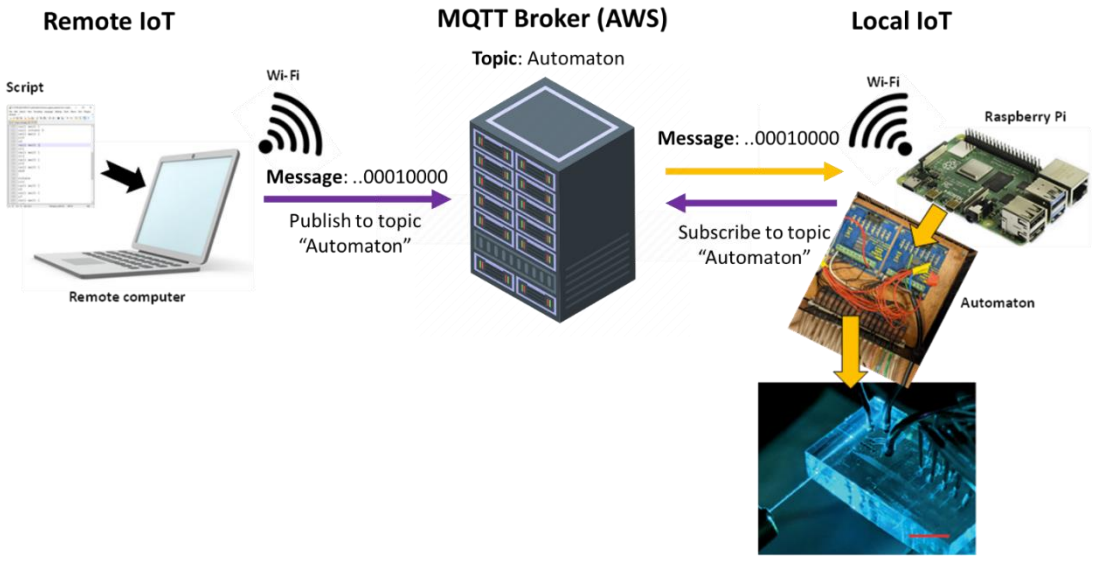

Fig. 4.1 IoT enabled optofluidic lab-on-chip platform.

switch which selects its output, either compressed air (positive pressure) or vacuum suction (negative pressure) based on a logical input signal. An electronic relay (ULN2803 Switch Board) provides the logical signal with appropriate voltage level (0 – 12V, 1.5A) for operating the solenoid valves by converting the logical voltage (0–3.3 V, 8 mA) level from the general-purpose input/output (GPIO) pins of a programmable electronics. The electronic relay and solenoid valves are housed in a small box. When connected with the PDMS microfluidic valve array, it is called an "Automaton". While the system architecture of PDMS lab-on-chip optofluidic device connected with the solenoid valve was developed earlier [78], I integrated an internet-connected Raspberry Pi (Model 4) device, eliminating the need for a desktop or laptop computer as programmable electronics. Raspberry Pi is a great choice here as it is small, light-weighted, portable, cheap, and comes with a self-sufficient Unix-based operating system that can be easily programmed in python [88].

4.1.2 MQTT broker

The Message Queuing Telemetry Transport (MQTT) protocol is chosen for establishing communication between the Raspberry Pi based local IoT device and a remote user. MQTT is a well-supported and industry standard publish-subscribe messaging protocol [89], [90]. A web server such as Amazon Web Service (AWS) acts as a broker that exchanges messages securely among different devices communicating in MQTT protocol [91]. Briefly, a list of devices and corresponding security license is created in the AWS account under a "topic". Here, a graphical user interface (described in a later section) acting as remote thing publishes an MQTT message through AWS

communication channel under the “Automaton” topic, and the local IoT thing listens to the MQTT message by subscribing to the same topic. As the AWS generated license needs to be present in both publisher and subscriber device, this communication channel is secure and close. The messages transmitted from the graphical user interface (GUI) are usually encoded and a decoder program runs inside the Raspberry Pi to extract necessary commands.

4.1.3 Remote IoT device – Graphical User Interface (GUI)

The GUI acted as a virtual IoT device that could be easily accessed and operated from any remote location by any user with correct log-in information. I designed the GUI by writing a custom python program that can run in web hosted Google colab or Jupyter Notebook environment (wetAI; www.wetai.gi.ucsc.edu). The custom python code for our designed GUI is provided in section A.1. The GUI offers three modes of operation. The first mode is for remote control of individual pneumatic valves for manual operation. This is offered by a set of user-controlled check buttons corresponding to each of the pneumatic valves. This mode helps to pre-wet and individually check the functionalities of the PDMS microvalves. However, while running a biological sample preparation step, one may need to sequentially turn on and off multiple valves simultaneously with a pre-defined time delay which is not possible with manual operation. To overcome this challenge, a simple, intuitive, and custom programming language with a predefined set of “instructions” and “functions” was developed previously [56]. A code written in this language is called “script”, which is basically a text file that can be opened and edited in any text editor application. For this proof-of-

concept experiment, only a few instructions are added with very self-explanatory key words, such as “O10” instruction stands for “open valve no 10”. This custom language and the structure of a script is very simple to understand, and anyone can quickly learn irrespective of their education background and programming experience. Also, Raspberry Pi has sufficient memory to locally save template scripts for common applications i.e., post-experiment device washing, that can be later accessed from the GUI application. The second mode of operation GUI offers is the selection and execution of a locally saved script for automation. Finally, a user can write and upload their own script remotely for a particular application just by following a template. This new script can also be stored in the local IoT device for future usage. The GUI transfers user input and the script as a MQTT message encoded in a special format. A python-based interpreter program running in the local Raspberry Pi device is used to decode the message and prepare a sequence of logic level information which is instantly output through GPIO pins.

4.2 Example and interpretation of a “Script”

The custom programming language allows researchers to write simple instructions in text file without prior knowledge about the GPIO pin orientation, logic level of Raspberry Pi hardware or experience on conventional programming languages such as C/C++ or Python. Additionally, no special application or integrated development environment (IDE) other than a text editor is needed on the user side computer to write/read a script. As Raspberry Pi is unable to process human language, an interpreter program is needed to convert the script to a sequence of Raspberry Pi readable logic

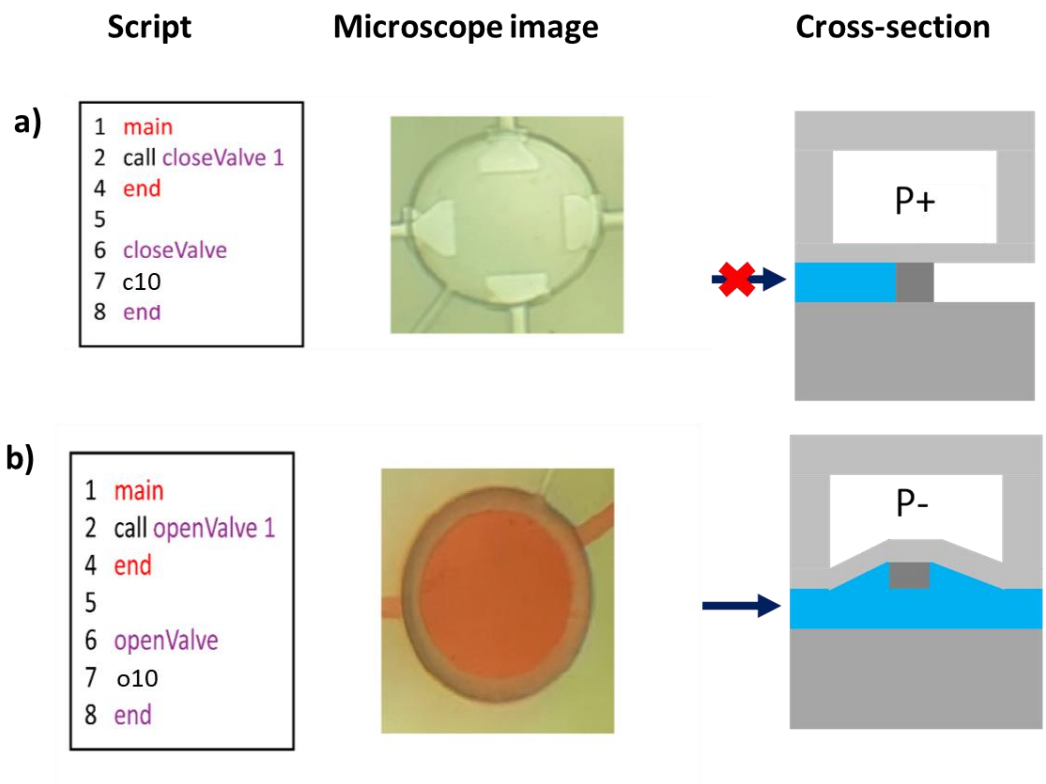

Fig. 4.2 Example of "script" for a) closing a valve, and b) opening a valve.

level information for each GPIO pin. Before explaining the underlying working principle of the interpreter program, we discuss the general structure of a script.

Similar to the C programming language, a “script” should have a “main” block with lines of instructions. The block runs once, and the lines are executed one after one. Each instruction line starts with a command, defined by a special character or word. The current version of the program allows three single character commands, such as “o” for opening a valve, “c” for closing a valve and “w” for a wait period. “c” and “o” commands have the desired valve number, and the “w” command has a wait period in milliseconds as a parameter. Also, additional user-defined functions can be called by writing “call” command followed by the function name. The definition of the user-

defined function should be provided by the user after the “main” block. Fig. 4.2 shows examples of simple scripts written for closing and opening valve number 10. It also demonstrates light microscope image and cross-sectional schematic view of the microvalve when it is open and filled with red food dye solution.

Previously a LabVIEW based interpreter program was running on a personal computer connected with a data acquisition board (NI USB 6501, National Instruments) for local implementation. For this remotely controlled IoT implementation, I replaced the PC

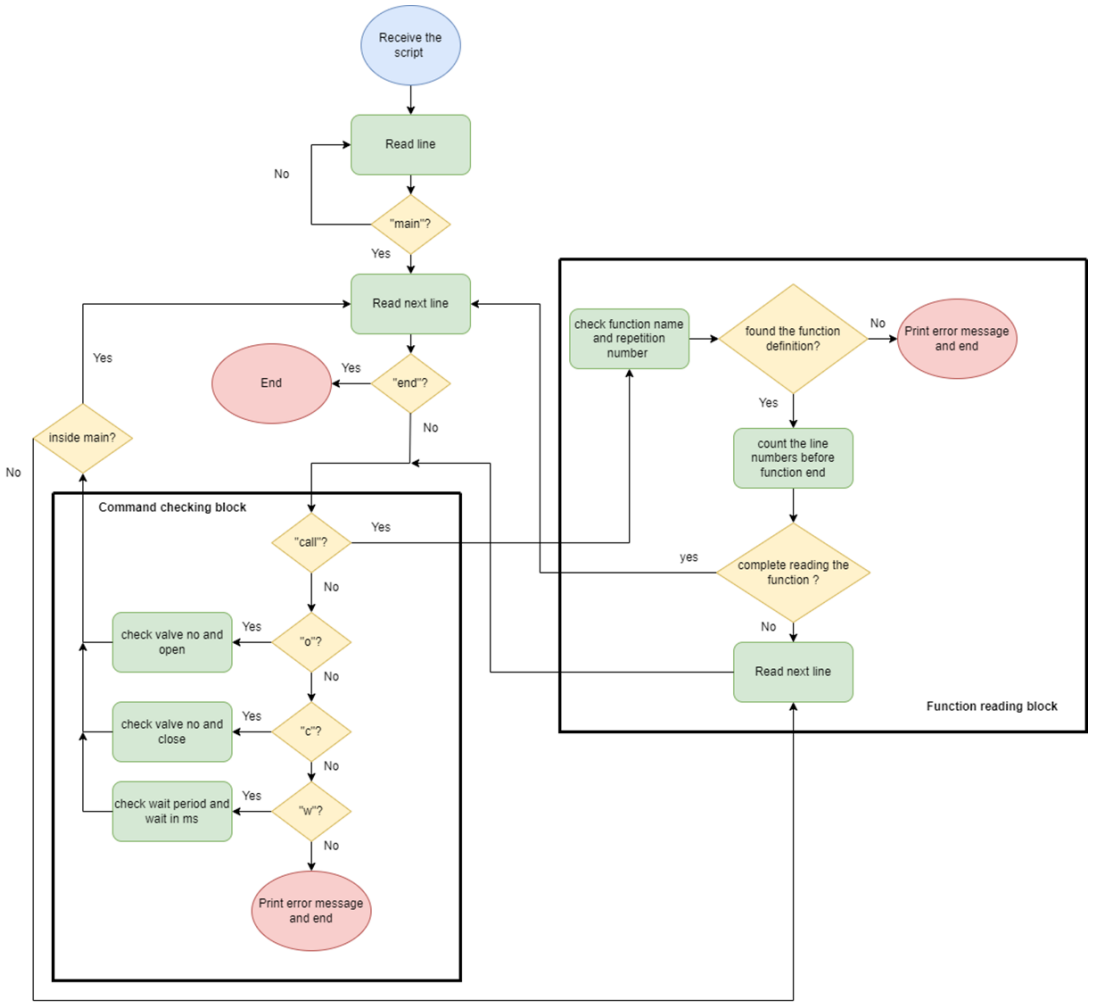

Fig. 4.3 Flowchart of the interpreter program.

and data acquisition board with a single Raspberry Pi and thus the interpreter program was redesigned for the newer platform. The interpreter program is written in python and its workflow can be divided into two major blocks defined as command checking block and function reading block (see fig 4.3). The interpreter program ignores any line written before the “main” keyword, indicating the beginning of the script. After that, the next lines are processed in the command checking block. For “call” instruction, the program moves towards the function reading block and finishes all the instructions written inside the function definition. After that it returns back to the main block and continues reading the next line before it reaches “end”, marking the end of script. The custom python code for this interpreter program is provided in section A.2.

4.3 IoT connected LOC as project based remote learning tool

The IoT enabled optofluidic LOC platform was utilized to remotely train programming concepts to life sciences students at the Universidad Católica Boliviana San Pablo. This educational outreach program was arranged by the Applied Optics and Mostajo-Radji lab within the framework of the NIH Center for Live Cell Genomics. A total of 42 students ranging from first to fourth year in college (18-22 years old) participated actively in the program. A training module was designed in the context of an on-chip water quality test targeting Escherichia coli (E. coli) bacteria, a strong indicator of water contamination. Water pollution is a common issue in developing world and a field study on the quality of drinking water in Bolivia showed that 64% of the tested water samples had E. coli contamination [92]. The module included two project preparation lectures introducing capabilities of microfluidic LOC devices and the

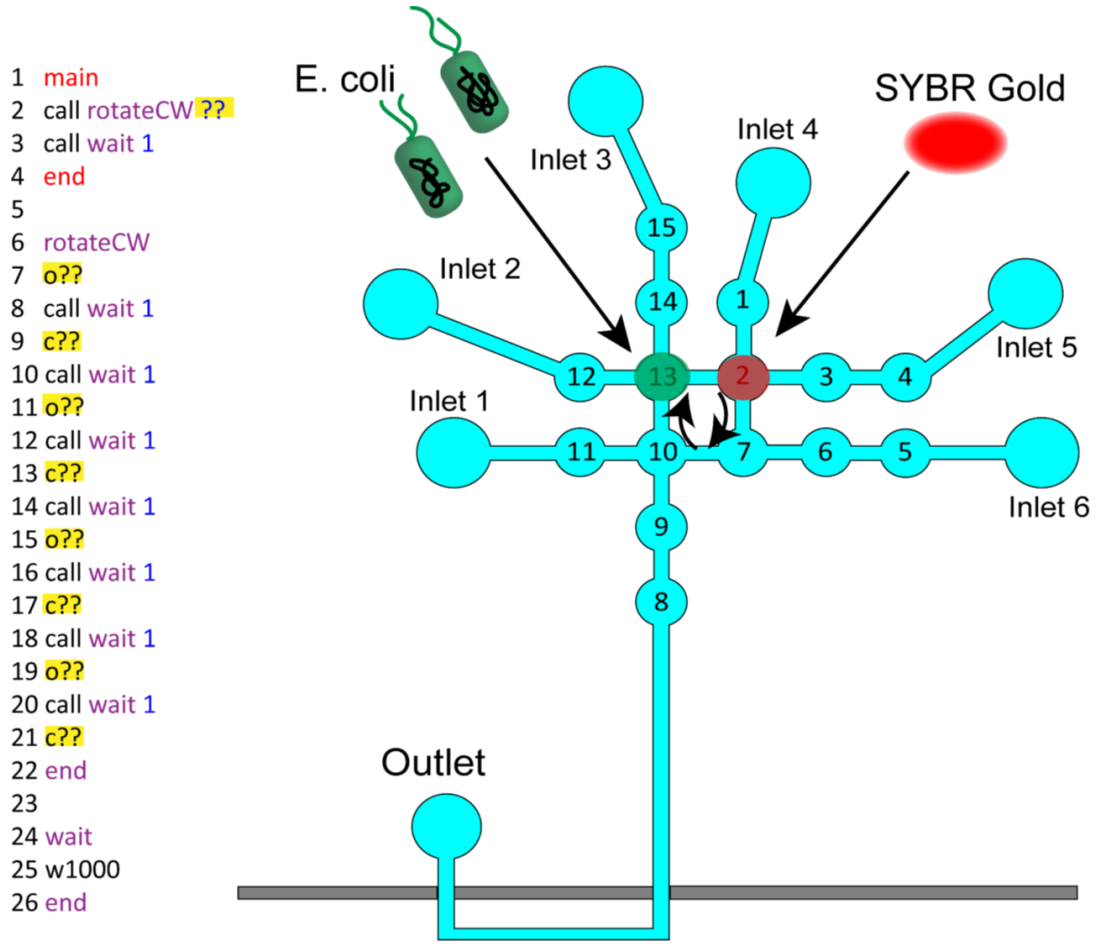

Fig. 4.4 Homework problem for the students participating in the remote educational outreach program.

custom programming language "script" for automatic liquid mixing and handling. The lectures were delivered by Dr. Mohammed Mostajo-Radji in Spanish, the native language of the Bolivian students. A quick demonstration of two different colors (red and blue) food dye mixing in an IoT connected automaton platform was performed for the students at the end of the lecture. My fellow lab mate, Dr. Tyler Sano performed the PDMS device fabrication, and the liquid sample handling, where I was responsible for the implementation and functioning of the IoT system. A predesigned project was assigned to the student groups to program the microfluidic valves for staining E. Coli

bacteria available in a contaminated water source by SYBR Gold, a highly sensitive cyanine dye that intercalates with plasmid DNA inside the bacteria and emits fluorescence signal when excited by 488nm laser light [93]. Here, laboratory grade DI water was spiked with isolated E. Coli bacteria to mimic a contaminated water source. Fig. 4.4 shows a homework problem related to the project with incomplete script. The task for the homework problem was to complete the script for 5 times counterclockwise mixing of contaminated water in valve 13 and SYBR Gold in valve 2. While solving this real-life problem, students learned the basic concept of programing a microfluidic platform for laboratory automation in a simplified way. Each student group successfully executed their E. coli staining script remotely from Bolivia, manipulating a PDMS microfluidic device located in Santa Cruz, California, to complete the project. A live video feed of the microfluidic valve movement was broadcasted for the students to see their successfully completed script working for E. Coli staining. Although this module was designed in the context of bacteria contaminated water pollution, several other modules can be designed ranging from traditional immunohistochemistry using antibodies, to microorganism detection. Moreover, the simplicity of the interpreter program allows this tool to be used as a first exposure to programming.

Chapter 5 Background on integrated nanopore-optofluidic platform development for high-throughput single molecule analysis

Single molecule analysis (SMA) involves characterization of individual molecules at a higher precision and sensitivity compared to ensemble measurement methods, leading to a deeper understanding of the structure, function and interaction of biomolecules at the molecular level [29], [94]–[96]. This advanced technique contributed advancements in biotechnology, disease diagnostics, and precision medicine [97]–[99]. Recently, nanopore technology has been proven to be a very effective label-free single-molecule analysis tool with exciting applications in the field of genomics, transcriptomics, and proteomics [100]–[104]. Also, advanced nanofabrication methods enabled integration of nanopore technology with electronics, microfluidics, and optics resulting in a single lab-on-chip platform combining all these powerful laboratory techniques [105]–[107].

Previously, chapter 2 discussed Si fabrication based planar solid core waveguide connected optofluidic platforms for fluorescence based single molecule analysis. The same optofluidic device can be utilized to offer on-chip, non-invasive and precise particle manipulation in aqueous environment by harnessing the optical power from the coupled laser light [14], [108]–[110]. This chapter will discuss the development of a solid-state nanopore integrated optofluidic platform by combining precise optofluidic particle manipulation technique and nanopore based label-free single molecule analysis

in a single chip. This highly sensitive platform enables amplification-free yet high-throughput biomarker analysis for molecular diagnostic applications [111], [112].

5.1 Nanopore definition, working principle, and types

A nanopore is a nanoscale opening created naturally or artificially on a thin insulating membrane, typically on the order of few nanometers in diameter [113], [114]. Under the influence of an electrical field, a nanopore enables the passage of particles with sizes smaller than its diameter in an ionic solution-filled liquid environment. Fig. 5.1a illustrates the nanopore working principle. Usually, a direct current (DC) bias voltage is applied by Ag/AgCl electrode pair to establish a constant electrical current through the nanopore. Due to the nanopore's small dimensions, a high electric field is created near the nanopore that extends only a few micrometers into the liquid chamber known as the capture volume of the nanopore [115], [116]. Under the right polarity, a particle residing inside the capture volume, will be attracted by the electric field and translocate from the "cis" side to the "trans" side of the pore, interrupting the electrical current signal in real-time. This transient interruption of ionic current or the translocation signal encodes the physical characteristics such as, size, charge, conformation etc. of the translocating particle. The blockade depth (ΔI) and translocation time (Δt) can be extracted from the translocation signal as shown in fig. 5.1a and a careful analysis of these parameters forms the basis of label-free single molecule analysis technique [117]–[120].

Generally, nanopores can be divided into two broad categories: biological, and solid-state nanopore (ssNP). The very first nanopore based analysis was done with a naturally

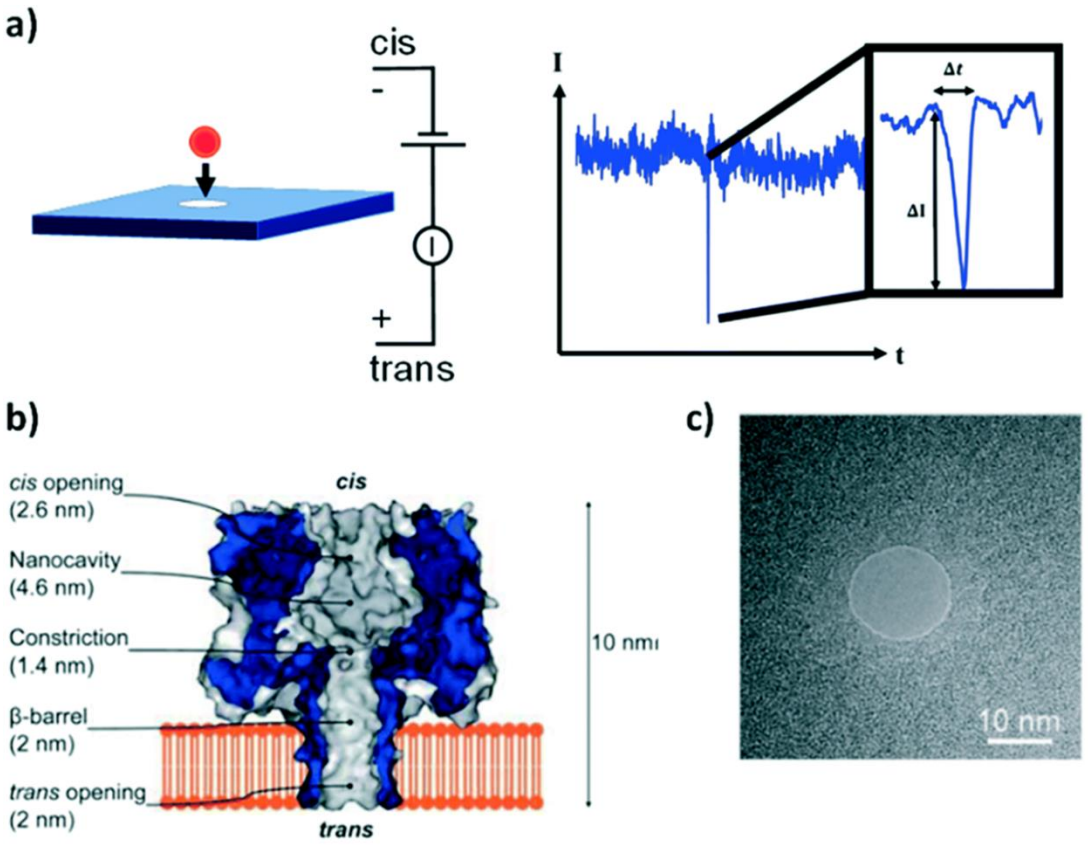

Fig. 5.1 a) Schematic presentation of a nanopore working principle and sensing ionic current signal. b) Cross-section of an alpha-hemolysin biological nanopore (from [128]). c) TEM image of a solid-state nanopore (from [114]).

available biological protein pore, α-hemolysin of diameter 1.4nm at its narrowest point [121] (see fig. 5.1b). The experimental setup for the biological nanopore is constructed by inserting the nanopore, here the α-hemolysin protein, into an insulating biological lipid membrane [122]. Later, various protein pores and viral connectors [123], [124] have been explored as biological nanopore for probing nucleic acids, proteins and other complex biomolecules [125]–[128]. Biological nanopores provide excellent signal to noise ratio, and are capable of distinguishing difference among nucleic acid bases forming the basis of next generation nucleic acid sequencing technique [129]–[131]. However, a biological nanopore has a fixed diameter, limited stability and it is hard to

produce and purify biological nanopores at a large scale challenging its integration with synthetic systems and devices for custom application [132].

To overcome these challenges, researchers utilized nanotechnology to fabricate nanoscale size hole in thin solid-state insulator membrane such as Si_3N_4, SiO_2 etc. that mimics the functioning of a biological nanopore [133], [134]. Fig. 5.1c shows a 12nm diameter solid state nanopore (ssNP) milled in a 60nm thick SiO_2/SiN/SiO_2 membrane using a focused electron beam [135]. Over the years, researchers explored several other methods for ssNP fabrication including ion beam drilling [136], chemical etching [137], dielectric breakdown [138], and nanopipette [139]. ssNPs are durable, mechanically stable, and easily integrable with chip-scale systems[48]. Also, size tunability and easy nanopore array fabrication allows for high-throughput target screening with broad size range [141]–[143]. So far, ssNPs have shown excellent performance detecting DNA, RNA, protein, small molecules, whole virus, extracellular vesicles (EVs) etc. from clinical samples [112], [144]–[150]. Henceforward, this thesis will focus on ssNP for optofluidic integration.

5.2 Nanopore integration with ARROW optofluidic platform

The solid-state nanopore has the capability to be easily integrated with microfluidic systems offering vast applications [114]. Our lab previously demonstrated techniques to integrate solid-state nanopores in the optofluidic region of the ARROW device [151], [152]. As the top cladding layer of the LC channel is made of electrically insulating materials such as SiO_2, it is possible to sculpt a thin membrane on the liquid channel

using a focused ion beam based etching process. Later, a nanopore can be milled to gain access to the liquid channel. However, milling a straight wall into the 6µm thick top oxide layer can result in a non-uniform membrane where the membrane will be thicker at the center compared to the four corners where the ion beam etching rate is higher.

We have created a terraced microwell structure using Nanometer Pattern Generation System (NPGS) software control system to obtain a uniform membrane avoiding the edge effects [111]. The terraced microwell consists of 5 nested rectangular areas for sequential FIB milling process starting with the largest one. Fig. 5.2a-c shows schematic illustrations of the LC channel cross-section with the milled terrace microwell and a nanopore. The milling was performed with a 30kV gallium ion beam

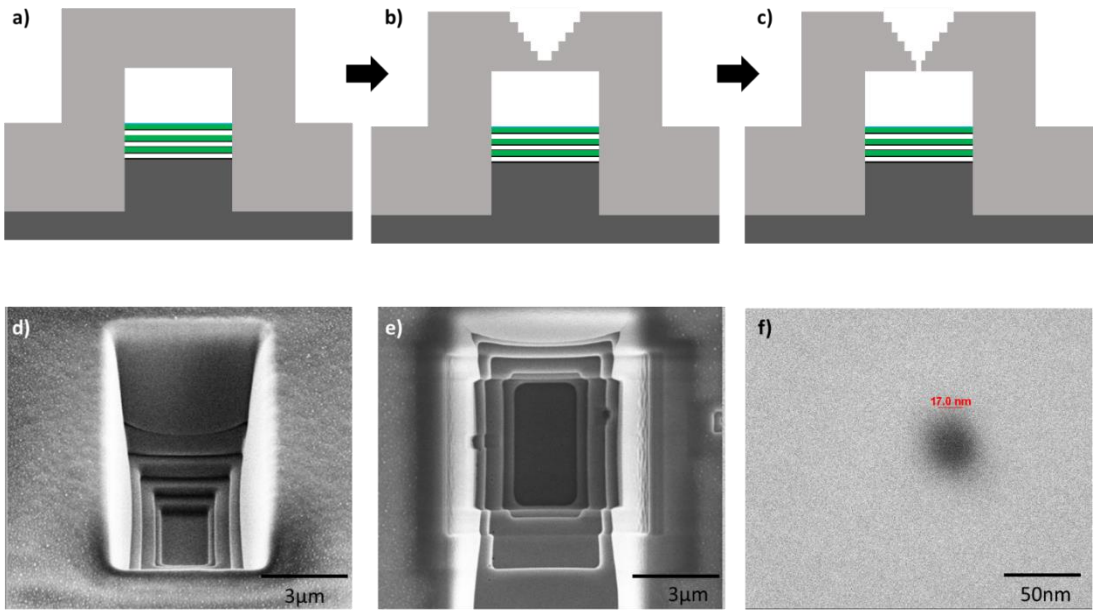

Fig. 5.2 Solid-state nanopore integration with ARROW optofluidic platform. a-c) Terraced microwell and nanopore milling steps on the LC channel using FIB. d) 52° tilted and e) top-down SEM image of the terrace microwell. f) SEM image of FIB milled 17nm diameter nanopore (from [111]).

at 5nA current for the first two rectangles and at 1nA current for the rest of the three rectangles. The last rectangle is milled in discrete steps due to slight variations in oxide thickness and/or milling rates. The milling is stopped when a uniform dark area is visible, indicating a large fraction of incident electrons can pass through without scattering. Additional 300pA milling steps are added if further thinning of the membrane is needed. The nested rectangles are aligned in such a way that opens a window for simultaneous electron beam monitoring of the microwell floor as the focused ion beam and the electron beam create a 52° angle with each other. Fig. 5.2d-e shows 52° tilted and top-down SEM image of the terrace microwell milled on the LC channel surface. Finally, a ~17nm nanopore is milled with single spot exposure of a 10pA ion beam controlled with NPGS (fig. 5.2f).

5.3 Nanopore integration with nanomembrane device

Another easy way to obtain a uniform thin insulated membrane on top of the LC channel is to start with a nanomembrane with known thickness. So, the milling time can be reduced to avoid any temporal and spatial fluctuation in the ion-beam current. Such a 300nm thin membrane has been fabricated by Prof. Hawkins' group at Brigham Young University using the help of the natural meniscus formed by flowing sacrificial SU-8 polymer into a microfluidic channel patterned in a Silicon wafer [153]. Moreover, with careful channel geometry design, an intersecting solid-core ridge waveguide has been coupled to the microfluidic channel for light-matter interaction [154], [155].

5.3.1 Nanomembrane optofluidic device fabrication

The nanomembrane fabrication process utilizes silicon nanofabrication process on a flat 100mm diameter silicon wafer. First, a basis for a 3mm long optofluidic channel structure was defined by anisotropically etching the silicon substrate based on a predesigned mask in an STS ICP Multiplex ASE RIE/ICP tool. The microfluidic channel mask comprises of multichannel inlets and outlets for particle delivery, a 100μm long optofluidic region for light-matter interaction and a 20μm long protrusion cavity for creating a low fluid flow space for nanopore integration and particle trapping. The etched channel is 10μm high and 14μm wide. A second RIE etching step defined the liquid channel thickness to be ~2.5μm and provided a pedestal for intersecting solid-core (SC) waveguides, which is 3μm lower than the top of the liquid channel to align the optical mode profile of the waveguides with the center of the optofluidic

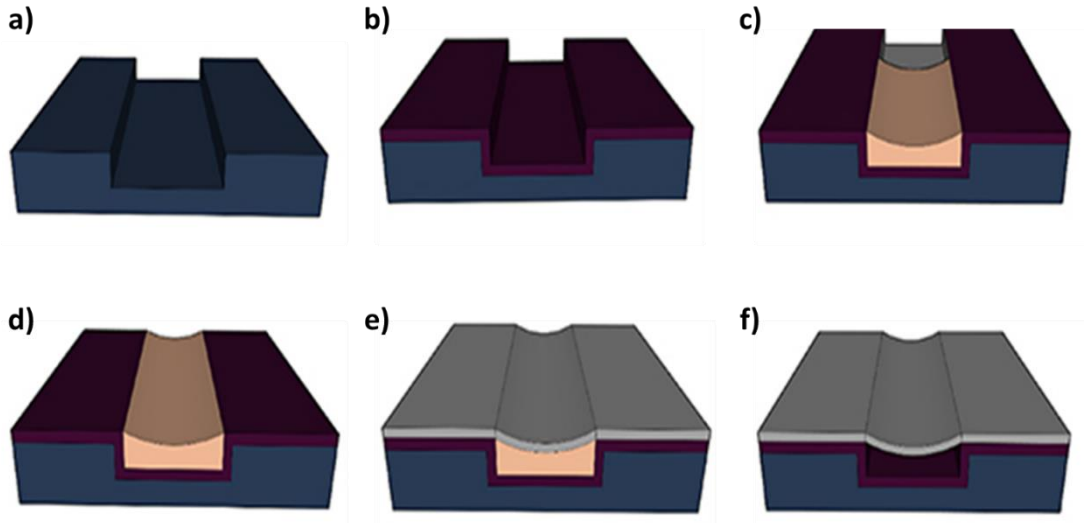

Fig. 5.3 Fabrication steps of the nanomembrane device. a) Microchannel definition on Si wafer with RIE etching. b) Thermal conversion of Si to SiO_2. c) Introduction of SU-8 sacrificial polymer into the channel. d) SU-8 meniscus pinned at the top of the channel. e) 300nm thin PECVD grown SiO_2 membrane supported and shaped by SU-8 meniscus. f) sacrificial polymer removal. (from [153])

channel. The channel wall was then thermally converted from silicon to silicon-dioxide in a furnace at 1100°C for 10.5h so that visible wavelength light can be introduced from an intersecting solid-core (SC) waveguide to the optofluidic channel. A 3µm thick PECVD silicon-dioxide layer deposition step is added afterwards to define a smooth liquid channel floor and future solid core waveguide. A 300nm thin PECVD silicon dioxide membrane was grown to cover the microfluidic channel after filling out the channel with a sacrificial polymer (SU8-2000.5). The naturally formed meniscus of the sacrificial polymer supports and shapes the thin membrane. In order to provide mechanical strength to the membrane, a 2µm thick low index silicon dioxide was deposited all over the channel excluding the central optofluidic region. The sacrificial polymer was finally removed by a combination of strong acids (1:1 mixture of H_2SO_4 and H_2O_2) to create a hollow channel with 300nm thin suspended silicon dioxide membrane in the optofluidic region paving an easier way to integrate a solid-state nanopore sensor to the optofluidic device. Fig. 5.3a-f shows step by step fabrication steps of the nanomembrane on the liquid channel.

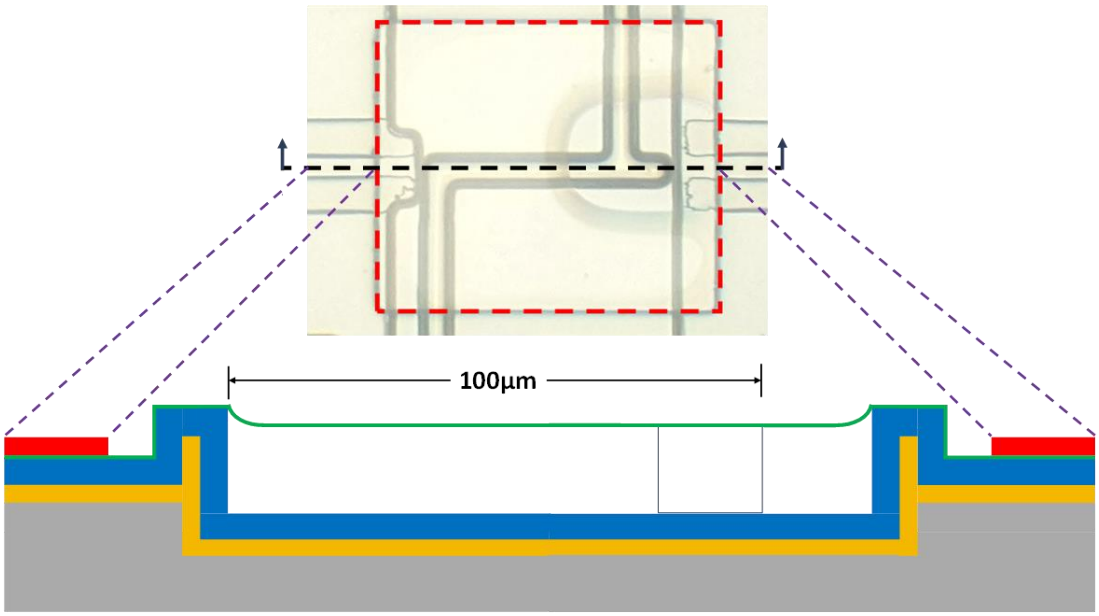

Fig. 5.4 Cross-sectional view of the nanomembrane optofluidic device with different oxide layers indicated in different color.

Simultaneously, a waveguide mask was used to etch a pedestal into the silicon substrate which provides a basis for the intersecting solid-core (SC) optical waveguide and fig. 5.4 shows a light microscope image of the fabricated nanomembrane device with 300nm thin membrane indicated by the red rectangular region and cross-sectional view of the optofluidic region indicating the thickness of different layers. To make the waveguide, the silicon pedestal surface was first thermally converted to low-index silicon dioxide (in yellow, t = 2µm, n = 1.44) which acts as the bottom cladding layer of the waveguide and then a 3µm thick high index PECVD layer (in blue, t = 3µm, n = 1.51) was patterned to form a 10µm x 3µm (w x h) waveguide core layer. The channel is selectively covered by a 300nm thin suspended silicon dioxide nanomembrane (in green) inside the red dashed region, where the rest of the area has an additional thicker

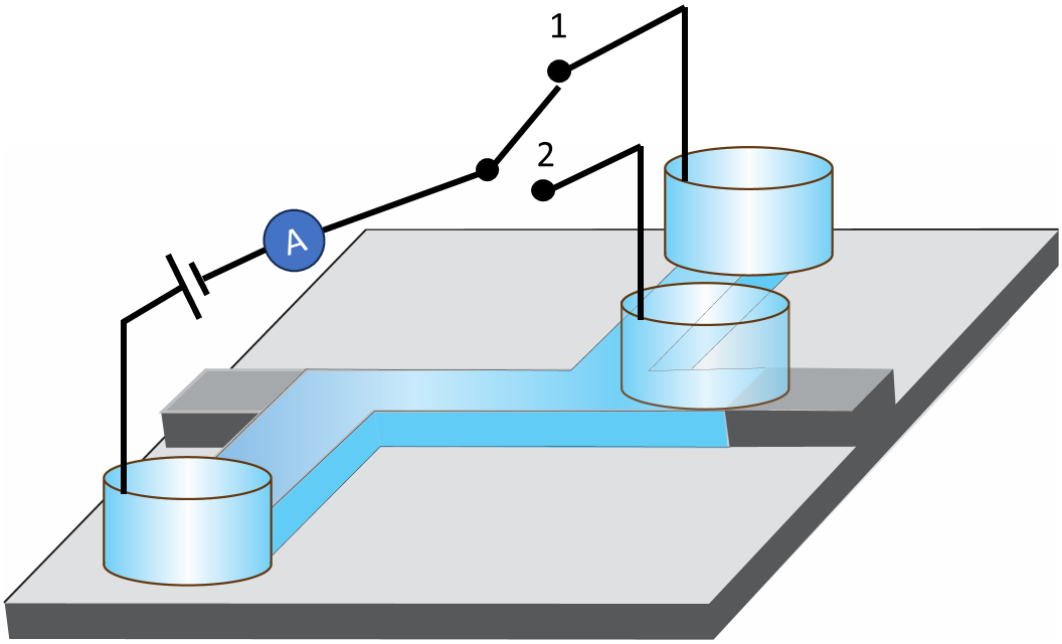

Fig. 5.5 Experimental setup for electronic voltage-current based 300nm thin membrane intactness test.

low refractive index silicon dioxide layer (in red, t = 2μm, n = 1.44) acting as cladding layer for the waveguide as well as for providing mechanical protection to the chip.

An electronic voltage-current measurement was performed to confirm intactness of the 300nm thin oxide membrane before the nanopore milling process as shown in fig 5.5. The inlet and outlet of the microfluidic channel are accessed by wax mounted reservoirs and a third reservoir is mounted on the central optofluidic region where the membrane thickness is 300nm. The reservoirs and the channel are filled with 1xT50 (50mM NaCl, 10mM Tris-HCl) salt solution. With a DC voltage application system and Ag/AgCl electrode pair, electrical current along the microfluidic channel was observed when the SPDT switch was at position #1. If the switch was moved to position #2, leakage current across the 300nm thin membrane was recorded. For an intact membrane device

before nanopore milling, a non-zero ionic current between the inlet-outlet reservoirs and a zero current between the inlet-central reservoirs is expected.

5.3.2 Nanopore fabrication

Similar to the ARROW optofluidic device, a solid-state nanopore is integrated to the nanomembrane device by milling a microwell for obtaining a uniform and thin insulated membrane inside the protrusion cavity on top of the microfluidic channel first. The steps are shown in fig. 5.6. Fig. 5.6a shows a SEM micrograph of the 300nm meniscus shaped SiO_2 membrane where the microwell is drilled. Fig. 5.6b illustrates a top-down view of a 2μm diameter microwell made by milling with 30kV, 10pA focused ion beam for 8~9 minutes controlled by NPGS software. This time, a circular shape microwell design is chosen to avoid the edge effects originating from the sharp corners

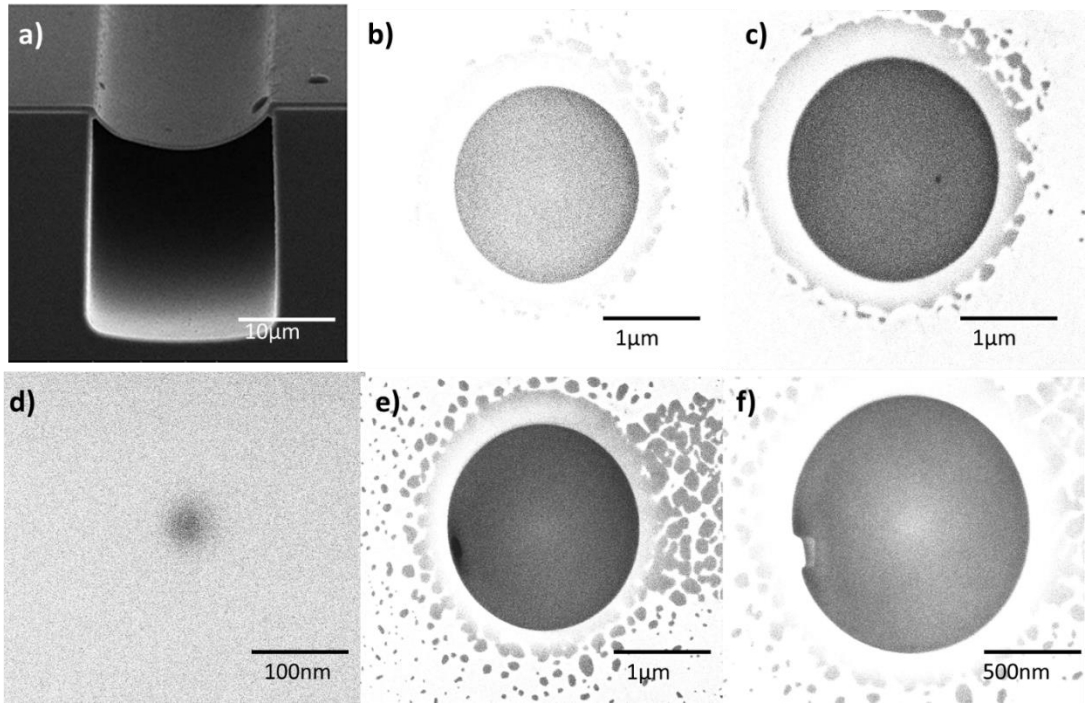

Fig. 5.6 Step by step SEM micrograph illustration of microwell and nanopore fabrication on nanomembrane optofluidic device.

in the rectangular microwell design described in section 5.2. The microwell is located at the center of the channel's top surface and 8.6μm away from the protrusion wall (see fig. 5.4). Fig. 5.6c shows top-down view and fig. 5.6d shows a zoomed in view of a ~20nm nanopore milled in the membrane. NPGS (Nanopattern Generation System) parameter: Ga FIB, 30kV, 10pA, single dose, dwell time: 14~20ms. Due to nonuniformity or the meniscus shape of the membrane, cracks can appear at the edge of the microwell (fig. 5.6e). If so, microwell fabrication is stopped immediately and the crack is patched with tetraeythlorthosilicate (TEOS) based SiO_2 deposition until the crack is invisible in the microwell membrane (fig. 5.6f).

5.4 Optofluidic particle manipulation

Optical trapping and particle manipulation techniques are very popular as they are non-invasive and contact-free methods [156], [157]. Optofluidic devices with intersecting solid-core and liquid-core waveguide provide excellent ways to precisely manipulate particles for on-chip single particle analysis, sorting, and pre-concentration applications [14], [108]–[110]. The optical force exerted on the manipulated particle is generated from the change of optical momentum while the light rays pass through a particle with different refractive index than the surrounding medium as shown in fig. 5.7. The component of the optical force acting along the beam direction is called "scattering force" and the other one acting along the intensity gradient (perpendicular to the beam direction for a collimated beam) is called "gradient force". Fig. 5.7 shows the origin of optical force on a spherical particle illuminated by light. The momentum carried by the incoming light is labeled as P_i and the ray reflected at the first surface

and the one transmitted (after two refractions at the surrounding environment and particle interface) are indicated as P_r and P_t. The change of momentum ($P_i - P_t$) of each incident rays generates optical force F. In the case of a homogeneous laser beam, the resultant force on the particle pushes it a horizontal direction along the light propagation direction, as the gradient force components cancel out each other (fig. 5.7a). However, in case of a gaussian beam where the intensity profile of the beam changes along the vertical direction and the particle sits off-axis with the optical axis, the particle is pushed towards the optical axis by the gradient force as well as pushed towards the propagation direction by combined scattering force (fig. 5.7b).

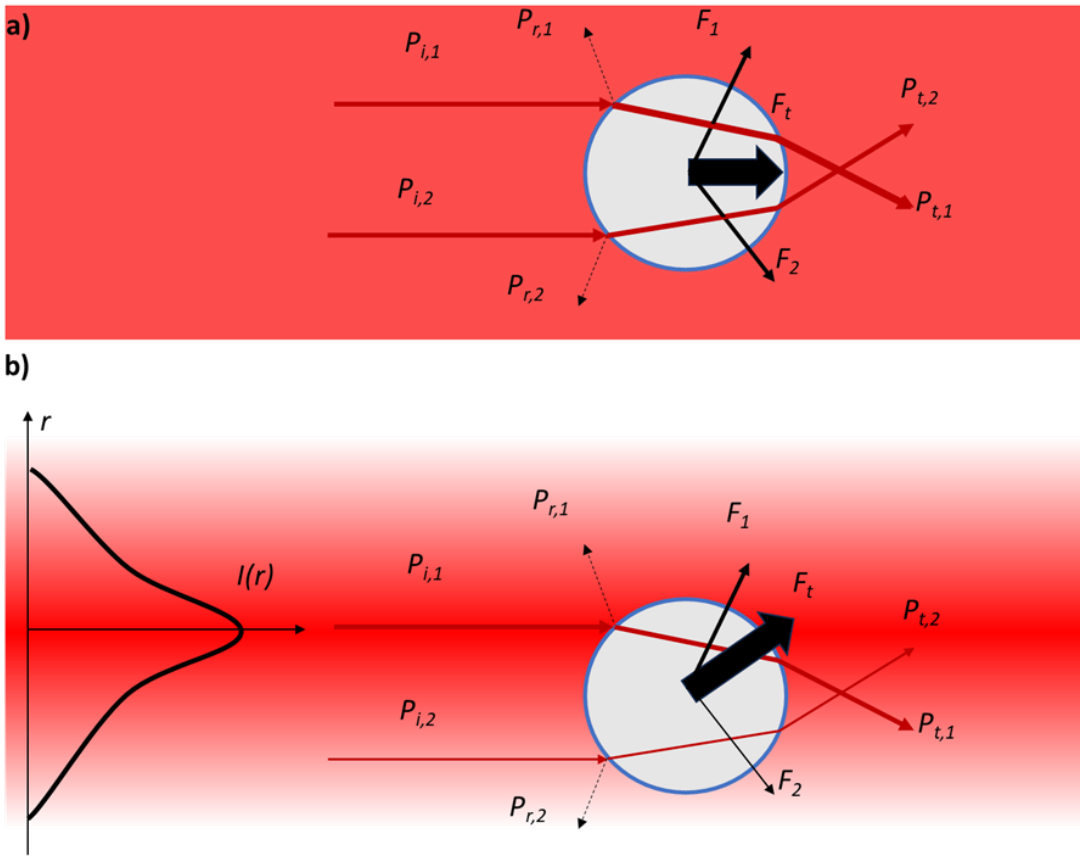

Fig. 5.7 Demonstration of optical scattering and gradient force on a particle exerted by a) homogeneous, b) Gaussian laser beam.

5.4.1 Optical trapping in ARROW optofluidic device

The ARROW optofluidic device usually uses single mode or multimode interference waveguide orthogonally intersected with liquid core channel for exciting fluorescently labeled particles flowing inside the channel under vacuum pressure as described in section 2.6. The emitted fluorescence signal is guided through the liquid core channel based on the ARROW principle and then collected with a solid core collection waveguide for off-chip signal collection process. For a symmetric design, both sides of the horizontal optofluidic channel are terminated with solid core collection waveguide. So, the same chip can be utilized for optical particle manipulation by coupling laser lights to the collection waveguides. The coupled light from both left and right side can propagate through the liquid core channel and interact with the particles flowing through it. Such an optical trapping scheme is shown in fig 5.8a, where particle is flowing slowly from the inlet reservoir under a small liquid height difference based gradient force. Inside the central optofluidic region, the optical intensity is maximum at the center of the LC channel so if a particle moves to the central part slightly off-axis or close to the channel wall, the optical gradient force will pull the particle to the center of the waveguide first and then the scattering force will push the particle along the channel toward the propagation direction. Usually, the gradient force is zero when a particle stays at the center of the channel. However, as the light propagates through the liquid channel, the scattering force goes down due to waveguide propagation loss. Eq.

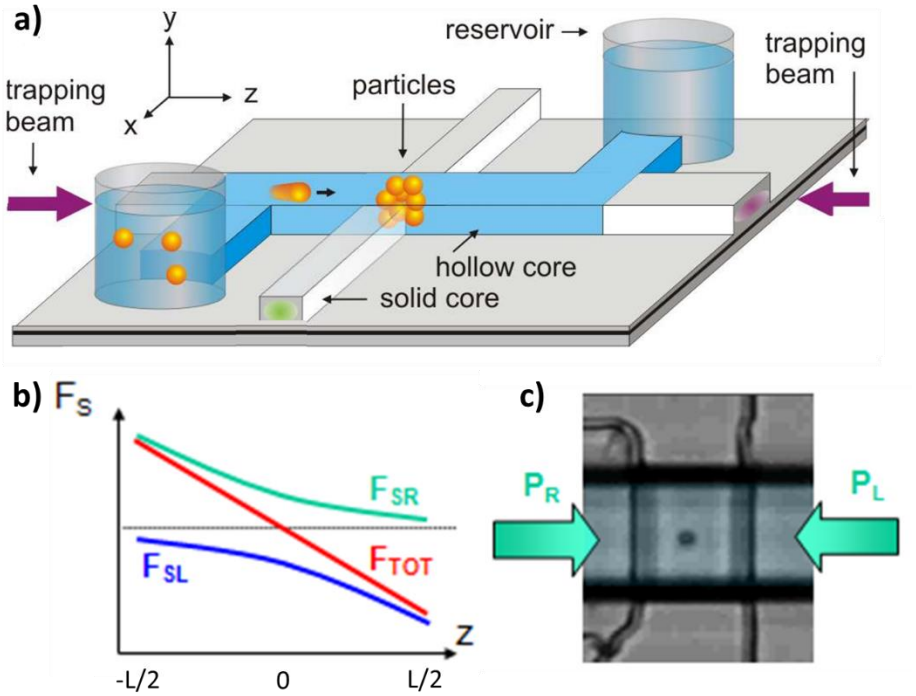

Fig. 5.8 Schematic illustration of dual-beam loss-based optical trapping scheme. a) Experimental setup for LB trap in ARROW optofluidic platform. b) Scattering force distribution along the optofluidic region. c) A single microbead trapped inside the liquid channel using LB trap. (from [110])

5.1 demonstrates exponentially decaying equation for scattering forces F_{SR} and F_{SL} due to the right and left optical beam respectively.

$$F_{\frac{SR}{SL}}(z) = \pm\frac{Qc}{n}P_{\frac{R}{L}}^{0}\exp\left(-\alpha\left(\frac{L}{2}\pm z\right)\right) \tag{5.1}$$

Here, Q is the radiation pressure efficiency, c is the speed of the light in vacuum, n is the refractive index of the surrounding medium, α is the waveguide loss coefficient, L is the optofluidic region length, and $P_{\frac{R}{L}}^{0}$ is the input beam power at the ends of the optofluidic region (z = ±L/2). Fig. 5.8b shows that for symmetric input optical beams, the total force ($F_{tot} = F_{SR} - F_{SL}$) along the ARROW liquid channel is zero at z = 0 marking the equilibrium position where the particles moving inside the channel will be

trapped. This optical trapping scheme is named as loss-based (LB) trapping as it relies on propagation loss of the waveguide. The LB trap is very flexible and the equilibrium position can be moved along the optofluidic region by carefully adjusting the optical beam power. Fig. 5.8c shows a single microbead trapped by LB trap inside the ARROW optofluidic platform. Previously, this LB trapping scheme has demonstrated trapping of ~120 microbeads inside the LC channel showing a promise of on-demand particle delivery and pre-concentration for on-chip ultrasensitive particle detection and processing [15], [110].

However, this optical trapping scheme is very sensitive to the liquid flow inside the channel and balancing two optical beams increases experimental complexity. Later, a single optical beam based optical trapping scheme was introduced where particles are flown through the channel at opposite direction to the optical propagation direction [111], [158]. Fig. 5.9 shows the experimental setup for the single beam trapping scheme in an ARROW optofluidic device. If the optical scattering force stronger than the particle flow velocity, the beads are trapped against the channel wall right after entering

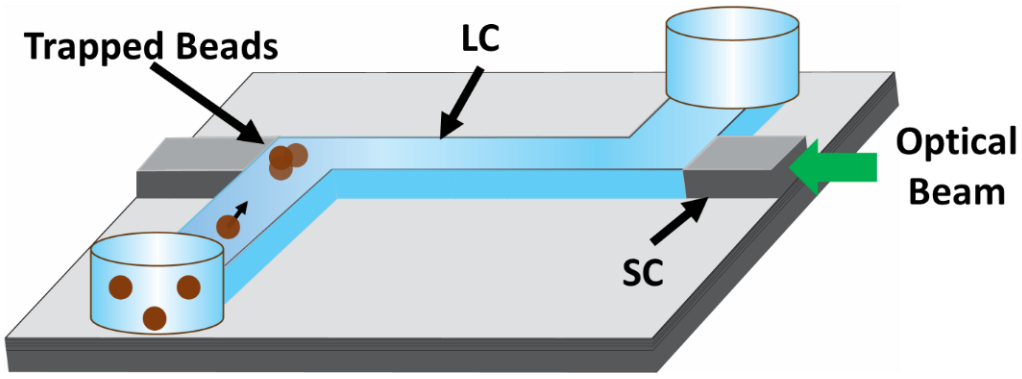

Fig. 5.9 Single beam optical trap in ARROW optofluidic device.

into the optofluidic region. This scheme reduces experimental complexity and offers reproducible optical trapping location.

5.4.2 Optical trapping in nanomembrane optofluidic device

Although the single beam optical trapping provides precise trapping location, better reproducibility and flexibility, the beads remained exposed to fluid flow while being trapped. A sudden increase in fluid flow or change in flow direction can wash away the trapped beads. A possible improvement idea can be to isolate the trapped beads from the fluid flow into a protrusion cavity where the fluid flow speed is minimum. Such an idea was implemented on the nanomembrane optofluidic device and two different optical waveguide designs were explored. The fabrication details of the nanomembrane optofluidic device are discussed in section 5.3.1. The first design involved an orthogonal optical waveguide with respect to the particle flow direction, so the optical

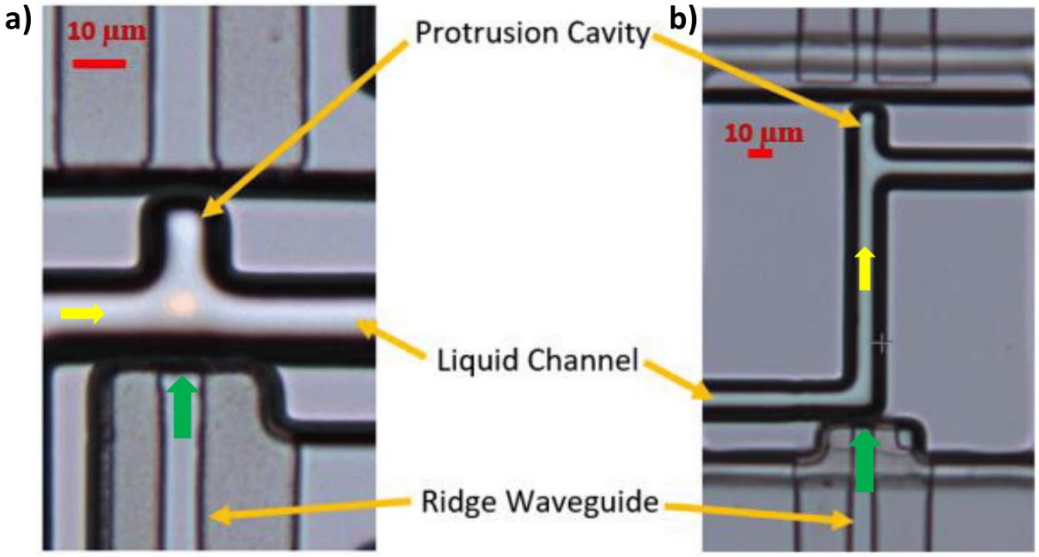

Fig. 5.10 Single beam optical trapping in nanomembrane optofluidic platform. Optical microscope image of the nanomembrane optofluidic device with a) orthogonal force design and b) gradient force design (from [155]). Green arrow: optical beam; yellow arrow: particle flow direction.

scattering force can push the particles towards protrusion cavity (see fig. 5.10a). This scheme is called orthogonal force design. The second design has an aligned optical waveguide with respect to the particle flow direction inside the optofluidic region, so the gradient force can first align the particle in the center of the channel and then the scattering force in combination with the fluid flow can easily push the particle towards protrusion region (see fig. 5.10b). This scheme is referred to as the gradient force design. The detailed characterization of these designs can be found in reference [155]. Under typical experimental conditions, the combined gradient and scattering force design showed higher optical trapping efficiency (~98%) compared to the orthogonal trapping method (80%).

5.5 Magnetic bead based solid-phase extraction method

This chapter explores the application of solid-state nanopores as a label-free single-molecule analysis tool, where target molecules are devoid of optical labeling, and their characteristics are encoded in the electrical detection signal. Ideally, similar types of particles should generate the same detection signal while translocating through the nanopore. However, statistical analysis of nanopore translocation signals originated from a single type of particles shows a spread in the detection signals which may raise ambiguity in case of differentiating among different particle types with close biophysical or chemical characteristics i.e., different nucleic acid sequences of equal length [159]. While using a solid-state nanopore for analyzing an unprocessed complex biofluid such as whole blood, plasma, urine, nasal swabs etc. the quantity of the target biomarker inside the experimental biofluid volume can be very low compared to other

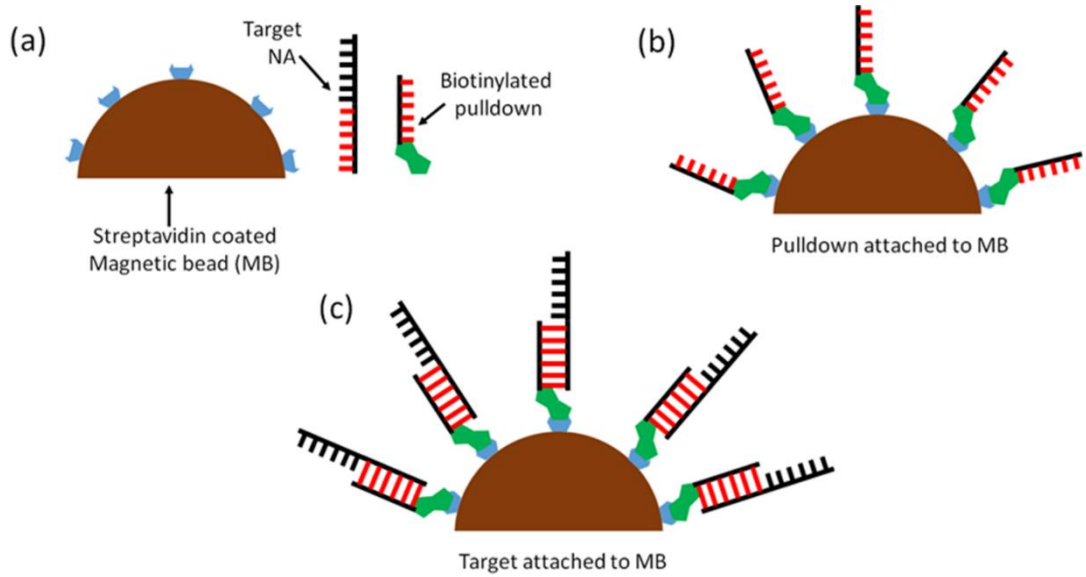

Fig. 5.11 Step by step illustration of magnetic bead based solid-phase extraction of specific nucleic acid target (from [158]).

constituents, which can limit the signal to noise ratio as well as the detection rate [47], [160]. It may take tremendous computational effort to successfully recognize a desired event from a pool of unwanted signals. Moreover, for being nanoscopic in size, nanopore can be easily blocked if an untreated raw biofluid is run through it. To avoid unwanted interference from various components of the biofluid other than the target molecule, an additional sample pre-processing step is required.

Magnetic bead based solid phase extraction method is one of the most utilized methods for extracting specific nucleic acid or protein target from complex biofluids [161], [162]. Fig. 5.11 shows the workflow of the magnetic bead based solid-phase extraction assay targeting nucleic acid. Fig. 5.11a shows all constituents of the assay, including a streptavidin coated magnetic microbead, target nucleic acid, and biotinylated short single strand DNA or pulldown sequence that is designed to be the reverse complement of a small part of the target nucleic acid (see red colored part in the target NA in fig.

5.11a). First, the magnetic bead surface is functionalized with the short pulldown sequence by streptavidin and biotin complex formation (fig. 5.11b). This interaction takes place at room temperature. After the binding process, excess unbound biotinylated pulldown sequences are discarded by magnetic washing process. Afterwards, target nucleic acids are specifically extracted from the biofluid by nucleic acid hybridization reaction between the target and pulldown sequence (fig. 5.11c). For this reaction to happen, target nucleic acid solution is first unfolded by heating at 95°C inside a programmable heating block for 5 minutes and then pulldown modified magnetic bead solution is added. After a short incubation period, another magnetic wash is performed, and next the target immobilized magnetic beads are suspended in the working buffer solution. This bead solution can be used for further downstream application. The immobilized nucleic acid targets can be released on demand just by heating the processed carrier bead solution at a higher temperature than the melting temperature of the pulldown sequence.

5.6 Nanopore capture radius and detection rate

A simple theoretical study of the nanopore target capture process translocation event is a diffusion limited process [115], [116]. Even though an electric bias voltage is applied using a pair of electrodes dipped in the ionic solution across the insulating membrane, most of the applied electric potential is dropped near the nanopore. Due to the nanoscopic size of the nanopore, a high electric field is generated near the nanopore extending over a finite volume known as the nanopore capture volume. The electric field inside the capture volume is so high that any charged particle with proper polarity residing inside this volume will be immediately captured by the nanopore. This phenomenon has been well studied by researchers and the capture volume inside the "cis" side of the pore has been modeled as a semi-hemisphere with a radius defined as capture radius (r) [115], [116]. However, for a typical millimeter scale flow cell, most of the target particles reside outside of the nanopore capture volume facing almost zero effective electrophoretic force. So, the nanopore capture process can be explained by

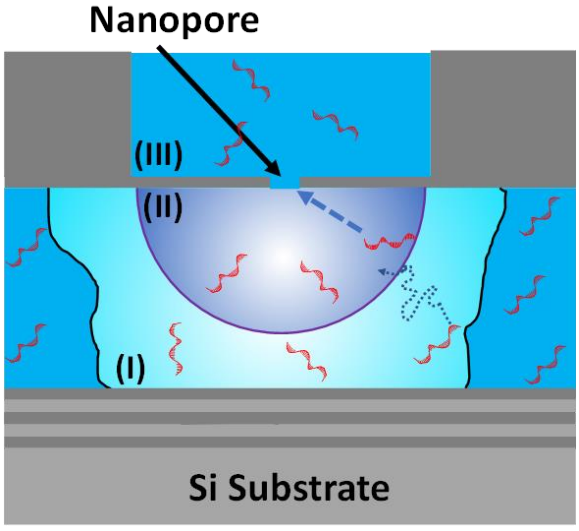

Fig. 5.12 Nanopore target capture process.

dividing the space near a nanopore into three segments, such as - i) diffusion region, ii) capture volume, and iii) “trans” side. Fig. 5.12 demonstrates the segments in the case of a nanopore integrated microfluidic channel. The diffusion region is defined as the region outside the capture volume from where the target molecules can diffuse towards and get inside the capture volume within the experiment running time. Any particle inside the capture volume is rapidly captured by the nanopore and the translocated particles are stored inside the “trans” side. The nanopore target capture rate (R) for a uniformly distributed particle concentration can be defined by Fick’s law [163] as-

$$R = 2\pi CDr \tag{5.2}$$

Here, C is the bulk concentration and D is the diffusion coefficient of the target biomolecule. For a diffusion limited nanopore experiment, it is possible to calculate the capture radius from the detected translocation rate. An experiment utilizing a ~20nm nanopore integrated ARROW optofluidic platform was conducted to target SARS-CoV-2 RNA segments at a bulk concentration of $5x10^8$/mL, revealing a calculated capture radius of 13.4μm [111]. Assuming a uniform distribution of the target within the 5μm high, 12μm wide, and 3mm long liquid channel, only $1/35^{th}$ of the total available targets will reside within the capture volume. As the clinically relevant target concentration ranges from 10^3 to 10^6/mL [47], [160], the anticipated targets inside the capture volume fall below 1, requiring prolonged experiment times to accumulate a sufficient number of molecules within the capture volume. This limits the nanopore applications in molecular diagnostics without adding target pre-amplification or pre-concentration steps. The next section will discuss an elegant solution to increase target

concentration inside the capture volume by integrating precise optofluidic microbead trapping techniques with on-chip solid-state nanopore sensor.

5.7 Optical trapping assisted nanopore capture rate enhancement (TACRE)

As discussed in the previous section, it is necessary to increase target concentration inside the nanopore capture volume in order to analyze a bio sample at clinically relevant concentration. Several methods have been explored for facilitating analyte delivery to the nanopore capture volume including pressure controlled target delivery [164], salt gradient based capture rate enhancement [165], nanopore integrated plasmonic structure for thermophoretic target capture [166], dielectrophoretic trapping of target molecules [167], Isotachophoresis (ITP) based extraction, preconcentration and delivery of target molecule to the nanopore [168]. However, a complete diagnostic assay for efficient delivery of selective biomarkers from a complex biofluid to the nanopore sensor in a label-free and amplification-free manner for attaining a higher detection throughput is still not fully accomplished.

We have recently developed a nanopore integrated optofluidic approach known as optical trapping assisted nanopore capture rate enhancement (TACRE) for obtaining specific, high-throughput, ultra-sensitive yet simple quantitative biomarker analysis [169]. The idea is to immobilize target molecules on micron size functionalized magnetic bead surface with high specificity utilizing solid-phase extraction method, and then optically trap and pre-concentrate the beads near the nanopore drilled on the integrated optofluidic channel. Simultaneously releasing the target particles from the

trapped microbeads and performing nanopore capture offers a significantly enhanced detection rate, resulting from the substantial increase in target local concentration (C_{local}) within the capture volume (V_{cap}) compared to the initial bulk concentration (C_{bulk}). Considering a lossless target release and capture process, the enhancement factor can be calculated using eq. 5.3 where N_{xloc} is the total number of target translocation observed.

$$Enhancement\ factor = \frac{C_{local}}{C_{bulk}} = \frac{\frac{N_{xloc}}{V_{cap}}}{C_{bulk}} \tag{5.3}$$

This target local concentration enhancement enables amplification-free direct detection of nucleic acid and protein targets using a nanopore with single-molecule sensitivity. Depending on the TACRE assay preparation protocol and the number of trapped beads, it is possible to get ~10^6x enhancement factor. In comparison with a PCR reaction, the obtained local concentration enhancement factor is close to the maximum amplification factor achieved from a 20-cycle long PCR reaction (For a 100% efficient PCR amplification, the amplification factor = 2^n, where n = cycle number).

Fig. 5.13a shows a schematic illustration of the experimental setup for TACRE implementation in a nanopore integrated ARROW optofluidic device. The setup utilized dual-beam loss-based optical trapping as described in section 5.4.1 for accumulating microbeads carrying target molecules at an equilibrium position along the LC channel, where a nanopore is also drilled to capture the released target particles. A cross-sectional view of the nanopore at the trapping location illustrates the TACRE process (fig. 5.13b). The effectiveness of the TACRE process was demonstrated with 100-mer ssDNA target corresponding to a melanoma cancer gene (BRAFV600E). A

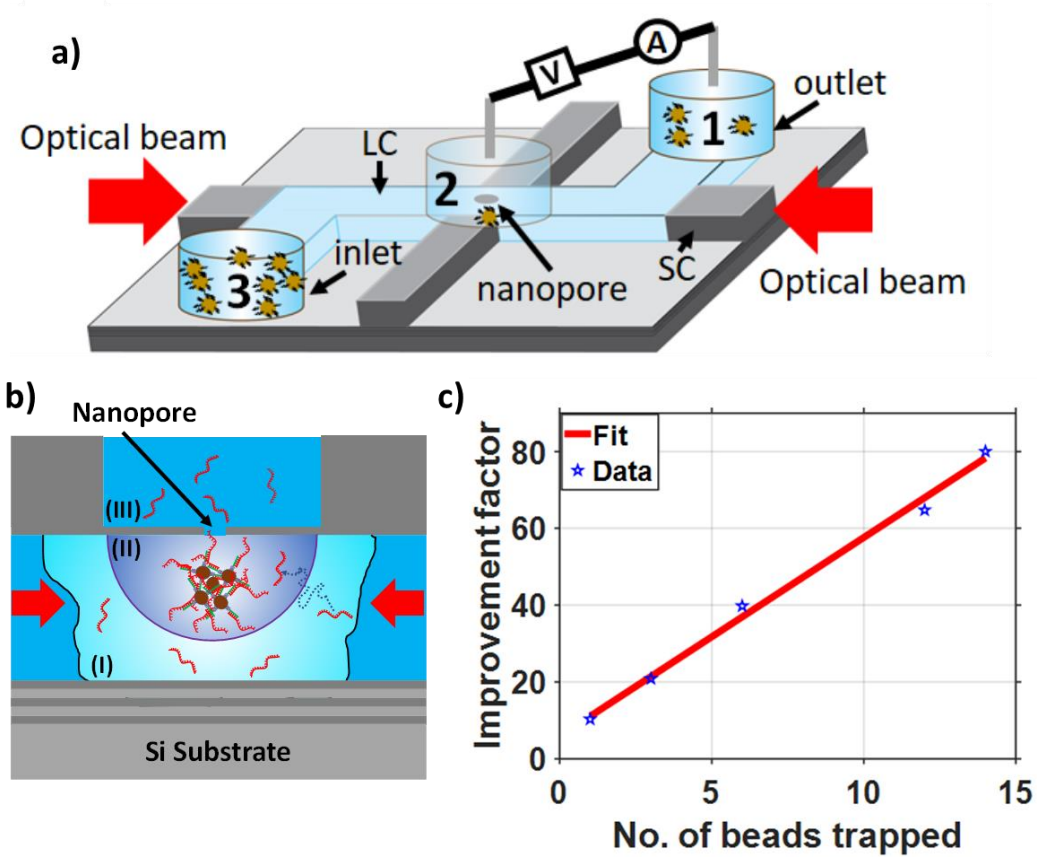

Fig. 5.13 TACRE implementation in nanopore integrated optofluidic platform. a) Schematic illustration of the experimental setup. b) Cross-sectional view of the nanopore showing trapped target carrying microbeads inside the capture volume. c) Nanopore detection rate improvement with the number of trapped beads (from [169]).

biotinylated 14bp long ssDNA pulldown sequence specific to the target was designed. First, a tenfold enhancement in nanopore detection rate is showcased when a single bead connected with 240,000 targets is trapped near the nanopore, compared to the rate achieved with the identical number of targets uniformly distributed within the LC channel. Subsequently, fig. 5.13c shows a linear rise of the nanopore detection rate with an increasing number of the trapped beads while keeping the same initial target concentration. The TACRE assay is very flexible and can be extended to different types of molecules, such as enhanced antigen detection utilizing antigen-antibody binding [158].

In the next chapters, this high-throughput TACRE process will be utilized for calibration-free quantitative analysis of target molecules. First, chapter 6 will discuss quantitative measurement of SARS-CoV-2 RNA molecules from both buffer and spiked human nasal swab sample using the TACRE assay covering the clinically relevant range. Then, chapter 7 will discuss longitudinal viral RNA load study with Zika and SARS-CoV-2 infected non-human marmoset and baboon biofluids. Finally, chapter 8 will discuss nanopore analysis of organoid derived whole exosome and TACRE based quantitative analysis of ENO1 gene, an important biomarker for metabolism, and tumor detection, from the exosome cargo.

Chapter 6 Optical trapping assisted label-free and amplification-free detection of SARS-CoV-2 RNAs with an optofluidic nanopore sensor

The global impact of the recent COVID-19 pandemic has prompted researchers worldwide to focus on the development of molecular biosensors capable of targeting a multitude of biomarkers and addressing diseases with closely related symptoms [170]–[172]. A recent survey assessing the preferred features of a COVID-19 sensor highlights the importance of incorporating high sensitivity and specificity, short turnaround time, user-friendly operation, cost-effectiveness, scalability, and seamless integration with digital platforms [59]. Designing a practical device encompassing all these sought-after characteristics has proven to be challenging. For example, the widely adopted quantitative reverse transcription-polymerase chain reaction (qRT-PCR) offers a specific, sensitive, and low limit of detection (LOD) COVID-19 testing approach, but it is complex, resource-intensive, and relatively slow [173]. In comparison, comparatively cheap, simple, and disposable lateral flow antigen testing kits provide rapid point-of-care testing with lower sensitivity and reliability [174]. Different emerging techniques such as CRISPR (clustered regularly interspaced short palindromic repeats) [175], [176], LAMP (Loop-Mediated Isothermal Amplification) [177], [178], RPA (Recombinase polymerase amplification) [179], [180], click chemistry[181] etc. are being explored to offer high sensitivity in limited resource application, but still involve optical labeling, multistep enzymatic reactions, and sensor calibration for quantitative analysis [182]. An integrated platform capable of direct,

rapid, label-free detection of individual molecular targets can overcome these challenges.

We have developed integrated nanopore electro-optofluidic chip to demonstrate the rapid, label-free, amplification-free and quantitative detection of SARS-CoV-2 RNAs with single molecule sensitivity using the optical trapping assisted nanopore rate enhancement (TACRE) approach [111]. With a highly specific TACRE assay, viral RNA was successfully detected from both buffer and clinical nasal swab samples and a wide dynamic range (10^4-10^9/mL) with LOD of 17aM has been reported. The examination of nanopore capture rate with target concentration revealed a favorable scaling by the TACRE approach towards lower concentration and a remarkable ~2000x detection rate enhancement resulting from target pre-concentration within the nanopore capture volume.

6.1 Experimental methodology

The optical trapping-assisted capture rate enhancement (TACRE) approach is implemented by combining off-chip SARS-CoV-2 assay preparation with an electro-optofluidic nanopore platform for high-throughput analysis.

6.1.1 SARS-CoV-2 assay

We used a modified version of the solid-phase extraction method described in section 5.5. Here, streptavidin coated 1μm diameter magnetic bead (purchased from New England Biolabs, Inc.) were functionalized with biotinylated 14 bp long pulldown sequence- /5BiotinTEG/CATTTCGCTGATTT (purchased from Integrated DNA

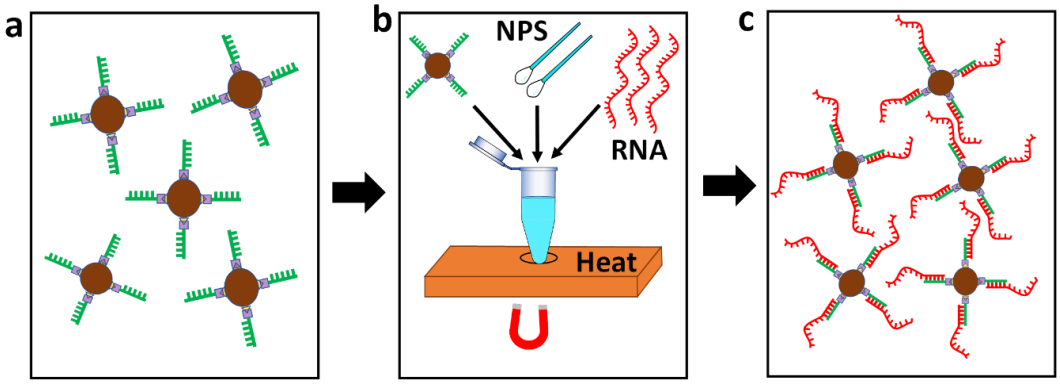

Fig. 6.1 Magnetic bead based SPE assay for SARS-CoV-2 RNA detection.

Technologies, Inc. (IDT)) targeting a part of the ORF 1ab region (nt. 28,294-28,307; Severe acute respiratory syndrome coronavirus 2 isolate Wuhan-Hu-1, complete genome, NCBI Reference Sequence: NC_045512.2) of the SARS-CoV-2 genome. The melting temperature of the pulldown is 35.1°C in 50 mM Na^+ salt solution (calculated from http://biotools.nubic.northwestern.edu/OligoCalc.html). The binding capacity of the magnetic bead is more than 500 pico-moles of 20bp biotinylated ssDNA molecules per mg. First, a 5µL aliquot of the beads at stock concentration (4 mg/mL) was washed 3x with 20nm filtered (Whatman Anotop Syringe Filters) 1XT50 (50 mM NaCl, 10 mM Tris, pH 6.5) buffer solution and then 0.5µL of 100µM biotinylated pulldown sequence was added with 6x molar excess to saturate the binding sites of each bead. The sample is incubated in a rotary mixture at room temperature for 1h. Afterwards, unbound pulldown sequence was discarded by magnetic washing and finally the functionalized beads were resuspended in 1XT50 buffer at predetermined concentration for downstream application (see fig 6.1a).

The clinical sample with predetermined target concentration was prepared by spiking negatively detected nasopharyngeal swab samples or buffer solution with synthetic

SARS-CoV-2 RNAs. Human nasal swab samples that tested negatively for SARS-CoV-2 (confirmed by RT-qPCR) were collected by the UCSC Molecular Diagnostics Laboratory. The synthetic RNA (stock concentration ranging from 10^5 to 10^6 copies/mL) including fragments from ORF 1ab, Envelope, and Nucleocapsid region of the SARS-CoV-2 genome were purchased from American Type Culture Collection (ATCC: VR-3276SD).

We have developed and characterized a calibration free and quantitative assay. For example, 20µL of spiked nasal swab sample prepared at target concentration of $5x10^8$ copies/mL was heated at 95°C for 5 minutes in a programmable heating block to melt the secondary structures in the RNA molecules and then immediately mixed with 2.5µL of pulldown functionalized magnetic bead sample at a concentration of $4x10^7$ bead/mL. The average ratio of the number of available targets to bread was 100. This assay is flexible, and the target to bead ratio can be modulated on-demand as each bead has more than 10^5 binding sites. The bead mixture was transferred to a 30°C water bath for 1 min and then the vial was gently flicked and centrifuged briefly. Afterwards, the sample was kept in a dry bath at 95°C for 1 min. The water bath cooling and dry bath heating steps were repeated four times to maximize the binding possibility of the target particles to the magnetic beads. Then the solution was kept in an ice bath for 30 min. Finally, the magnet beads went through 2x magnetic washing to discard unwanted constituents from the nasopharyngeal swab and resuspended in nanopore working buffer (1xT50 with 2% w/v sodium dodecyl sulfate (SDS)) at a concentration of 3.3×10^6 beads/mL. Fig. 3b & 3c illustrate the target extraction process and the final bead-

target construct. Though the complete extraction efficiency of the assay is unknown, the results described later in this chapter demonstrate good agreement with our expected values indicating minimal losses.

6.1.2 Integrated electro-optofluidic nanopore platform development

We have developed an integrated electro-optofluidic nanopore platform for delivering target immobilized magnetic beads near the nanopore with a higher rate. Fig. 6.2 shows schematic representation of the developed platform. At the heart of the platform there is an 8x8 mm^2 Si-based ARROW optofluidic device with intersecting solid core waveguide (in gray) and liquid core channel (in blue). A ~20nm nanopore sensor is integrated at the end of the optofluidic part of the LC channel by programmable FIB milling process. The detailed fabrication process of the ARROW device is described in section 2.5 and the nanopore integration is described in section 5.2. Three metal reservoirs are placed at the LC channel entrance (#1 and #3) and on the nanopore (#2),

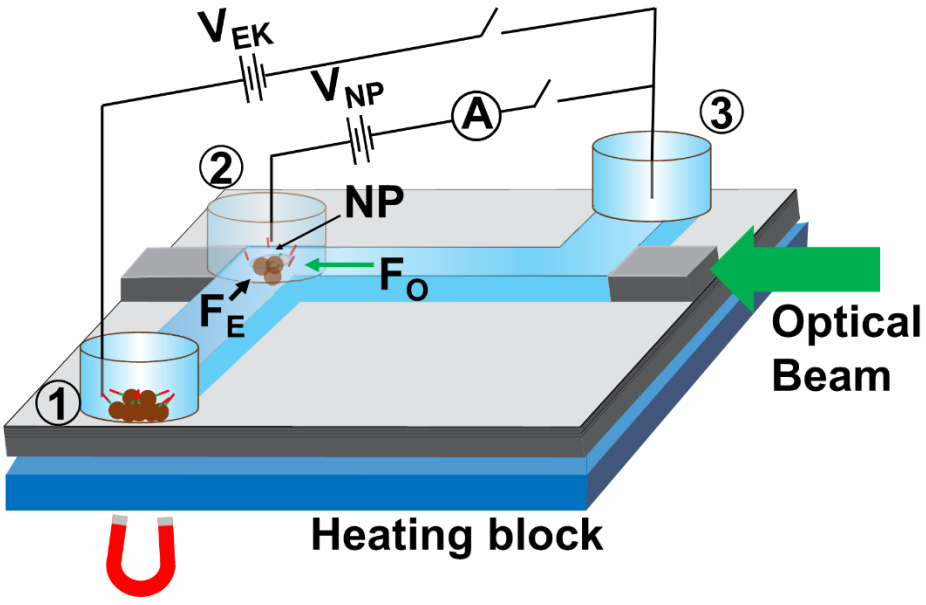

Fig. 6.2 Nanopore integrated electro-optofluidic platform.

to introduce liquid and particles inside the channel as well as for inserting Ag/AgCl electrodes for applying electrical voltage. Initially, the target immobilized beads are introduced in reservoir #1 and a brief magnetic pulling was applied (1 min) to increase the number of beads near the channel inlet. Then, a potential difference V_{EK} (usually between 6v to 12v) was applied to drive the beads to the optofluidic region by electrokinetic force. When, the SC waveguide is coupled with laser light (532 nm, Lighthouse Photonics), the optical scattering force, F_o will overcome the electrokinetic force, F_E and trap the beads against the channel wall under the nanopore sensor. Fig. 6.3a shows a timeline of optical trapping inside the optofluidic device. The magnetic beads move under the influence of F_E during timestamp $T_1 – T_2$ indicated by red arrows. The laser light was turned on at time stamp T_3 and the beads were pushed along the beam propagation direction indicated by purple arrows as $F_O > F_E$. The beads were trapped against the channel wall at timestamp T_9. In comparison with diffusion-based bead delivery method (ctrl, black bars), combined magnetic and electrophoretic bead

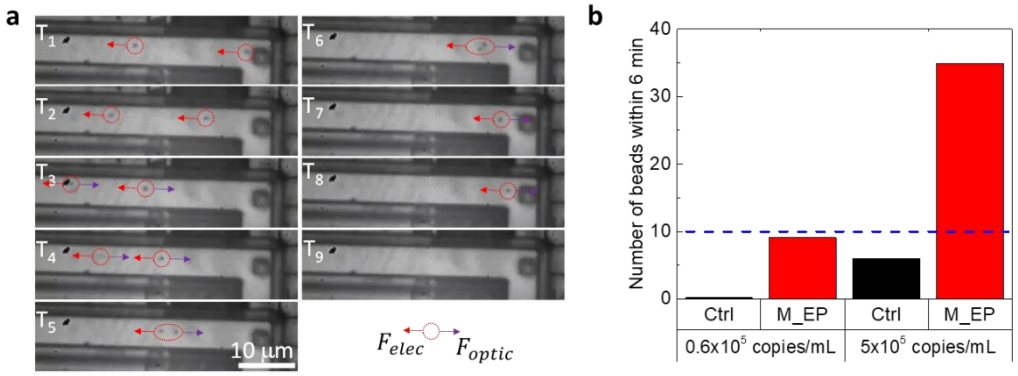

Fig. 6.3 a) Optical trapping of target carrying microbeads inside the optofluidic channel. b) Comparative analysis between purely diffusion based and combined magnetic-electrophoretic bead delivery method.

delivery method (M_EP, red bars) demonstrated superior performance as shown in fig. 6.3b.

The device is placed on a Peltier heater (TES1 12703, Hebei I.T. (Shanghai) Co., Ltd) controlled by a temperature controller (LDC 3724B, ILX Lightwave). The controller is set to 45°C, 10°C above the melting temperature of the pulldown sequence to account for heat transfer loss from the heater block to the ARROW chip and a 10kΩ resistor is placed on the heater surface to implement a closed loop PID algorithm. After a desired number of beads are trapped, the heater is turned on for thermally releasing target molecules from the magnetic bead surface inside the nanopore capture volume and a nanopore voltage V_{NP} is applied to capture the released target simultaneously. The current signal from the nanopore was amplified by a highly sensitive current amplifier (Axopatch 200B, Molecular Device) and simultaneously recorded at a sampling rate of 250KSa/s through a data acquisition module (Digidata 1440A, Molecular Device). The

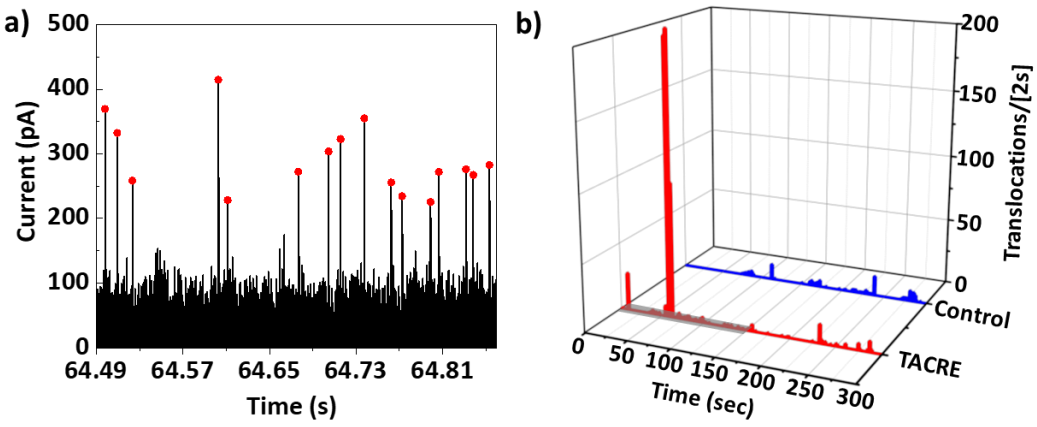

Fig. 6.4 a) Baseline subtracted nanopore translocation signal for individual SARS-CoV-2 RNA segments. b) Real-time translocations of SARS-CoV-2 RNAs from TACRE method and control experiment. The gray region in the TACRE trace represents the 150s heating period for target release.

current signal is filtered by a low pass filter (10kHz cut-off frequency) and a custom MATLAB program is used to analyze and identify translocation spikes from noise and other ionic current fluctuations [158]. The program first calculates standard deviation (SD) of the baseline current and sets up a detection threshold, here at 4x SD. In each cycle, 5 samples are collectively considered as a new data point and compared with previous data point. Real translocation events are confirmed by checking the change in consecutive data points against the user defined detection threshold, and a successful return to the baseline within a user defined time threshold (~10X longer than the expected translocation dwell time). Fig. 6.4a shows the characteristic nanopore electrical detection signal with good signal-to-noise ratio resulting from the translocation of individual RNA molecules through the nanopore (marked in red dots). The next section will discuss the performance of the TACRE assay, which shows dramatic detection range enhancement compared to stand-alone nanopore detection of target molecules from bulk solution.

6.2 Result and discussion

6.2.1 TACRE assay speed

To quantify the performance of the TACRE assay, we performed a diffusion limited nanopore experiment without any preconcentration steps at target concentration of 10^9 copies/mL. A 2s integrated translocation histogram along the experiment time (fig. 6.4b – blue trace) shows stochastic, but continuous detection of small numbers of targets due to the slow, diffusion-limited target delivery to the pore. Compared to the bulk

detection experiment, the target starting concentration in the TACRE experiment was $2x10^8$ copies/mL and the assay was prepared for each bead holding approximately 5 targets on average. After 90 target carrying beads were optically trapped, the heater was turned on for the first 150 seconds (indicated by the gray region) of the experiment runtime. The translocation histogram (fig. 6.4b – red trace) shows a sharp rise in the instantaneous translocation rate between t = 57s and t = 63s during which 75% of the total of 677 molecules were drawn through the nanopore and detected. This demonstrates the speed and effectiveness of the TACRE process.

6.2.2 Detection dynamic range

The suitability of the TACRE assay for viral RNA detection covering clinically relevant concentration range was evaluated. To do so, a series of nanopore control experiments without any preconcentration steps and optical trapping was performed with target spiked buffer solution at concentrations 10^4 – 10^9 copies/mL. The total number of detected translocations within 360s of experiment time at different bulk concentrations are plotted in fig. 6.5a. 6 minutes of experiment time represents a reasonable experiment time for point-of-care application. It was observed that the nanopore based label-free, direct viral RNA detection process becomes unreliable at 10^5 copies/mL target concentration with 2 ± 1 total translocation count observed within 360s. So, the limit of detection for the standalone nanopore detection process was determined to be 10^6 copies/mL, which misses essentially the entire clinically relevant

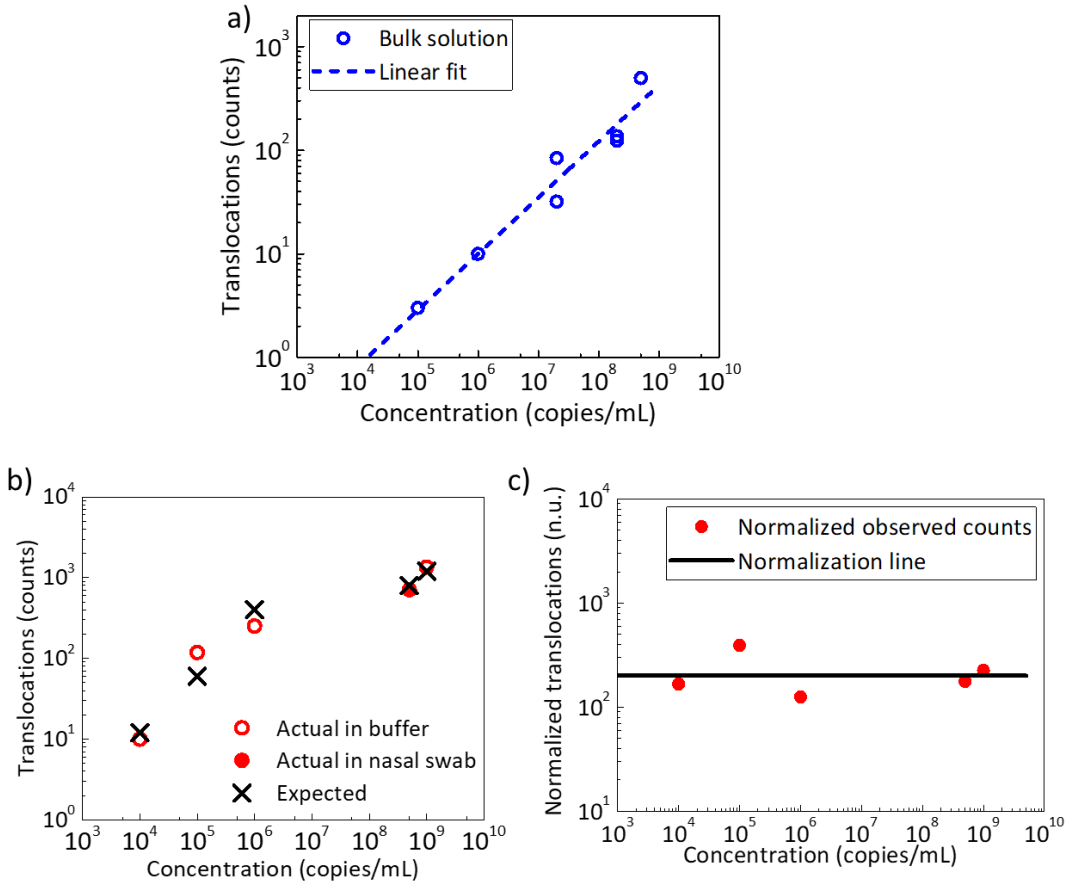

Fig. 6.5 a) Total number of translocations in nanopore control experiment at different starting viral RNA concentrations. b) Number of detected viral RNAs in TACRE method at different starting target concentrations. c) Normalized target count obtained from TACRE analysis to the case of 10 trapped beads with 20 RNAs/bead assay.

concentration range. The TACRE process can overcome this challenge as it is possible to deliver enough targets, for instance minimum of 10 targets to the nanopore capture volume by optically trapping a desired number of target carrying beads, which will be captured by the nanopore instantly upon thermal release. Fig. 6.5b shows the total observed translocation count (red circle) and expected number of molecules delivered to the nanopore by multiplying the number of trapped beads with the average number of targets per bead (black cross) in TACRE experiments with different target initial

concentration covering the entire clinical concentration range. The open red circle indicates TACRE experimental results in spiked buffer solution, where the filled circle indicates an experiment in spiked swab solution. For the spiked nasal swab sample, the TACRE assay was designed to incorporate an average of 100 targets per bead and with 8 optically trapped beads, 800 molecules were expected to translocate through the nanopore. A good agreement between the expected and observed translocation count shows a good extraction efficiency and effectiveness of the TACRE assay in case of processing complex biofluid such as nasal swab sample. It is also demonstrated that at least 10 translocation counts were observed from each TACRE experiments down to a detection of limit of 10^4 copies/mL with good agreement with the expected number of translocation count determined from the assay.

Unlike the control experiment, the translocation count in the TACRE experiments is not expected to follow a predefined trend. As a flexible assay, different target per bead ratio values (always chosen to be greater than 1) were adopted and different number of beads were trapped during these experiments resulting in different number of targets released near the nanopore. To clarify this, the experimental results illustrated in fig. 6.5b was normalized to a standard case of 10 trapped beads with 20 average target attached per bead according to eq. 6.1 and plotted in fig. 6.5c.

$$Normalized\ count = \frac{10}{trapped\ bead} x \frac{20}{target\ per\ bead} \qquad (6.1)$$

All the experimental results with good agreement between observed and expected counts are expected to have same normalized value close to 200 (indicated by black line) irrespective of the number of trapped beads and assay design. The normalized

count from the highest and the lowest tested target concentration (255 and 167 respectively) shows that the assay is equally efficient across the entire concentration range. It is also possible to conclude that the TACRE process can enable viral RNA detection of even lower target concentration overcoming the diffusion barrier by increasing the number of trapped beads, and/or mixing fewer beads with available sample volume to get higher target per bead ratio.

6.2.3 Local target concentration enhancement

The fundamental idea of the TACRE process is to increase target concentration near the nanopore sensor to enable amplification-free high throughput target counting. To quantify the local target concentration near the nanopore, the nanopore capture volume is estimated by graphical calculation in AutoCAD. Fig. 6.6a shows a schematic drawing of 5µm x 12µm LC channel and the nanopore is located (indicated by orange point) on the top of the channel, 6um away from the side wall and 3um away from the channel wall. The capture volume is modeled here as a semi-hemisphere with capture radius, r = 13.4µm which is calculated from a diffusion limited nanopore experiment as

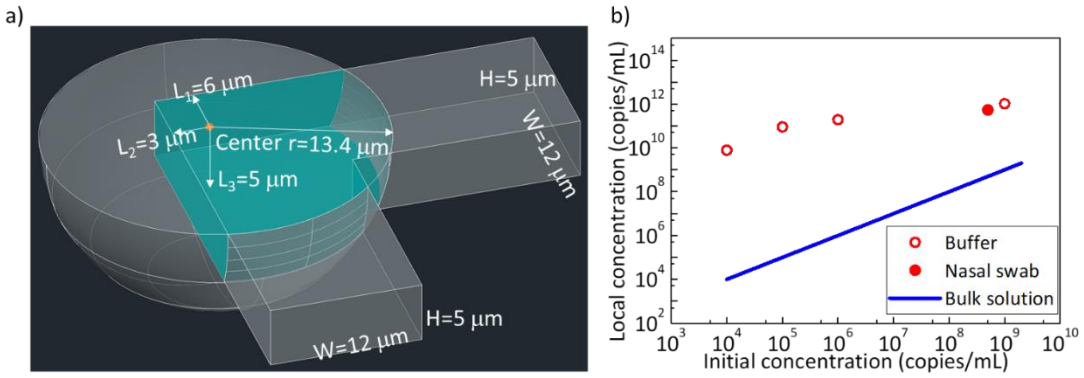

Fig. 6.6 a) Graphical calculation of nanopore capture volume. b) Calculated target local concentration near the nanopore at for different initial concentration.

described in section 5.6. Due to dimension limitations of the LC channel, the overlapped blue shaded region in fig. 6.6a is the actual capture volume, which is measured to be 1309μm^3 or 1.309pL. Now, the target concentration can be calculated for each TACRE experiment by dividing the total number of expected target particles released from the trapped beads by the actual capture volume. The calculated local concentration values for the TACRE experiments demonstrated in fig. 6.5b are plotted (red circles) in fig. 6.6b against the starting target concentration. Here, the target local concentration for the control experiments will be the same as initial bulk concentration as indicated by the blue straight line in fig. 6.6b. TACRE experimental results show favorable scaling of local concentration enhancement towards the lowest target concentration, enabling attomolar target detection while keeping the local concentration in the picomolar range. The maximum concentration enhancement of

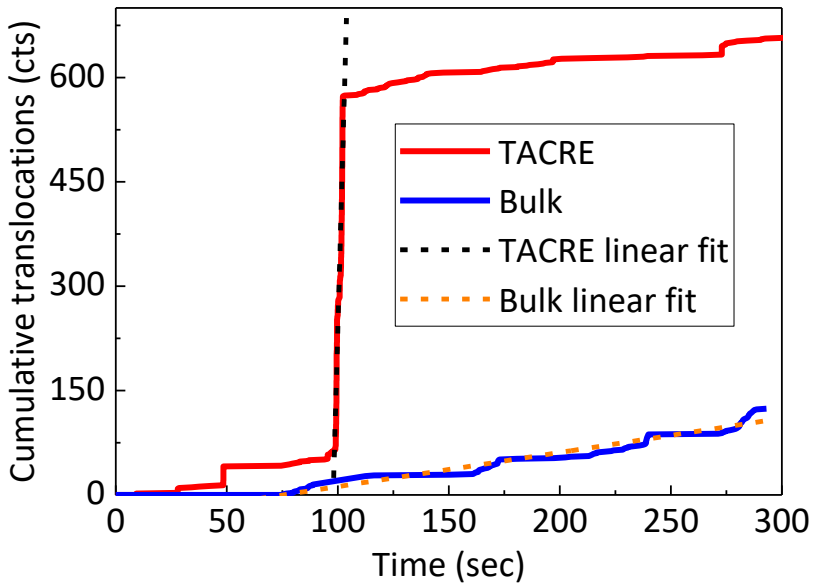

Fig. 6.7 Capture rate comparison between bulk detection and TACRE assay.

$7.8x10^5$ was observed for the lowest initial target concentration of 10^4 copies/mL or 17aM.

6.2.4 Capture rate enhancement

Finally, the target concentration enhancement near the nanopore resulted in nanopore capture rate or detection rate enhancement. The translocation detection dynamics was analyzed to quantify this enhancement factor. The blue trace in fig. 6.7 shows the cumulative translocation count obtained from the nanopore bulk control experiment performed at 10^9 copies/mL target concentration. The trace shows a continuous and stochastic detection of target particles governed by diffusion. The capture rate for this diffusion limited process can be obtained from the linear fit of this trace. However, the cumulative particle detection count for the TACRE assay shows a completely different picture (red trace in fig. 6.7). The linear fit to this trace shows a steeper slope compared to the bulk control trace. The translocation rate enhancement is defined here as the ratio of peak translocation rate at each concentration of the TACRE assay and the rate of particle counts over the 360s duration of the assay for the control case. Table 6.1 shows the enhancement factor for different initial target concentrations, and it is evident that

Table 6.1 Capture rate enhancement at different target concentration.

SARS-CoV-2 RNA (copies/mL)	Translocation rate (molecules/sec)		Capture rate enhancement
	TACRE	Control	
$1x10^6$	18	$1.67x10^{-2}$	1080
$1x10^5$	18	$8.67x10^{-3}$	**2075**
$1x10^4$	1.5	Not detectable within 360s	

TACRE assay becomes more powerful at the lower target concentration. Maximum target capture rate enhancement of 2,075x is observed at 10^5 copies/mL target concentration. As described earlier, the bulk detection scheme becomes unreliable at 10^4 copies/mL target concentration, so the rate enhancement at this concentration would nominally be infinite. A finite number of detection events and a finite enhancement factor at this target concentration can be obtained by increasing the bulk control experiment time. However, it is safe to assume that the enhancement factor will result in a larger value than the obtained maximum value of 2,075x.

Chapter 7 Nanopore integrated optofluidic platform for quantitative viral RNA analysis from primate biofluids

Infectious diseases caused by viruses can cause pandemics due to their high rate of infectivity, rapid transmission routes, variable incubation periods before showing symptoms, as well as frequent mutations in viral genome [183]–[185]. During the last couple of decades, the world has witnessed multiple viral pandemics such as Swine flu pandemic in 2009, Ebola virus pandemic during 2013-2016, Zika virus pandemic during 2015-2016 and the COVID-19 pandemic, causing huge loss of life as well as obstructing economic growth and development [186]–[188]. As preventive measures, such as vaccination, and antiviral medicine for viral infection are often either limited or unavailable, it is essential to develop simple low-cost point-of-care (POC) diagnostic technologies for public health monitoring with high accuracy and efficiency [189], [190]. The optical trapping assisted nanopore capture rate enhancement (TACRE) method can be a promising and powerful clinical diagnostic tool enabling label-free and amplification-free single biomarker detection, but with dramatically reduced complexity.

Non-human primate models play a pivotal role in advancing our understanding of viral infections and vaccine development. Their physiological and immunological similarities to humans make them invaluable for studying disease progression, immune responses, and testing vaccine efficacy [21], [22]. This chapter presents a highly sensitive quantitative study of the viral RNA concentration progression in biofluids from well-established non-human primate models, a common marmoset for Zika virus

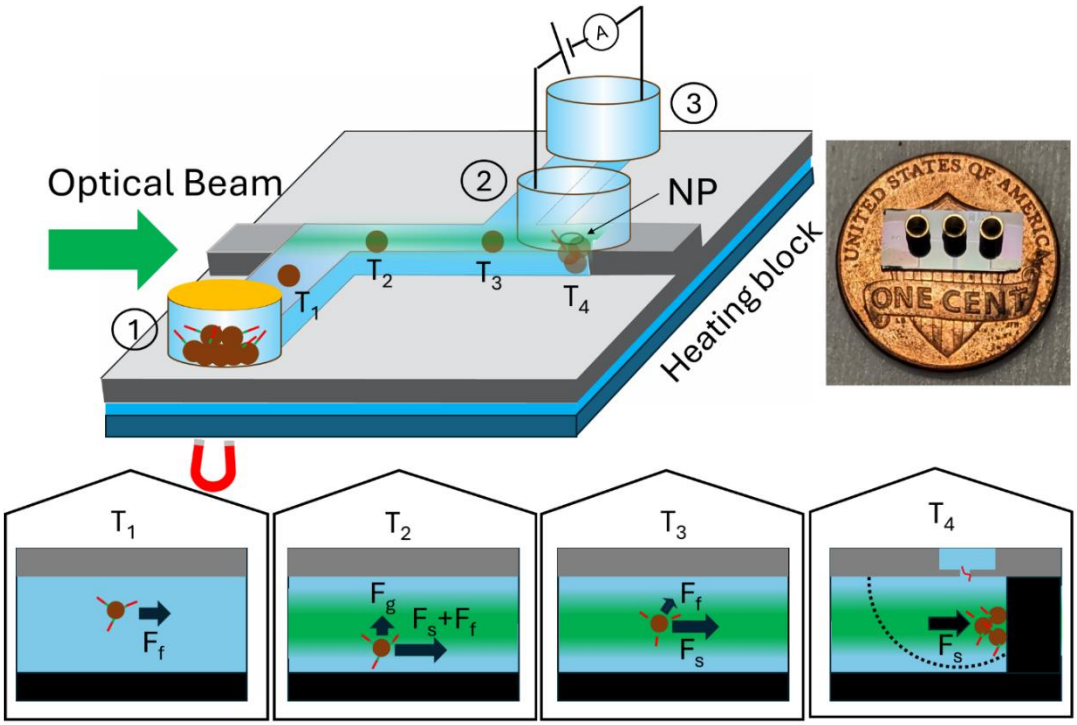

Fig. 7.1 Integrated optofluidic nanopore platform for TACRE implementation. The time points T1-T4 shows the different forces acting on the magnetic bead as it moves through the optofluidic region. Inset shows a real-life device with respect to a one cent coin.

infection, and a baboon for SARS-CoV-2 virus infection animals, using the TACRE method. Six different biofluids (Zika infected marmoset: semen, urine and whole blood; SARS-CoV-2 infected baboon: nasopharyngeal and throat swab (NPT), rectal swab, bronchoalveolar lavage (BAL)) were collected and analyzed with the optofluidic nanopore platform along a planned four-week longitudinal study. The successful quantification of viral RNAs from all six different types of biofluids in agreement with the gold-standard RT-qPCR viral load is demonstrated first. The trapping-based target local concentration enhancement allowed this amplification-free method to follow the course of infection with a detection limit of 10aM and a dynamic range of five orders of magnitude. These results show a great potential for integrated optofluidic-nanopore

platform to be a true low complexity, inexpensive continuous viral load monitoring tool.

7.1 Integrated optofluidic nanopore platform development

A schematic view of the experimental platform is shown in fig. 7.1. The platform consists of a nanomembrane optofluidic device featuring a 10μm x 10μm cross-section microfluidic channel covered with a selectively etched 300nm SiO_2 membrane. The device fabrication steps are described in section 5.3.1. At the center of the device, a 10μm x 6μm solid core waveguide intersects with the microfluidic channel and creates a 100μm long horizontal optofluidic particle manipulation region. The optofluidic region has a 20μm extended protrusion to create a low fluid flow region for isolating particles from the fluid flow and trapping them at a precise location. A 20nm nanopore is milled into the oxide membrane inside the protrusion cavity by focused ion beam (fig. 7.2a). The detailed nanopore integration method for this nanomembrane platform is provided in section 5.3.2. The nanopore capture volume (V_{cap}) was calculated by a previously described graphical method in AutoCAD [111] (see Ch. 6). Fig. 7.2b shows the cross-section of the protrusion in the microchannel (10μm height x 10μm width x 20μm length) and the nanopore is located at the center of the top surface of the protrusion (yellow dot). The capture volume is defined by the intersection between the semi-sphere with the previously calculated capture radius (13.4μm) for a similar ~20nm nanopore and the microfluidic channel (see Ch. 6). The capture volume (V_{cap}) is calculated to be 2,187 μm^3 or 2.187×10^{-9}mL. Three metallic reservoirs are attached by wax for accessing the microfluidic channel to introduce liquid and target particles

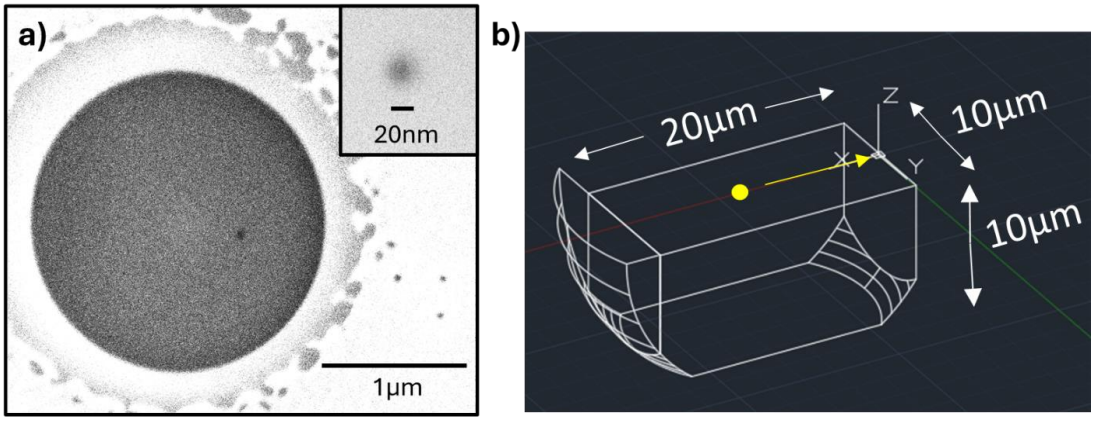

Fig. 7.2 a) SEM micrograph of milled microwell and nanopore on the thin insulating membrane. b) Graphical method of calculation for nanopore capture volume.

through the inlet (#1) and to apply an electric potential difference between the nanopore (#2) and outlet (#3) by Ag/AgCl electrodes. A highly sensitive current amplifier is connected to the platform for measuring the ionic current signal.

For optofluidic bead manipulation, a 532nm laser is coupled to the solid-core optical waveguide by a single mode fiber. The microbeads are introduced by the inlet reservoir and moved through the channel via hydrostatic pressure from different fluid heights in the reservoirs. Natural evaporation is utilized to obtain this fluid height difference. Usually, the inlet reservoir is filled with 6µL of bead solution preceded by a drop (~1µL) of mineral oil to prevent the evaporation and the outlet reservoir is filled with 6.7µL of 1xT50 buffer (50mM NaCl, 10mM Tris-HCl) only. For characterizing this particle delivery and trapping method, the cumulative number of trapped microbeads against the experiment time is plotted for three different optofluidic-nanopore devices (fig. 7.3). These experiments were performed with carboxylate-modified 1µm diameter

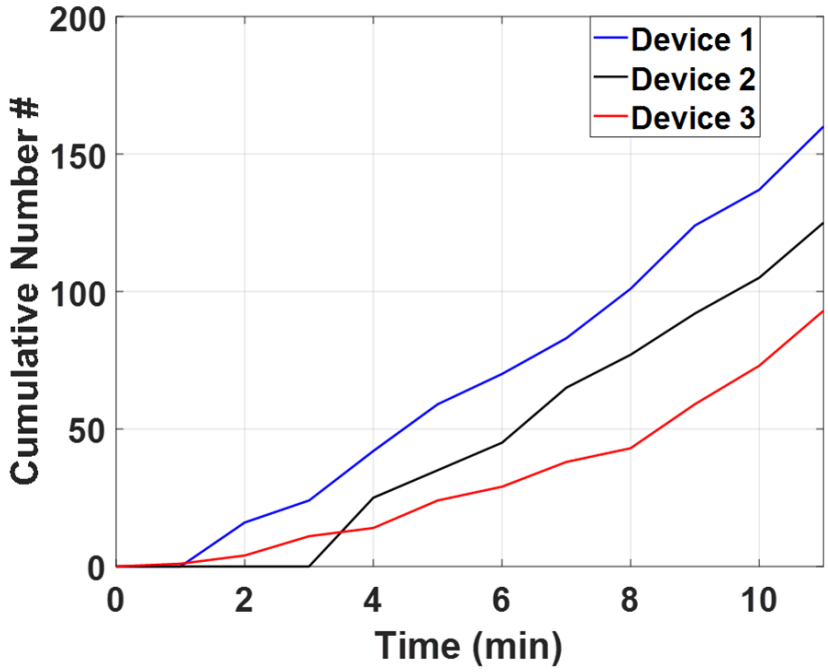

Fig. 7.3 Natural evaporation controlled microbead delivery for optical trapping.

fluorescent beads (Excitation/Emission: 625/645nm) at $4x10^7$ bead/mL concentration suspended in 1xT50 buffer with 0.5% Tween 20 surfactant. Tween 20 surfactants were added to the bead solution for avoiding bead aggregation and non-specific bead binding events to the microfluidic channel surface. Each characterization experiment takes 6µL of fluorescent bead sample. This analysis shows a good bead delivery rate with 100% trapping efficiency for more than 10 minutes. The microbead flow was monitored using a CCD camera (Andor Luca R, Oxford Instruments) connected with a custom-built microscope. A 50x long working distance objective lens (Olympus, SLMPlan, 0.45 NA, 15mm WD) was used to illuminate and collect light from the device and a 40nm bandpass filter centered at 670nm wavelength (Omega Optical LLC. 670DF40) was used to reject the laser light. Furthermore, the TACRE assay involves target carrying magnetic beads, and they are pre-concentrated inside the inlet reservoir using a brief

magnetic pull-down to improve the bead delivery rate and keep the assay time in an optimal range.

The trajectory of the target-carrying beads from the inlet to the trapping region can be divided into four distinct timepoints (T_1-T_4) where various combinations of forces act upon a bead (fig. 7.1-bottom panel). First, when a bead enters the microfluidic channel (timepoint T_1), it experiences fluid flow induced force F_f. The bead doesn't experience any optical force before it reaches the horizontal optofluidic region. At the waveguide-channel intersection, the optical beam exerts both gradient (F_g) and scattering force (F_s) on the microbead providing a net optical force based on the refractive index of the microbead and the surrounding medium (timepoint T_2). The SC waveguide is aligned with the microfluidic channel, so the optical mode profile of the SC waveguide lines up with the channel cross-section. Optical mode simulation of this optofluidic region has been described before in [155]. The scattering force acts in the direction of light propagation, pushing the particle along the channel in the same direction as the fluid flow where the gradient force is a 3-dimensional force acting perpendicular to the light wave propagation and pulls the bead towards the center of the channel where the light intensity is maximum. At the microchannel and protrusion junction (timepoint T_3), if the optical beam power is enough to provide a stronger scattering force compared to the fluidic flow, the bead will be pushed towards the protrusion cavity away from the fluid flow. The fluid flow inside the protrusion cavity is negligible so the beads pushed inside this region will experience only the scattering force F_s, enabling optical trapping of the beads against the cavity wall (timepoint T_4). This way the target carrying

magnetic micro particles are efficiently trapped against the cavity wall near the nanopore sensor.

7.2 Primate biofluid processing and solid phase extraction based TACRE assay

7.2.1 Biofluid collection

The virus infected non-human primate biofluid collection and analysis was performed in collaboration with Prof. Jean L. Patterson lab from Texas Biomedical Research Institute (TBRI). All experimental procedures with animal samples were approved by the Institutional Animal Care and Use Committee of the Texas Biomedical Research Institute (IACUC, #1714 PC and #1528 CJ 10), and the University of California Santa Cruz (IACUC, #Schmh2104 and #Schmh 2207dn).

A male marmoset (*Callithrix jacchus*) was inoculated with Zika virus and three different bodily fluid (urine, whole blood, and semen) were sampled and serially monitored. The inoculation and sample collection method were described previously in ref[22]. The urine sample was collected on days 3, 5, 7, 9, 11, and 13 (considering the date of viral inoculation as day 0). The whole blood sample was collected on days 1, 3, 6, 9, and 28. The semen sample was collected on days 9, 14, and 28. Similarly, a baboon (*Papio hamadryas anubis*) was inoculated with SARS-CoV-2 virus and three different bodily fluids (bronchoalveolar lavage, nasopharyngeal throat swab, and rectal swab) were sampled and serially monitored as described in [191]. The bronchoalveolar lavage (BAL) was collected on days -7, 2, 14, 21, and 28. The nasopharyngeal throat

swab (NPT) and rectal swab sample was collected on days -7, 0, 2, 7, 10, 14, 18, 21, and 28.

7.2.2 RT-qPCR control experiment for viral RNA quantification

A gold standard RT-qPCR control experiment was conducted for obtaining viral load from all these samples. I thank Bernadette Guerra and Kendra Alfson from TBRI for the qRT-PCR based viral load analysis. For independent viral load reference measurements, total ZIKV RNA was isolated from bodily fluids (semen, saliva, and urine) using TRIzol LS reagent (Invitrogen) according to the manufacturer's instructions. 10µg of yeast RNA as a carrier and 30µg of Glycoblue Coprecipitant (Invitrogen) was added during the extraction procedure. The RNA pellet was re-suspended in a volume of 50µL nuclease free water and 5µL of RNA was used to

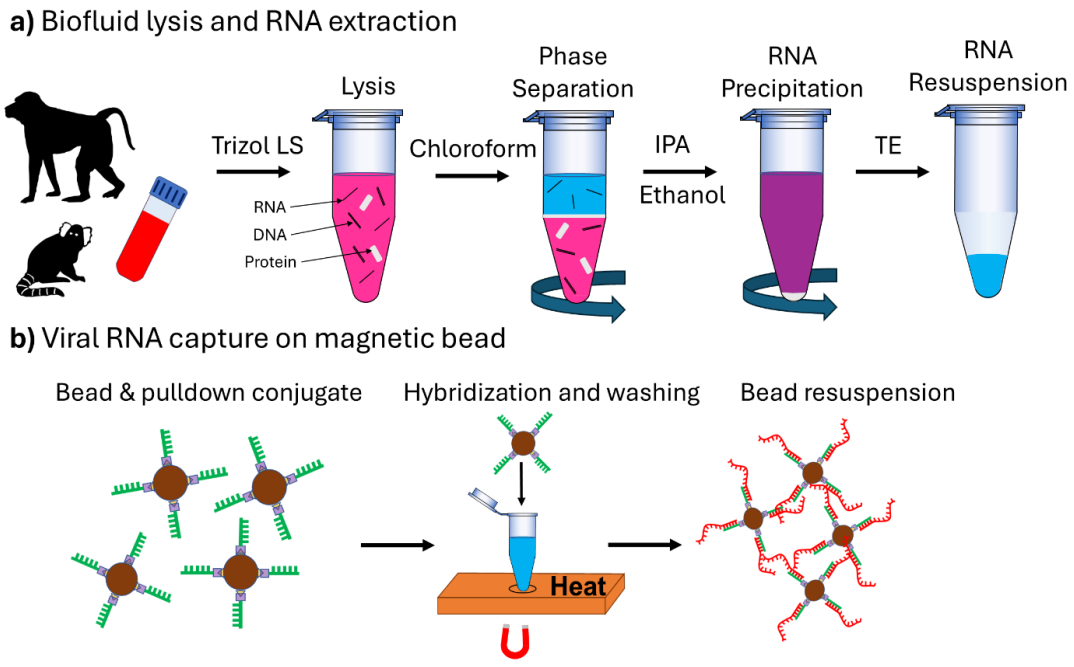

Fig. 7.4 TACRE assay preparation steps for viral RNA detection from animal biofluid.

quantify the viral titer. Quantitative RT-PCR was performed using RNA Ultrasense One-Step RT-PCR system (ThermoFisher) on an Applied Biosystems 7500 Real -Time instrument at 40°C for 30 minutes followed by denaturation at 95°C for 10 minutes then thermocycling for 40 cycles of at 95°C for 15 seconds and 60°C for 1 minute. The sequence of the ZIKV primers used are forward 5′-AAR TAC ACA TAC CAR AAC AAA GTG-3′, reverse 5′-TCC RCT CCC YCT YTG GTC TTG-3′, probe 5′-/56-FAM/CTY AGA CCA /ZEN/GCT GAA R/3IABkFQ/-3′ (Integrated DNA Technologies)[192]. SARS-CoV-2 viral RNA was quantified via quantitative reverse transcription polymerase chain reaction (qRT-PCR), as previously described [21], [191]. The CDC-developed 2019-nCoV_N1 assay was used to target a region of the N gene. Briefly, samples were inactivated using TRIzol LS Isolation Reagent (Invitrogen) and RNA extracted using the EpMotion M5073c Liquid Handler (Eppendorf) and the NucleoMag Pathogen kit (Macherey-Nagel). MS2 phage (Escherichia coli bacteriophage MS2, ATCC) was spiked in as an internal efficiency control. The TaqPath 1-Step RT-qPCR Master Mix (Life Technologies) was used for qRT-PCR, using 5μL of the extracted RNA material. Assays were performed on a QuantStudio 3 instrument (Applied Biosystems) with the following cycling parameters: Hold stage 2 min at 25°C, 15 min at 50°C, 2 min at 95°C. PCR stage 45 cycles of 3 s at 95°C, 30 s at 60°C. Primer and probe info: 2019-nCoV_N1-F: GACCCCAAAATCAGCGAAAT (500nM); 2019-nCoV_N1-R: TCTGGTTACTGCCAGTTGAATCTG (500 nM); 2019-nCoV_N1-P FAM/MGB probe: ACCCCGCATTACGTTTGGTGGACC (125nM).

7.2.3 TACRE assay preparation

Similar to the PCR analysis, the collected primate biofluids are first lysed to obtain high-quality RNA molecules by disrupting cell and cellular structures for the TACRE assay preparation. So, the TACRE assay for the primate biofluid analysis can be divided into two steps. First crude RNA is extracted from lysed biofluid (fig. 7.4a) and then magnetic bead based solid phase extraction assay for quantitative viral RNA detection (fig. 7.4b).

Here, biofluid lysis and RNA extraction is performed using TRizol LS, a phenol, guanidine isothiocyanate-based agent inside a biosafety level-2 cabinet. RNAs are easily isolated from DNA and proteins by ultracentrifugation steps (Sorvall Legend Micro 21R Centrifuge). All biofluid samples were inactivated by mixing with 750µL of TRizol LS (250µL sample + 750µL of Trizol LS) maintaining a ratio of 3:1 between the volume of Trizol LS and the sample. If the volume of sample was less than 250µL then 1xPBS was added to bring the volume of sample to 250µL. 200µL of chloroform was added and mixed to the lysed sample tube by pipetting up and down. The tube was then centrifuged for 15 minutes at 12,000 × g at 4°C followed by a 3 min incubation period at room temperature. The clear upper aqueous layer (approximately 600µL), which contains RNA, was carefully transferred to a new 1.5mL tube. To precipitate RNA, 500µL of isopropanol (IPA) was added to the transferred liquid and mixed. The sample was then centrifuged for 10 minutes at 12,000 × g at 4°C followed by a 10 min incubation period at room temperature. The supernatant was discarded, and the remaining pellet was resuspended by vortex in 1mL of 75% ethanol. The sample was

again centrifuged for 5 minutes at 7,500 × g at 4°C. Extra ethanol was discarded and the RNA pellet was air dried for 20 minutes. The isolated total RNA was eluted by 30-50μL of nuclease-free water (Invitrogen) or 1xIDTE buffer (10mM Tris, 0.1 mM EDTA) by flicking the tube. Finally, the RNA solution was incubated in a water bath set at 55–60°C for 15 minutes. For quantitative analysis, biofluid volume is properly tracked throughout the sample preparation steps. The resuspended RNA sample is then used for downstream assay preparation steps.

The magnetic bead based solid-phase extraction method relies on biotinylated short ssDNA sequence. Two 14 base pair long biotinylated ssDNA pulldown sequences (Zika: 5'- /5BiotinTEG/GTTTTGGTATGTGT -3' and SARS-CoV-2: 5'-/5BiotinTEG/CATTTCGCTGATTT -3') were purchased from Integrated DNA Technologies (IDT). The melting temperature of both pulldown sequences in 50mM Na^+ salt is 35.1°C (http://biotools.nubic.northwestern.edu/OligoCalc.html). The pulldown sequence for Zika viral RNA quantification experiment was designed to complement a part of NS5 region of the viral genome (nt. 9275 – 9288; Zika virus strain ZikaSPH2015, complete genome, NCBI Reference Sequence: KU321639) and the pulldown sequence for SARS-CoV-2 experiment was designed to complement a part of ORF1ab region of the viral genome (nt. 28,294-28,307; Severe acute respiratory syndrome coronavirus 2 isolate Wuhan-Hu-1, complete genome, NCBI Reference Sequence: NC_045512.2). The streptavidin coated magnetic microbeads of 1μm diameter (4mg/mL) were purchased from New England Biolabs (NEB). The beads bind with 500 pmol of single-stranded 25 bp biotinylated oligonucleotide per mg which

translates to 240,000 pulldown binding sites per bead offering a wide dynamic range for viral RNA concentration analysis. The magnetic bead surface is first functionalized with this specific pulldown sequence by streptavidin-biotin based attachment process. These attached pulldown sequences offer specific hybridization sites for the viral genes. For pulldown bound magnetic bead preparation, 5μL of the stock magnetic bead ($2x10^7$ beads) were magnetically washed and resuspended in 20nm syringe filtered 1xT50 buffer solution. The washed magnetic beads were then added to biotinylated synthetic capture pulldown oligomers so that the ratio between the number of available binding sites and the number of pulldown oligomers is 1:6. The sample was well mixed in a rotary mixture for 1 hour and the unbound excess pulldown sequences were discarded by magnetic wash. Afterwards, the pulldown functionalized beads were resuspended at a suitable concentration (10^7 – 10^5 beads/mL) for downstream sample preparation.

7.2.4 Quantitative viral RNA analysis using TACRE assay

Usually, a known number of pulldown functionalized beads are (N_{beads}) mixed with the RNA sample ($V_{biofluid}$). For an error free RNA extraction, the resuspended RNA sample should have all the viral RNAs available in the biofluid. Also, for an efficient solid-phase extraction process, all the viral RNAs should be immobilized on the magnetic bead surface maintaining a mean value for RNAs to bead ratio. A subset of these beads ($N_{trapped}$) are optically trapped near the nanopore and the cumulative number of translocations (N_{xloc}) gives the total number of attached RNAs on the trapped magnetic bead surface. This provides an estimated number of viral RNAs attached per bead

($f_{xloc:bead}$) as shown in eq. 7.1. The number of RNAs in the biofluid (N_{RNA}) can then be determined as eq. 7.2. And, finally the concentration of the viral RNA (C_{RNA}) from an unknown biofluid can be estimated by TACRE assay according to eq. 7.3.

$$f_{xloc:bead} = \frac{N_{xloc}}{N_{trapped}} \tag{7.1}$$

$$N_{RNA} = N_{beads}\, x\, f_{xloc:bead} \tag{7.2}$$

$$C_{RNA} = \frac{N_{RNA}}{V_{biofluid}} \tag{7.3}$$

This quantitative TACRE method is calibration-free unlike qPCR. The choice of the number of pulldown functionalized beads (N_{beads}) mixed with the RNA sample is critical for obtaining lower LODs. A lower number of beads can target a lower number

Table 7.1 Zika infected marmoset biofluid sample preparation summary.

Sample	Day 3	Day 9	Day 14
Blood	N_{bead} = 4200 $f_{RNA:Bead}$ = 1.88 $V_{biofluid}$: 250µL $f_{xloc:bead}$ = 2.9 $N_{trapped}$ = 21 N_{xloc} = 61	Not Detected	N/A
Urine	Not Detected	N_{bead} = 600 $f_{RNA:Bead}$ = 1.42 $V_{biofluid}$: 500µL $f_{xloc:bead}$ = 15.5 $N_{trapped}$ = 2 N_{xloc} = 31	N/A
Semen	N/A	N_{bead} = 625 $f_{RNA:Bead}$ = 472 $V_{biofluid}$: 62.5µL $f_{xloc:bead}$ = 655 $N_{trapped}$ = 4 N_{xloc} = 2620	N_{bead} = 12000 $f_{RNA:Bead}$ = 2.03 $V_{biofluid}$: 250µL $f_{xloc:bead}$ = 5.3 $N_{trapped}$ = 10 N_{xloc} = 53

of RNAs, offering a very low LOD. However, a lower number of magnetic beads inside the optofluidic device requires longer analysis time for getting a finite number of beads trapped inside the nanopore capture radius. To keep the experimental analysis time within an optimum range for the lowest viral loads, the number of beads was chosen to result in approximately 1-100 targets per bead based on the qPCR reference measurements. In the absence of a qPCR value, a viral load of 10^3/mL was assumed. A list of assays and experimental parameters are demonstrated in table 7.1 and 7.2.

Table 7.2 SARS-CoV-2 infected baboon biofluid sample preparation summary.

Sample	Day 2	Day 7	Day 10	Day 14	Day 18	Day 21
BAL	N_{bead} = 14400 $f_{RNA:Bead}$ = 23.1 $V_{biofluid}$: 250µL $f_{xloc:bead}$ = 20.8 $N_{trapped}$ = 5 N_{xloc} = 104	N/A	N/A	Not Detected	N/A	Not Detected
NPT	N_{bead} = 6000 $f_{RNA:Bead}$ = 100 $V_{biofluid}$: 8.75µL $f_{xloc:bead}$ = 134.6 $N_{trapped}$ = 10 N_{xloc} = 1346	N_{bead} = 12000 $f_{RNA:Bead}$ = 28 $V_{biofluid}$: 250µL $f_{xloc:bead}$ = 34.11 $N_{trapped}$ = 18 N_{xloc} = 614	N_{bead} = 3600 $f_{RNA:Bead}$ = 1.03 $V_{biofluid}$: 600µL $f_{xloc:bead}$ = 1 $N_{trapped}$ = 3 N_{xloc} = 3	N_{bead} = 1800 $f_{RNA:Bead}$ = ND $V_{biofluid}$: 600µL $f_{xloc:bead}$ = 22.63 $N_{trapped}$ = 8 N_{xloc} = 181	N_{bead} = 1800 $f_{RNA:Bead}$ = ND $V_{biofluid}$: 600µL $f_{xloc:bead}$ = 8.2 $N_{trapped}$ = 5 N_{xloc} = 41	N_{bead} = 1800 $f_{RNA:Bead}$ = 1.24 $V_{biofluid}$: 600µL $f_{xloc:bead}$ = 2.17 $N_{trapped}$ = 6 N_{xloc} = 13
REC	Not Detected	N_{bead} = 30000 $f_{RNA:Bead}$ = 27 $V_{biofluid}$: 250µL $f_{xloc:bead}$ = 27.17 $N_{trapped}$ = 6 N_{xloc} = 163	N_{bead} = 96000 $f_{RNA:Bead}$ = 112 $V_{biofluid}$: 250µL $f_{xloc:bead}$ = 71.67 $N_{trapped}$ = 9 N_{xloc} = 645	N_{bead} = 1800 $f_{RNA:Bead}$ = 0.43 $V_{biofluid}$: 250µL $f_{xloc:bead}$ = 0 $N_{trapped}$ = 2 N_{xloc} = 0	Not Detected	Not Detected

7.3 TACRE implementation for quantitative viral RNA analysis

To characterize the nanopore sensor for viral RNA quantification method, first a blank control experiment was performed. The nanopore integrated optofluidic device was filled with 1XT50 buffer solution only. When an electrical voltage is applied between nanopore and outlet reservoir, a steady baseline ionic current is established (fig. 7.5a). No particle translocation deterministic spike signals appeared when no target functionalized magnetic beads were optically trapped and heated under the nanopore. This confirms no false positive signal from the nanopore sensor without the presence of target RNA particles.

To observe the response of the nanopore sensor during a TACRE experiment, semen sample collected from the Zika infected Marmoset on the 9th day after the inoculation was tested. The viral RNA concentration in the biofluid was calculated as 4.72x10^{6}/mL from RT-qPCR analysis. The TACRE assay was designed so 62.5µL ($V_{biofluid}$) of the biofluid was processed and 472 targets ($f_{RNA:bead}$) were attached to each magnetic bead

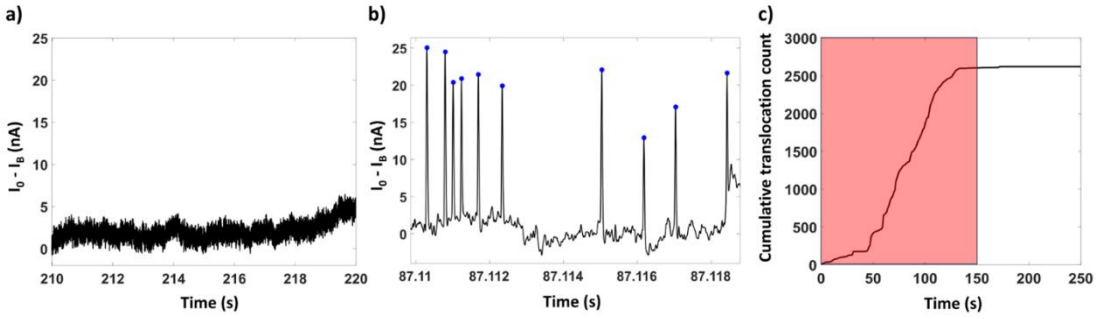

Fig. 7.5 a) Baseline subtracted nanopore ionic current signal for a blank control. b) Observed single viral RNA translocation (blue dots) during simultaneous heating and nanopore capture process. c) Cumulative translocation count shows dynamic nature of the TACRE assay (the red shaded region indicates 2.5 min heating window).

based on the qPCR result. During the optical trapping stage, 4 target functionalized beads ($N_{trapped}$) were trapped within the nanopore capture radius. The experiments were run with the highest voltage provided by the Digidata 1440A digitizer to maximize translocation rate and ionic current change, and characteristic translocation signals were observed when the simultaneous heat release and nanopore signal acquisition was started (fig. 7.5b). Though a nanopore with size smaller than 20nm would have further increased the relative current change $\Delta I/I$, our experimental conditions produced translocation signals with very high signal-to-noise ratio demonstrated in fig. 7.5b, indicating that nanopore size did not limit our analytical sensitivity. In total, 2,620 translocation signals (N_{xloc}) were observed, indicating the total number of released Zika viral RNAs from the trapped beads inside the nanopore capture volume (fig. 7.5c). The average number of calculated viral RNA per bead ($f_{xloc:bead}$) is 655, in comparison to the expected $f_{RNA:bead}$ of 472. The viral RNA concentration is calculated to be 6.28×10^6/mL according to eq. 7.3, which is close to the qCPR predicted viral RNA concentration.

7.4 Longitudinal viral load study with virus infected non-human primates

After characterizing the TACRE assay for successful zika viral RNA quantification from an infected marmoset semen sample, we considered implementing this assay in longitudinal viral load analysis studies. The top panel of fig. 7.6 shows the timeline of sample collection events (denoted by checkmarks) for the different fluids. Circles

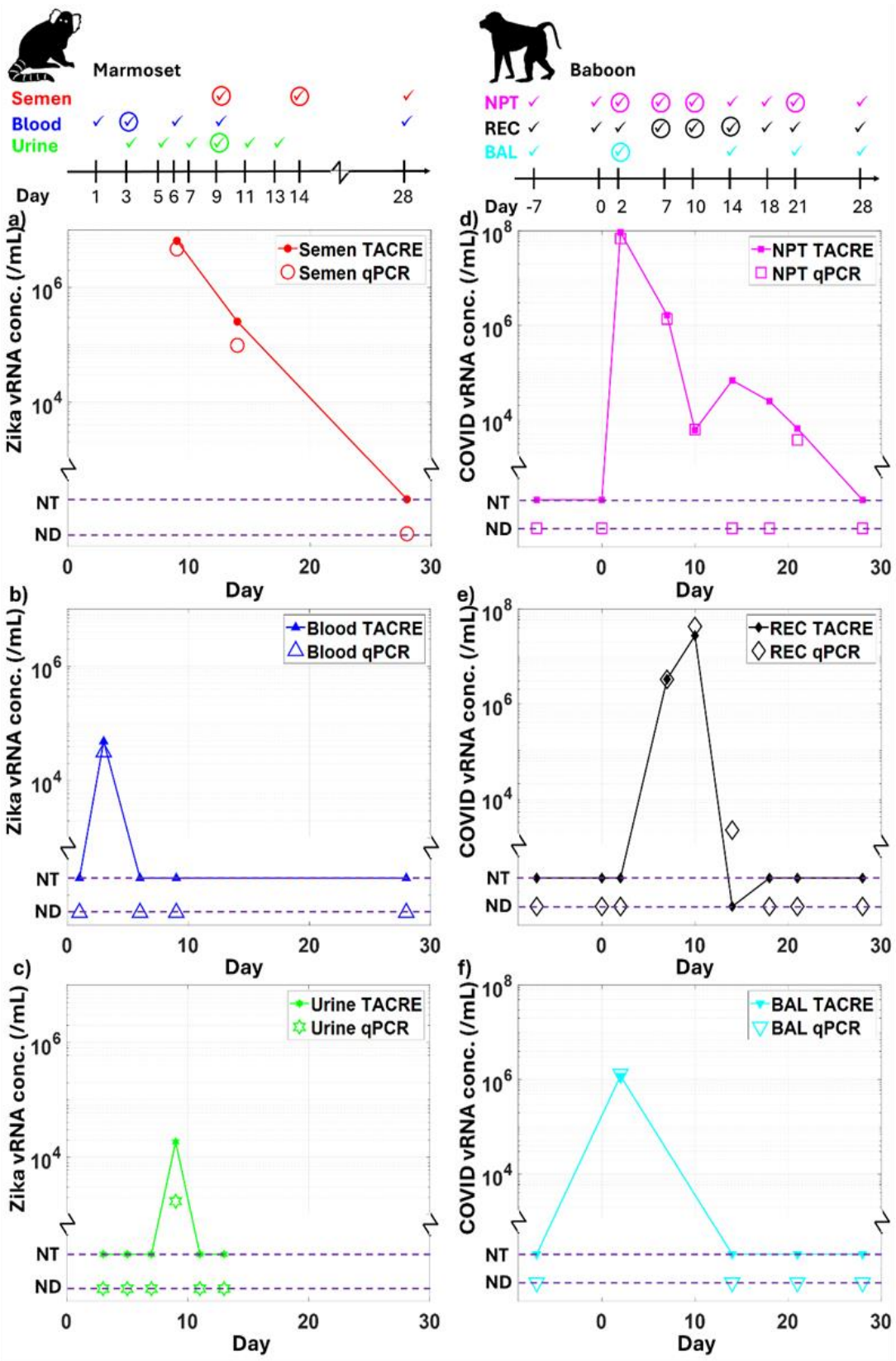
Marmoset
Semen
Blood
Urine
Day
1 3 5 6 7 9 11 13 14 28
Baboon
NPT
REC
BAL
Day -7 0 2 7 10 14 18 21 28
a)
Zika vRNA conc. (/mL)
Semen TACRE
Semen qPCR
NT
ND
Day
d)
COVID vRNA conc. (/mL)
NPT TACRE
NPT qPCR
b)
Blood TACRE
Blood qPCR
e)
REC TACRE
REC qPCR
c)
Urine TACRE
Urine qPCR
f)
BAL TACRE
BAL qPCR

Fig. 7.6 Longitudinal nanopore TACRE study of a-c) Zika infected marmoset and d-f) SARS-CoV-2 infected baboon biofluids. The top panel shows the sample collection frequency along the longitudinal study. A checkmark indicates a day on which a sample was collected and tested with qPCR. A checkmark inside a circle indicates that the qPCR assay provided a result for the collected sample. (Solid marker: for TACRE calculated value, open marker: qPCR obtained value). The dashed lines indicate that no viral load was detected (ND, PCR) or samples were not tested (NT, TACRE).

around the checkmark denote a positive RT-qPCR result, indicating that most PCR measurements were unsuccessful, likely due to very low viral loads or the complexity of the PCR process.

A four weeklong longitudinal study was designed with Zika virus infected Marmoset as a non-human primate model. Three different biofluids, i.e., semen, urine, whole blood, were collected and analyzed from the animal at pre-determined intervals. Our experimental analysis displayed (Fig. 7.6a-c) successful viral RNA identification and quantification from all three samples using the TACRE method covering the entire dynamic range throughout the infection period. Statistical analysis of these translocation signals shows commonly observed data clustering, indicating analysis of similar particles and a distinguishable SNR (fig. 7.7a-c). Specifically, semen emerged as the most suitable sample type, showing the highest viral loads and largest observable period, in agreement with previous studies [193]. While urine and blood samples produced only limited viral load values for both assay types, we were able to conclude from the nanopore assay that the viral load peaks earlier in the infection, and that urine can be used as a more readily available sample fluid if semen is too difficult or impossible to obtain. When compared with the corresponding RT-qPCR analysis, we got good agreement between the two methods even though the TACRE based viral

quantification method is simple and direct (calibration-free, amplification-free, and label-free). Also, the PCR method has numerous steps (reverse transcription, amplification, standard curve calibration) that can lead to target loss and errors, resulting in a smaller concentration reading.

Another five weeklong longitudinal study was performed with a SARS-CoV-2 infected baboon and three types of biofluids i.e., nasopharyngeal and throat swab (NPT), rectal swab, bronchoalveolar lavage (BAL) were collected and analyzed. Similar to the Zika virus analysis, the TACRE assay successfully detected and quantified viral RNAs from all types of biofluids (fig. 7.6d-f) and statistical analysis shows similar clustering (fig. 7.7d-f). This longitudinal study shows prolonged viral RNA shedding in NPT sample (fig. 7.6d) and a temporally delayed response in the rectal swab samples (fig. 7.6e) indicating both respiratory, and gastrointestinal (GI) infection caused by SARS-CoV-2 virus as predicted in recent literatures[194]. The viral load in the BAL samples followed the same course as in NPT samples as observed both with PCR and the nanopore sensor (Fig. 7.6f).

Though a consistent triplicate measurement could not be performed due to the small amounts of sample volume, the validity of our measurements was ensured by the good agreement with the PCR reference values across all samples and days. This label- and amplification-free analysis method produced results for all PCR-positive samples with the exception of a single SARS-CoV-2 sample (day 14, rectal swab), in which case the PCR concentration was very low and very little sample volume was available for the nanopore measurement. Again, the timeline on top of Figs. 7.6d-f shows that less than

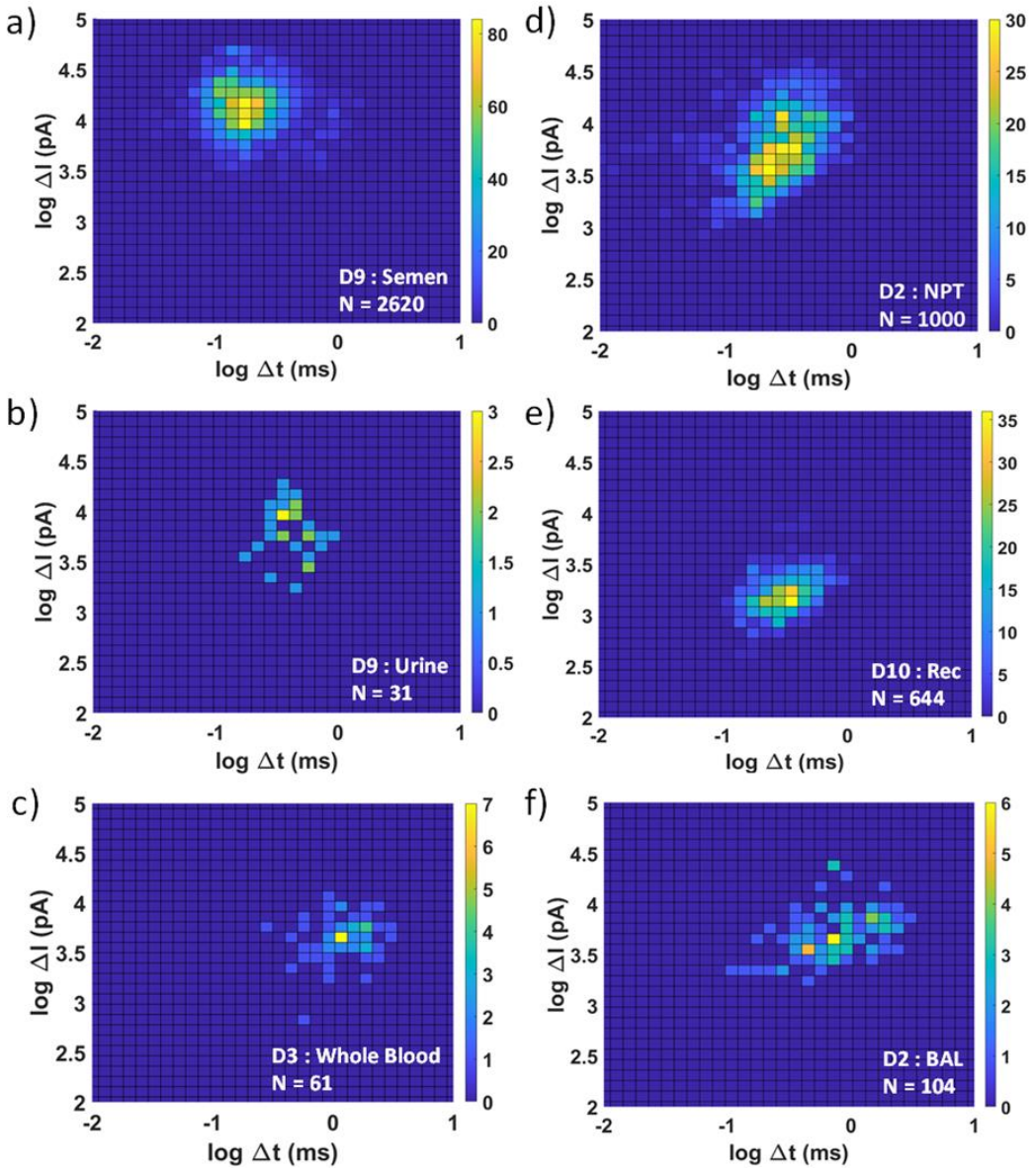

Fig. 7.7 Statistical analysis of translocation signals for TACRE experiments with six different biofluids.

50% of the collected samples produced a positive PCR result. So, we ran two of the samples for which PCR did not produce a result and that represented a gap in the longitudinal study (SARS-CoV-2, NPT, days 14 and 18). As shown in fig. 7.6d, a quantitative viral load value for both samples were obtained consistently following the

dynamic trend that this biofluid exhibited over time. It should be noted that, the TACRE assay does not have a fundamentally lower limit of detection than PCR, and thus the samples at the beginning and end of the infection were not tested by TACRE assay when the viral loads are extremely low. It can be concluded that the nanopore based TACRE approach performs at least as well as RT-qPCR, but with significantly reduced experimental complexity. The next section will discuss the underlying reason of this amplification-free TACRE assay to be able to obtain comparable results to the qRT-PCR method.

7.4.1 Target local concentration enhancement

The TACRE method utilizes the optical trapping assisted target local-concentration enhancement inside the nanopore capture volume (V_{cap}). The target local concentration obtained by TACRE can be calculated by eq. 7.4 similar to the method explained in section 6.2.4. Here, the bulk concentration is assumed to be equal to the target concentration (CRNA) calculated by the TACRE assay.

$$Enhancement\ factor = \frac{N_{xloc}}{V_{cap}\ x\ C_{RNA}} \tag{7.4}$$

The values of the concentration enhancement factor for all of our tested samples are listed in Tables 7.3 and 7.4. The enhancement factor ranges from $8.3x10^3$ to $1.22x10^6$. This large increase is critical for implementing this high throughput nanopore detection scheme with clinically relevant concentrations.

Table 7.4 Local target concentration enhancement factor for TACRE experiments with Zika infected marmoset samples.

Sample	Day 3	Day 9	Day 14
Blood	5.72×10^5	N/A	N/A
Urine	N/A	7.66×10^5	N/A
Semen	N/A	3.053×10^5	9.54×10^4

Table 7.3 Local target concentration enhancement factor for TACRE experiments with SARS-CoV-2 infected baboon samples.

Sample	Day 2	Day 7	Day 10	Day 14	Day 18	Day 21
BAL	3.96×10^4	N/A	N/A	N/A	N/A	N/A
NPT	8.295×10^3	1.7×10^5	2.29×10^5	1.22×10^6	7.62×10^5	9.145×10^5
REC	N/A	1.35×10^4	1.07×10^4	N/A	N/A	N/A

In summary, incorporation of this powerful optofluidic-nanopore platform in a longitudinal viral load monitoring study comprising two lethal viral infection i.e., Zika and SARS-CoV-2 and six different types of biofluid showed the versatility of the TACRE assay, paving a new way towards solid-state nanopore based molecular diagnosis from clinical samples without the need of nucleic acid sequencing and amplification.

Chapter 8 Nanopore integrated optofluidic platform development for label-free exosome and exosomal cargo analysis

In recent years, the development of organoid cultures has emerged as a groundbreaking laboratory technique for modeling complex biological processes in vitro [23], [24], [195]. Among these, brain organoid cultures have drawn significant attention for their ability to replicate the intricate cellular organization and functional characteristics of the developing human brain, providing valuable insights into neurological development during infancy and fetal stages [196]–[198]. As researchers dive deeper into the complexity of organoid cultures, attention has turned to the role of small extracellular vesicles (EV) secreted by cells as potential biomarkers [199], [200]. Exosomes, a type of extracellular vesicle (EV), typically range in size from 30 to 150 nm and closely resemble their parent cells in characteristics. Their role in facilitating cell-to-cell signaling by transporting diverse proteins and genetic materials within their cargo has captured the attention of researchers, leading to the exploration of novel scientific avenues [201], [202]. Furthermore, the presence of exosomes in the conditioned media of organoid cultures offer a non-invasive window into these complex systems and can be used as next generation liquid biopsy biomarker [203], [204]. Specifically, the presence of the Enolase 1 (ENO1) gene within exosomal RNA has captivated our attention, given its critical roles in cellular metabolism, notably in glycolysis, tumor cell division, proliferation, apoptosis, and metastasis [205]–[207]. Understanding the dynamics of organoid-secreted whole exosome and organization of exosomal cargo,

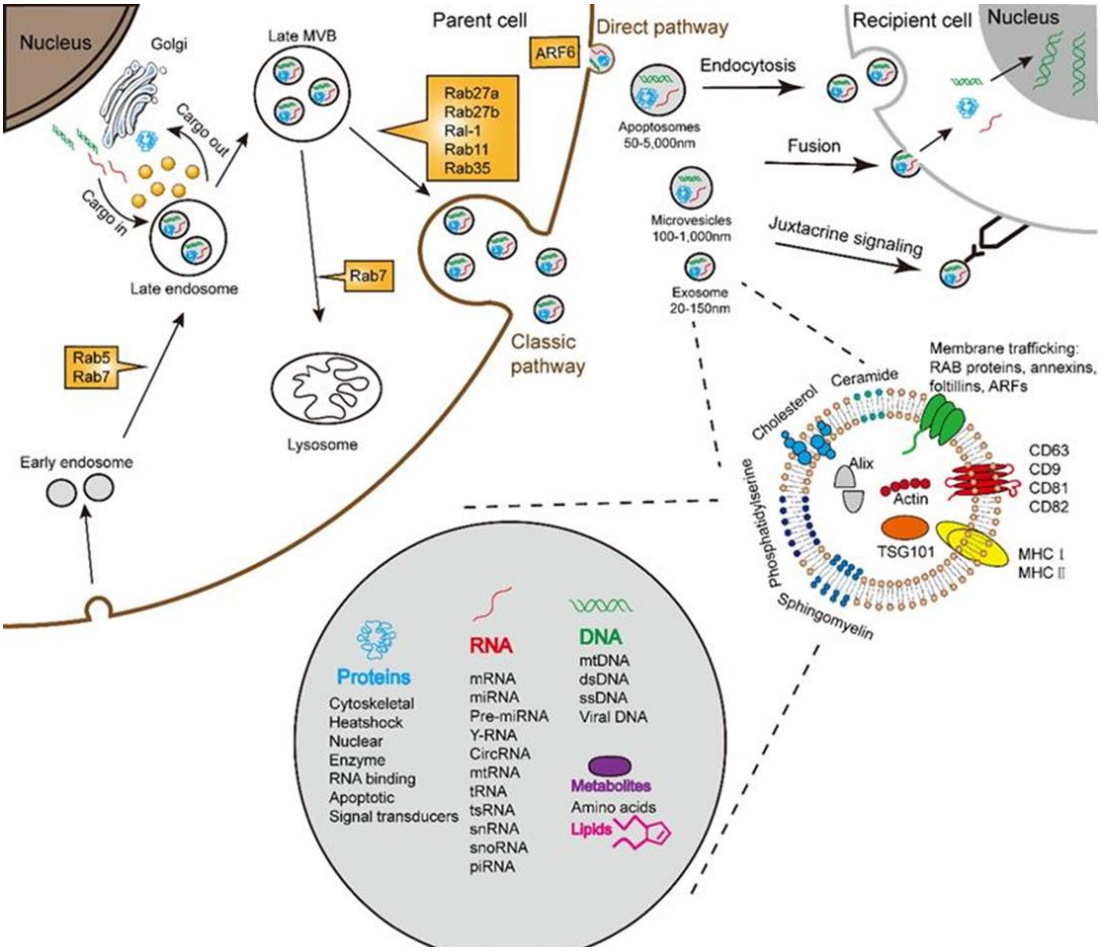

Fig. 8.1 Schematic illustration of exosome biogenesis and its composition. Adapted from [212].

including the Enolase 1 gene holds promise for unraveling the metabolic activity of the organoid in the culture and its dependency on the physiological concentration of the nutrient and waste inside the condition media. This chapter will first discuss label-free direct electrical detection of exosomes in solid-state nanopore sensors. Then, another application of optical trap assisted nanopore capture rate enhancement (TACRE) technique will be demonstrated for high-throughput quantification of ENO-1 gene from organoid secreted exosomes available in the cerebral organoid culture conditioned media.

8.1 Exosomes: definition, isolation and detection methods

Extracellular vesicles (EVs) are secreted by nearly all cells and are classified into three types based on origin, function, and biogenesis: exosomes, microvesicles (MVs)/shedding particles, and apoptotic bodies [208], [209]. Exosomes, typically ranging from 30-150 nm in size, are formed inside endosomes and released into the extracellular environment (see fig. 8.1). Exosome biogenesis and uptake by cell is an active area of research leading to the understanding in sorting and packaging of cargos in exosomes and their role in therapeutics and drug delivery [199]. Exosomes and other EVs can be found in biofluids such as saliva, urine, blood, and cerebrospinal fluid (CSF) [210], [211]. Exosomes possess membrane structures comprising a lipid bilayer and contain various molecular constituents, including proteins (enzymes, signal transducers etc.) , DNAs, RNAs (non-coding RNA, miRNA, mRNA etc.), lipids, and metabolites [212]. They also possess a negative surface charge in biofluid or when suspended in a water-based buffer solution. For example, the zeta potential of exosome particles is calculated to be -7.825mV, -8.54mV, and -30mV inside human serum, saliva and 1x phosphate buffer saline (PBS) solution, respectively [213], [214]. As researchers increasingly recognize the clinical significance of exosomes, worldwide efforts are underway to develop diverse custom micro- and nano-systems beyond conventional bulk machines for the isolation, processing, and detection of extracellular vesicles (EVs), including exosomes. The conventional method for isolating EVs and MVs relies on size and density, such as ultracentrifugation, which is time-consuming and demands expensive laboratory equipment and trained personnel [215]. Recently

developed microfluidic platforms for extracellular vesicle (EV) isolation have revolutionized the process by scaling it down to a single chip [216]. Innovative techniques like Deterministic Lateral Displacement (DLD), which utilizes micro and nano pillars, and acoustic nano filters employing interdigitated transducer (IDT) electrodes, leverage the advantages of micro/nano fabrication and microfluidic methodologies [217], [218]. Also, lipid-based nanoprobes, Immunoaffinity-based isolation assays have been developed to obtain high specificity, and to isolate specific subpopulations of EVs based on the expression of a specific surface marker [219]–[221]. For quantification of the isolated EVs in aqueous media, the most popular method is nanoparticle tracking analysis (NTA) [222], [223]. This method relies on a confocal light microscopy system, and any commercial NTA platform has software that counts and tracks individual particle trajectory to calculate the hydrodynamic diameter of the particle based on a modified Stokes-Einstein equation as well as the concentration and zeta potential of the particle in the sample [224]. New applications such as sub-population and colocalization are being offered by utilizing both light scattering- and fluorescence-based analysis on the same instrument. Though NTA instruments are now being extensively used for analyzing microvesicles and EVs with a size limit of detection of 30-50nm, the required sample concentration (10^5 particle/mL) and volume (minimum of 1mL) for a reliable measurement is still high. Other conventional EV detection methods include flow cytometry, dynamic light scattering (DLS) and cryogenic transmission electron microscopy (cryo-TEM) [225]. All these methods have their own limitations, and they are not convenient for

integrating with a broader microfluidic network for developing a high-throughput sample to result scheme.

Solid-state nanopore sensors have shown great promise in the single molecule analysis field and can be a perfect candidate for developing integrated platform for detecting, counting, and sorting single EVs [226], [227]. The nanopore based detection technique relies on transient ionic current change while a particle goes thorough the pore encoding the size, and charge of the translocating particle. Also, it is possible to tune the size of the nanopore to target different size ranges. Compared to conventional EV detection methods, nanopore based method is cheaper, and can offer higher resolution and lower limit of detection [228]–[230].

We have developed an integrated nanopore-optofluidic platform by integrating optical planar waveguides and solid-state nanopores with microfluidic channels on the same chip. Previously, this platform demonstrated excellent correlated electrical and optical detection of fluorescently tagged nanobead and whole virus (H_1N_1: 80-120nm) with ~150nm nanopore [20]. As exosomes have similar size range (30-150nm), a similar nanopore-optofluidic platform was utilized for electrical detection of cerebral organoid derived exosome samples. Details of the sample preparation and nanopore detection result will be described in the next section.

8.2 Direct exosome detection in nanopore-optofluidic platform

8.2.1 Exosome sample preparation

The exosome sample was collected and processed in the Haussler-Salama laboratory at UCSC. I thank Spencer T. Seiler for his help in the exosome sample preparation process. The sample processing protocol was adopted from [231] and involved ultracentrifugation for isolating exosomes from cell debris, apoptotic bodies and larger vesicles. First, 9mL of condition media collected from an organoid culture well was diluted with 29mL of 1xPBS buffer solution and then filtered through 200nm filter unit (Corning). The flowthrough volume was transferred to a centrifugation tube and extra volume of 1xPBS was added to make final weight of the tube as 38 grams. The tube was spun at 10,000 rpm for 10 min at 4°C (Parameter: r_MAX = 17,100 g, r_AVG = 12,300 g, r_MIN = 7,480 g) to pellet larger vesicles. The supernatant was transferred to a new tube and then spun at 30,000 rpm for 90min at 4°C (parameter: r_MAX = 154,000 g, r_AVG = 111,000 g, r_MIN = 67,300 g) to pellet smaller vesicles. The supernatant was discarded, and the pellet was resuspended in 500µL of 0.1x Sasai-2 condition media. Sasai-2 is a nutrition media prepared by slightly diluting the commercially available DMEM/F-12, GlutaMAX™ supplement (Thermo Fisher Scientific). The The sample was aliquoted (20µL) and stored at -80°C freezer. A single aliquot was thawed and immediately tested with the nanopore platform.

8.2.2 Nanopore detection result and analysis

Fig. 8.2a shows the nanopore integrated optofluidic platform for direct label-free detection of exosome particles. The platform consists of a microfluidic channel with a nanopore drilled on its top wall. Detailed device fabrication and nanopore integration is provided in chapters 2 and 5. For this experiment, the nanopore was created using FIB milling to achieve a targeted diameter of 150 nm to cover the whole size range of exosome. Fig. 8.2b shows a SEM micrograph of such a FIB milled nanopore of size 145.7nm. Three metal reservoirs are added to the inlet, outlet, and on the nanopore to fill the channel, introduce particles and apply electric potential across the nanopore. As exosomes have negative surface charge, the electric potential is applied such that particles can translocate from the nanopore reservoir (cis) to the microfluidic channel (trans). This translocation orientation promises future applications such as nanopore based single exosome gating [112], correlated electro-optical analysis [20], and electrical trapping [232] inside the optofluidic channel.

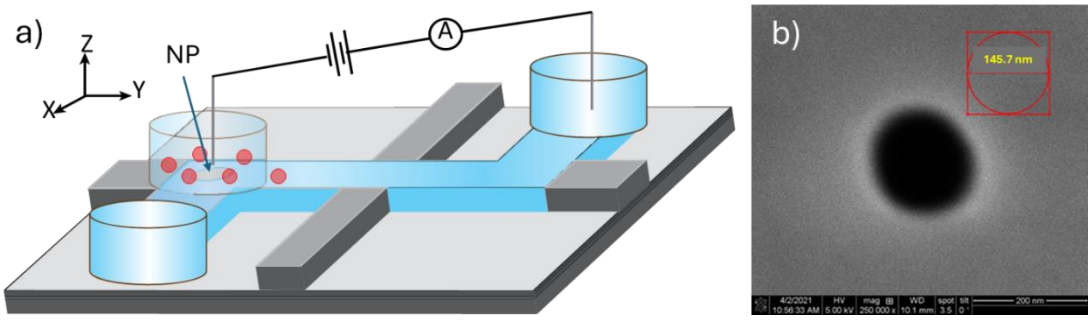

Fig. 8.2 a) Nanopore-optofluidic platform for direct electrical detection of cerebral organoid derived exosome. b) SEM micrograph of solid-state nanopore drilled on the microfluidic channel.

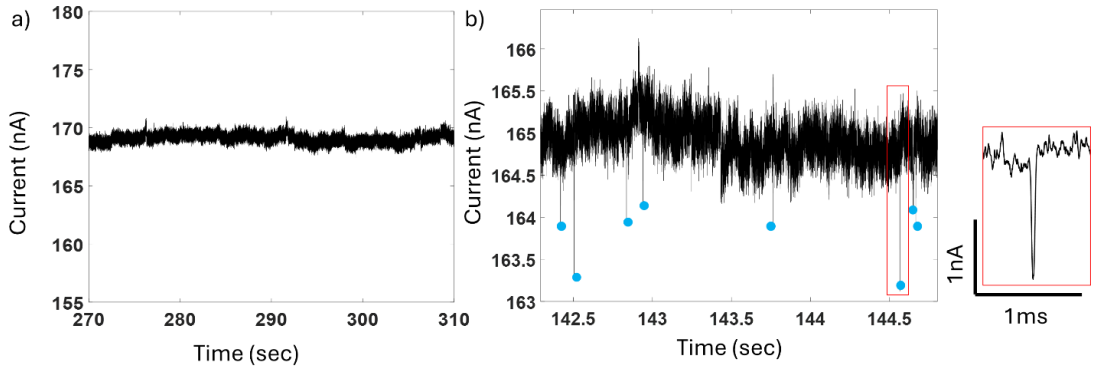

Fig. 8.3 a) Nanopore baseline current for 1xSasai-2 condition media (filtered with 20nm filter). b) Characteristic nanopore translocation signal for exosomes. Inset shows zoom-in view of a single blockade.

Fig 8.3a shows nanopore baseline current at a constant DC voltage when the device is filled with fresh 1x Sasai-2 condition media (filtered with 20nm track etched inorganic membrane filter). The same nanopore sensor starts to show characteristic blockade signals when the nanopore reservoir is filled with exosome solution (see fig. 8.3b). Each blockade corresponds to individual exosome particle translocation event (see fig. 8.3b inset) and further analysis of the blockade depth or differential current (ΔI) and dwell time (Δt) of these detected translocation signal can provide useful information regarding the detected exosome population. Fig. 8.4 a-c shows dwell time vs differential current scatter plot observed with three similar size (~150nm) nanopore devices. The current blockade (differential current/baseline current) analysis shown in fig. 8.4 d-f demonstrates good agreement among these trials indicating similar particle translocation through the nanopore. The summary of these trials is provided in table 8.1.

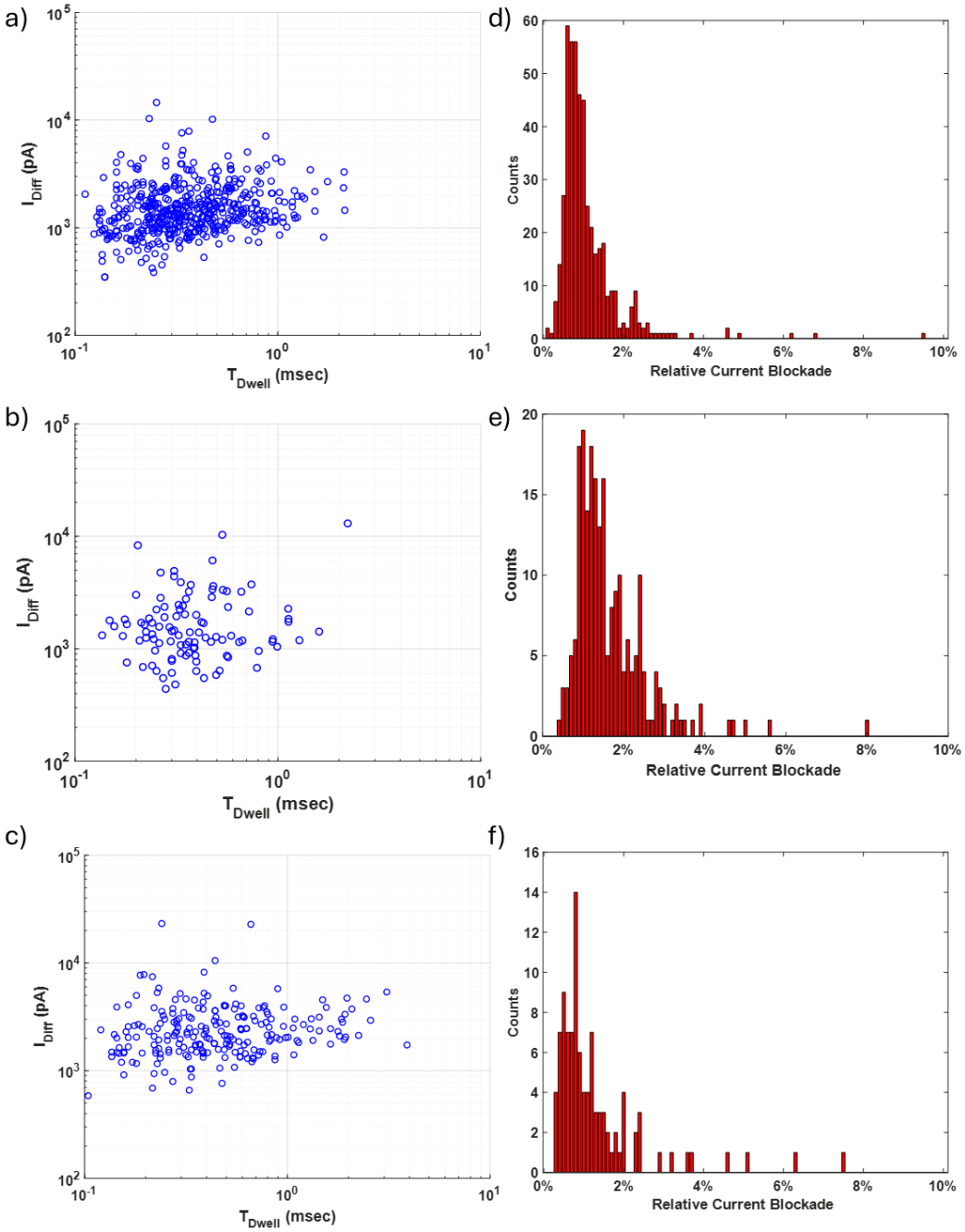

Fig. 8.4 Exosome translocation analysis with three similar size nanopore devices. a-c) Scatter plot of dwell time vs differential current. d-f) Relative current blockade histogram.

Table 8.1 Summary of nanopore based exosome detection experiments.

1	~142nm (F8@MA41)	0.43 ± 0.301	1.71 ± 1.27	1.05 ± 0.8
2	~150nm (D7@MA41)	0.445 ± 0.314	1.98 ± 1.873	1.25 ± 1.19
3	~145nm (G7@MA41)	0.595 ± 0.545	2.74 ± 2.39	1.76 ± 1.84

8.3 Label-free and amplification-free quantification of Enolase-1 gene in conditioned media from organoid model

The organoid culture process aims to closely replicate the growth of specific cell types outside the human body within a controlled environment. To achieve this, various conditioned media solutions are utilized to supply nutrients and maintain physiological parameters within optimal ranges [233]. Despite the widespread use of commercially available media in organoid culture experiments, they often lack tailored optimization for specific cell types [234]. A notable challenge arises in cerebral organoids, where in vitro growth may lead to upregulated glycolysis as the cell prefers aerobic glycolysis under stressed environment [235], [236]. This affects glucose consumption and waste secretion rates, compromising organoid fidelity. Therefore, implementing a continuous feedback mechanism based on the physiological properties or metabolic biomarkers of the conditioned media becomes crucial to fine-tune media properties accordingly. Given the pivotal role of Enolase-1 (ENO-1) in glycolysis regulation, it emerges as a promising biomarker to monitor cellular metabolism. In the pursuit of non-invasive

liquid biopsy methods, monitoring the expression of the ENO-1 gene within exosomal cargo offers insights into cellular dynamics and metabolic activity. However, the low concentration of Enolase-1 gene in the condition media and the presence of other cell constituents make it hard for a standalone nanopore-based label-free detection mechanism to achieve specificity and low limit of detection. In that case, optical trapping-assisted nanopore capture rate enhancement (TACRE) can offer an elegant solution. The subsequent section will discuss the redesign of the TACRE assay for capturing and quantifying ENO-1 gene from condition media in label-free and amplification-free manner.

8.3.1 TACRE assay for rapid ENO-1 gene detection

TACRE assay uses magnetic bead based solid-phase extraction method which requires designing a biotinylated short pulldown (ssDNA) sequence that compliments a part of the target gene. A 17 base pair long pulldown sequence (/5BiotinTEG/AA CGA TGA GAC ACC ATG) was designed for the ENO-1 TACRE assay to complement a region of the exon 10 (Accession no - NM_001428.5: 1217-1233; Homo sapiens enolase 1 (ENO1), transcript variant 1, mRNA). The melting temperature of the designed pulldown sequence is calculated to be 49°C by IDT oligo analyzer tool (https://www.idtdna.com/calc/analyzer). As described in section 5.5, the streptavidin coated magnetic beads are first mixed with biotinylated pulldown sequence in such a way that all the available binding sites on the bead surface will be occupied by the pulldown sequences. Then the beads are washed to get rid of unattached pulldown

sequences. The resuspended bead-pulldown construct will be later used for quantitative ENO-1 gene detection assay.

To validate the nanopore TACRE assay for ENO-1 gene, 1781 bp long synthetic ssDNA strands with the same sequence as ENO-1 gene (accession no: NM_001428.5) was purchased from Twist Biosciences. The concentration of the purchased solution is 1 ng/uL or $5.2x10^{11}$ copies/mL (the weight of each strand of 1781bp long ssDNA = $1.922x10^{-18}$ gram).

The TACRE assay is calibration-free, and a detailed description of the target concentration determination is provided in section 7.2.4. Briefly, 16µL ($V_{biofluid}$) of $5.2x10^{9}$ copies/mL (C_{target}) 1781 bp long synthetic ENO-1 ssDNA target is heated at 95°C for 5 mins and then mixed with 20µL of $2x10^{7}$/mL magnetic bead pulldown constructs. The total number of beads inside the sample is 400,000 (N_{bead}). The samples were incubated in an ice bath for an hour and then magnetically washed to discard the supernatant. Ideally, each bead should have 208 targets ($f_{RNA:bead}$) immobilized on its surface. Finally, the washed beads were resuspended in 1x T50 buffer for experimental use.

8.3.2 TACRE based quantification of synthetic ENO-1 ssDNA target

The nanopore-optofluidic platform used for the ENO-1 TACRE assay was described in section 7.1. Fig. 8.5 shows a schematic view of the experimental platform where the target-carrying beads are added to the inlet reservoir and flown inside a microchannel. A subset of the beads ($N_{trapped}$) is optically trapped from the fluid flow in the protrusion region by a fiber-coupled 532nm wavelength laser light. A ~20 nm diameter nanopore is drilled on the optical trapping region by milling through the top 300nm thin membrane using a focused ion beam (FIB). The target nucleic acids immobilized on the trapped beads are simultaneously released by heating the chip to 50°C and rapidly captured by the electrophoretic force created by applying a DC voltage difference between the nanopore and outlet reservoir. Translocated particles generate characteristic ionic current changes and a MATLAB based analysis is utilized for

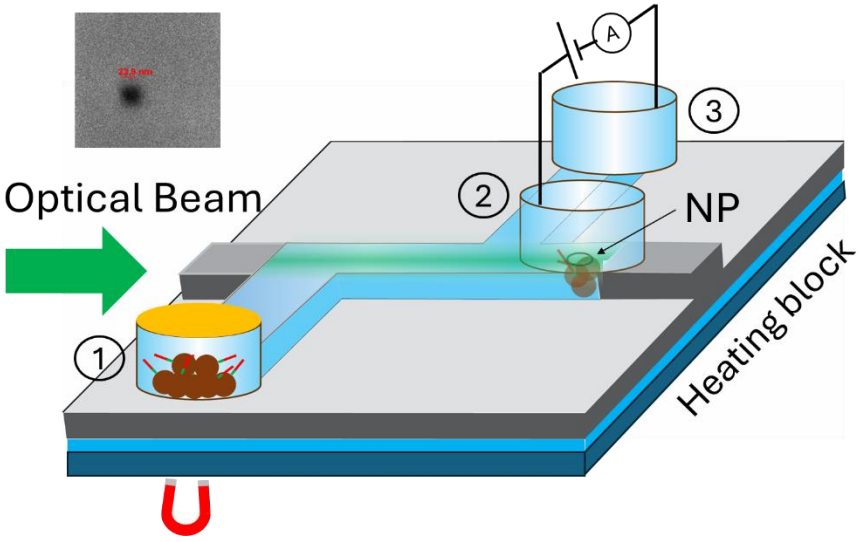

Fig. 8.5 TACRE platform for high-throughput ENO-1 gene detection. Inset shows a 23nm size nanopore drilled by FIB.

counting the total translocation events (N_{xloc}) throughout the experiment. Finally, the concentration of the target particles can be calculated using eq 8.1.

$$C_{TACRE} = \frac{\frac{N_{xloc}}{N_{trapped}} N_{bead}}{V_{biofluid}} \quad 8.1$$

The TACRE assay was first applied to quantify the ENO-1 ssDNA target suspended in 1xT50 buffer. Later, the target gene was spiked in lysis buffer (Qiagen RLT lysis buffer) to mimic the experimental environment where the condition media will be lysed to break open exosomal cargo. The experimental results show excellent agreement between the expected and calculated target concentration. The detailed experimental parameters and results are included in table 8.2. Fig 8.3 shows characteristic translocation signals and event detection dynamics for both experiments.

Table 8.2 Experimental parameters for TACRE based synthetic ENO-1 target concentration analysis.

Parameter	Value
C_{target} (#/mL)	5.2×10^9
$V_{biofluid}$ (µL)	16
N_{bead}	400000
$f_{RNA:bead}$	208
ENO-1 in 1XT50	
$N_{trapped}$	12
N_{xloc}	2542
C_{TACRE} (#/mL)	5.296×10^9
ENO-1 in lysis buffer	
$N_{trapped}$	20
N_{xloc}	4657
C_{TACRE} (#/mL)	5.82×10^9

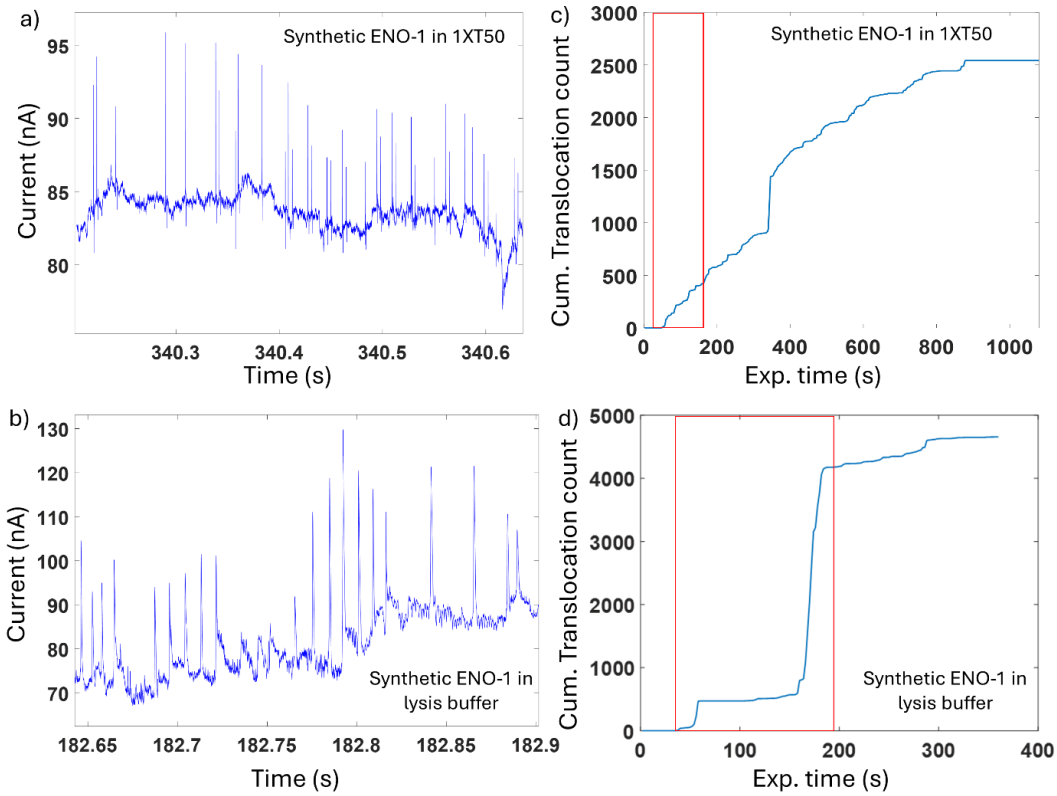

Fig. 8.6 Nanopore detection trace for TACRE ENO-1 assay in a) 1XT50 buffer, and in b) lysis buffer. Translocation event detection dynamics for experiments in c) 1XT50 and in d) lysis buffer. Red rectangle indicates the heating time window.

Finally, the TACRE assay was tested with actual exosome samples derived from an organoid culture system. The conditioned media was provided by the Braingeneers Lab at UCSC. 150 µL of condition media ($V_{biofluid}$) was collected from 78 days old cerebral organoid tissue and then filtered with a 200nm membrane filter to discard cell debris and macrovesicles with size larger than 200nm. Afterwards, the filtered sample was lysed with 450 µL of Trizol LS lysis agent to expose the exosomal cargo. The TACRE assay was performed by heating the sample at 75°C for 5 mins and then mixed with 6 µL of $2x10^6$/mL magnetic bead-pulldown construct (N_{bead} = 12,000) for hybridization. After 1 hour of ice bath incubation, the beads were washed and resuspended in 1XT50

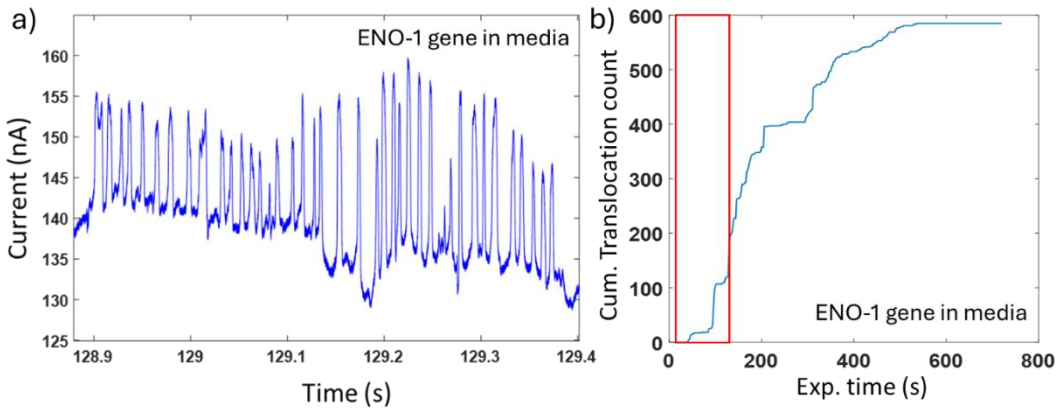

Fig. 8.7 a) Translocation detection trace for TACRE ENO-1 assay in lysed condition media derived from cerebral organoid culture. b)Translocation event detection dynamics for the same nanopore experiment. Red rectangle indicates the heating time window.

buffer for experimental use. During the experiment, 62 beads ($N_{trapped}$) were trapped, and 585 translocation events (N_{xloc}) were observed. The ENO-1 gene concentration in the conditioned media was calculated using eq 8.1 as $7.55x10^5$/mL. Fig 8.7 shows the translocation trace and event detection dynamics obtained from the experiment.

In summary, the TACRE assay with integrated nanopore-optofluidic platform showed great promise in exosome liquid biopsy applications. In the future, this simple yet high-throughput platform can be utilized for targeting multiple biomarker genes from the same condition media just by designing different pulldown sequences. If integrated with an organoid culture network, the nanopore-optofluidic platform can form a closed loop system and can provide valuable feedback by counting the genes of interest in the conditioned media.

Chapter 9 Conclusion and outlook

In conclusion, this thesis has explained innovative methodologies for integrating programmable electronics with optofluidic biomarker detection and a biofluid processing unit, enabling user-friendly, configurable, remotely accessible, and high-throughput single-chip analyses at the point of care. Moreover, the nanopore-integrated optofluidic platform has been reconfigured for rapid, amplification-free biomarker quantification from various clinical biofluids and organoid culture-derived condition media.

The first major advancement involved the introduction of an FPGA-integrated ARROW optofluidic platform for real-time signal processing and particle flow analysis. This platform was successfully tested with both fluorescent nanobeads and antibiotic-resistant plasmid DNA targets at clinically relevant concentrations, demonstrating a detection accuracy of 99% in real-time compared to MATLAB-based post-processing analysis. The concentration of the target particles was determined within seconds to a few minutes with excellent reliability and reproducibility covering clinically relevant range. Furthermore, statistical analysis was conducted to determine the optimum experimental time for reliable analysis, while showcasing the potential for a futuristic closed-loop system to efficiently deliver processed biofluid to the sensing region without wasting valuable reagents. Moving forward, hardware and software improvements could enhance the platform's capabilities, such as integrating y-splitters [237] or top-down excitation [238] for generating higher signal-to-noise ratio spot patterns, as well as implementing machine learning algorithms [16] for real-time

multiplexed biomarker detection. Additionally, the integration of an electrical feedback circuit for a smart particle delivery system based on real-time flow analysis results is feasible.

The second advancement involved the integration of a PDMS-based programmable microfluidic sample processing unit into an IoT framework, enabling remote access and controllability for automation. A graphical user interface was designed to facilitate the transfer of user-defined instructions from a remotely located computer to the experimental setup via Amazon Web Service in the form of MQTT messages. An internet-connected Raspberry Pi device received the message and controlled the pneumatically actuated fluidic valves of the microfluidic device according to user commands. This functional block demonstrated the feasibility of a massively parallel biofluid processing scheme targeting multiple biomarkers simultaneously, with potential applications in resource sharing and scientific education for underserved communities. Finally, a successful field testing of this platform as an easy project-based learning tool for teaching programming concepts to Latinx life science students was demonstrated.

The third advancement focused on developing a label-free and amplification-free quantitative assay for detection of viral RNAs in clinical samples on a nanopore-optofluidic chip. This assay, combined with precise non-invasive optical particle manipulation techniques, addressed the throughput limitations of standalone solid-state nanopore sensors. The first application of this scheme was demonstrated with rapid screening of SARS-CoV-2 RNAs from human nasal swab and from buffer solutions

covering the entire clinically relevant concentration with a dynamic range of 5 logs and limit of detection of 17 aM. The optical trapping of target carrying magnetic microbeads near the nanopore sensor increased the target concentration locally by a factor of ~10^5, enabling a detection rate enhancement of ~2000x at the limit of detection. The platform was further redesigned to improve the controllability and reliability of the optical trapping process. The next application of TACRE demonstrated label-free and amplification-free quantification of viral load progression for Zika and SARS-CoV-2 infections in marmoset and baboon animal models, respectively. The assay was applied to all relevant biofluids, including semen, urine, and whole blood for Zika and nasopharyngeal and throat swab, rectal swab, and bronchoalveolar lavage for SARS-CoV-2, proving its versatility. The assay demonstrated a limit of detection of 10 aM and showed excellent accuracy in comparison with corresponding RT-qPCR results. Future improvement could include a lightweight and portable biofluid separation disk [44] to extract total RNA. Moreover, an on-chip automatic sample preparation and delivery system [56], [61] can be integrated to the nanopore-optofluidic chip to minimize the required sample volume and to enable parallel operation. Furthermore, the approach can be extended to multiplexed analysis using various strategies, such as sequentially exposing the sample to a group of functionalized beads with different pulldown sequences and delivering the beads to one or more nanopores. The groups of beads can be delivered to multiple nanopores working in parallel or to a single nanopore for simultaneous detection by designing pulldown sequences for different melting temperatures and then detecting

the target molecules in order of increasing pulldown melting temperature. The assay can also be integrated with other on-chip microbead trapping techniques, such as nano channel based mechanical trapping for point-of-care application [239].

Finally, the nanopore-optofluidic platform was leveraged for size specific detection of exosomes from cerebral organoid culture media demonstrating promise in single exosome gating and analysis by integrating programmable electronics [112], [232] and optical waveguide [20]. Additionally, the TACRE method was utilized for calibration-free quantification of the Enolase-1 gene from lysed media, a relevant biomarker indicating cell metabolism. This high-throughput assay and platform can be further integrated in line with organoid culture network to provide useful feedback and can create a closed loop system.

Overall, this work lays the foundation for simple, programmable, high-throughput, and highly sensitive integrated optofluidic platforms that can serve as a new class of molecular diagnostic tools.

Appendix

A.1 Python code for graphical user interface (GUI)

The custom python program for designing the graphical user interface (GUI) is divided into several individually executable blocks. The program can be run in any cloud-based python notebook such as Google Colab, Jupyter Notebook.

```
#Block 1 - initialization
import time as t
import json
!pip install AWSIoTPythonSDK
import AWSIoTPythonSDK.MQTTLib as AWSIoTPyMQTT
from google.colab import drive
from google.colab import files
import io
drive.mount('/content/gdrive')

#Block 2 – certificate
# Define ENDPOINT, CLIENT_ID, PATH_TO_CERTIFICATE,
PATH_TO_PRIVATE_KEY, PATH_TO_AMAZON_ROOT_CA_1, MESSAGE,
TOPIC, and RANGE
ENDPOINT = "apshwcds0150b-ats.iot.us-west-
2.amazonaws.com"
CLIENT_ID = "testDevice"
PATH_TO_CERTIFICATE = "/content/gdrive/My
Drive/certificates/34604caebf5afe3e013edde47d6a36f85e31
946065c99c3ea72c1f889d418c7f-certificate.pem.crt"
PATH_TO_PRIVATE_KEY = "/content/gdrive/My
Drive/certificates/34604caebf5afe3e013edde47d6a36f85e31
946065c99c3ea72c1f889d418c7f-private.pem.key"
PATH_TO_AMAZON_ROOT_CA_1 = "/content/gdrive/My
Drive/certificates/AmazonRootCA1.pem"
TOPIC = "test/testing"
myAWSIoTMQTTClient =
AWSIoTPyMQTT.AWSIoTMQTTClient(CLIENT_ID)
```

```
myAWSIoTMQTTClient.configureEndpoint(ENDPOINT, 8883)
myAWSIoTMQTTClient.configureCredentials(PATH_TO_AMAZON_
ROOT_CA_1, PATH_TO_PRIVATE_KEY, PATH_TO_CERTIFICATE)
switch = True
myAWSIoTMQTTClient.connect()
#Block 3 - upload "script" remotely
uploaded = files.upload()
for fname in uploaded.keys():
  data_path = fname
test_file = open(data_path)
test_file_content = test_file.readlines()
test_file.close()
print(test_file_content)
#Block 4 - variable and user control switch setup
result = 0
result_struct = {}
Mode_Manual_Control = False #@param {type:"boolean"}
Mode_Run_Saved_Scripts = False #@param {type:"boolean"}
Mode_Load_Remote_Scripts = False #@param
{type:"boolean"}
Mode_EXIT = True #@param {type:"boolean"}
CH_1 = False #@param {type:"boolean"}
CH_2 = False #@param {type:"boolean"}
CH_3 = False #@param {type:"boolean"}
CH_2 = False #@param {type:"boolean"}
CH_3 = False #@param {type:"boolean"}
CH_4 = False #@param {type:"boolean"}
CH_5 = False #@param {type:"boolean"}
CH_6 = False #@param {type:"boolean"}
CH_7 = False #@param {type:"boolean"}
```

```
CH_8 = False #@param {type:"boolean"}
CH_9 = False #@param {type:"boolean"}
CH_10 = False #@param {type:"boolean"}
CH_11 = False #@param {type:"boolean"}
CH_12 = False #@param {type:"boolean"}
CH_13 = False #@param {type:"boolean"}
CH_14 = False #@param {type:"boolean"}
CH_15 = False #@param {type:"boolean"}
CH_16 = False #@param {type:"boolean"}
Manual_List = [CH_1, CH_2, CH_3, CH_4, CH_5, CH_6,
CH_7, CH_8, CH_9, CH_10, CH_11, CH_12, CH_13, CH_14,
CH_15, CH_16]
print(Manual_List)
Script_1 = False #@param {type:"boolean"}
Script_2 = False #@param {type:"boolean"}
Script_3 = False #@param {type:"boolean"}
Script_4 = False #@param {type:"boolean"}
Script_5 = False #@param {type:"boolean"}
'''make sure only select one!'''
'''Modes:
1=manual,
2=saved scripts (in Raspberry Pi),
3=remote scripts (from drive)'''
if (Mode_Manual_Control):
 result = 0
 for ch in Manual_List:
     result = (result<<1) + int(ch)
 result_struct['mode'] = 1;
 result_struct['param'] = result;
elif (Mode_Run_Saved_Scripts): #Optimize this later
```

```
 if Script_1:
     result_struct['mode'] = 2
     result_struct['param'] = 1
 elif Script_2:
     result = (2<<4)+2
     result_struct['mode'] = 2
     result_struct['param'] = 2
 elif Script_3:
     result = (3<<4)+2
     result_struct['mode'] = 2
     result_struct['param'] = 3
 elif Script_4:
     result = (4<<4)+2
     result_struct['mode']= 2
     result_struct['param'] = 4
 elif Script_5:
     result = (5<<2)+2
     result_struct['mode'] = 2
     result_struct['param'] = 5
elif (Mode_Load_Remote_Scripts):
    result_struct['mode'] = 3
    result_struct['param'] = test_file_content
elif (Mode_EXIT):
    result_struct['mode'] = 0
    result_struct['param'] = 0
print("{0:b}".format(result))
```

```
#Block 5 - publish the message
print('Begin Publish')
message = result_struct
myAWSIoTMQTTClient.publish(TOPIC, json.dumps(message),
1)
print("Published: '" + json.dumps(message) + "' to the
topic: " + "'test/testing'")
t.sleep(0.1)
```

A.2 Python code for decoding MQTT message running on Raspberry Pi

- **Main program: Subscriber.py**

```
import time
import os
import logging
import json
import datetime
import RPi.GPIO as GPIO
from time import sleep
from AWSIoTPythonSDK.MQTTLib import AWSIoTMQTTClient
#our files starting here
from RunScript import run_script
from RunScript import run_main

GPIO.setmode(GPIO.BOARD)
GPIO.setwarnings(False)
# valves 1-4
GPIO.setup(11, GPIO.OUT)
GPIO.output(11, GPIO.LOW)
GPIO.setup(13, GPIO.OUT)
GPIO.output(13, GPIO.LOW)
GPIO.setup(15, GPIO.OUT)
GPIO.output(15, GPIO.LOW)
GPIO.setup(16, GPIO.OUT)
GPIO.output(16, GPIO.LOW)
```

```
# valves 5-8
GPIO.setup(18, GPIO.OUT)
GPIO.output(18, GPIO.LOW)
GPIO.setup(12, GPIO.OUT)
GPIO.output(12, GPIO.LOW)
GPIO.setup(22, GPIO.OUT)
GPIO.output(22, GPIO.LOW)
GPIO.setup(29, GPIO.OUT)
GPIO.output(29, GPIO.LOW)
#valves 9-12
GPIO.setup(31, GPIO.OUT)
GPIO.output(31, GPIO.LOW)
GPIO.setup(33, GPIO.OUT)
GPIO.output(33, GPIO.LOW)
GPIO.setup(35, GPIO.OUT)
GPIO.output(35, GPIO.LOW)
GPIO.setup(37, GPIO.OUT)
GPIO.output(37, GPIO.LOW)
#valves 13-16
GPIO.setup(32, GPIO.OUT)
GPIO.output(32, GPIO.LOW)
GPIO.setup(36, GPIO.OUT)
GPIO.output(36, GPIO.LOW)
GPIO.setup(38, GPIO.OUT)
GPIO.output(38, GPIO.LOW)
GPIO.setup(40, GPIO.OUT)
GPIO.output(40, GPIO.LOW)
MANUAL=1
SAVED_SCRIPTS=2
REMOTE_SCRIPTS=3
EXIT = 0
```

```
#script name dict
script_names = {
 1:"Dummy",
 2:"Dummy2",
 3:"TestAll"
}
delay_period = 0.01
switch = True
# 3/2 - added all pins (16)
channel_num = 16
# the list indices (0~15) are according to the valve
indices (1~16)
channel_pin =
[11,13,15,16,18,12,22,29,40,38,36,32,37,35,33,31]
ENDPOINT = "apshwcds0150b-ats.iot.us-west-
2.amazonaws.com"
CLIENT_ID = "RemoteDevice"
PATH_TO_CERTIFICATE = "certificates/cloud.pem.crt"
PATH_TO_PRIVATE_KEY = "certificates/cloud.pem.key"
PATH_TO_AMAZON_ROOT_CA_1 = "certificates/root-ca.pem"
# When the mode is MANUAL, this function will be
called. It changes status of
#    the pins according to the manual commands
def manual_control(param):
        i = 0;
        for channels in range(channel_num):
                if ((param>>(15-i))&1) >0:
                        GPIO.output(channel_pin[i],
GPIO.HIGH)
                else:
                        GPIO.output(channel_pin[i],
GPIO.LOW)
                i+=1
# When the mode is SAVED_SCRIPTS, this function will be
called.
#    It runs one of the saved scripts
```

```
def saved_scripts(param):
     print("running script "+ script_names[param])
     run_script("saved_scripts/" + script_names[param])
def remote_scripts(param):
     print("Running remote script")
     run_main(param)
        current_time = datetime.datetime.now()
     filename ="history/"+ str(current_time)+".txt"
#This is where we name the history file
     history = open(filename, "w")
     for lines in param:
          history.write(lines)
     print("script saved in " + filename)
#When the mode is EXIT, this function exits the
subscriber loop
def exit_subscriber():
     print("Ending subscriber")
     os._exit(0)
def read_msg_struct(self, params, packet):
     message = packet.payload;
     message = json.loads(message)
     print("Message: ", message)
     mode = message['mode']
     param = message['param']
     if (mode == MANUAL):
          manual_control(param)
     elif (mode == SAVED_SCRIPTS):
          saved_scripts(param)
     elif (mode == REMOTE_SCRIPTS):
          remote_scripts(param)
     elif (mode == EXIT):
          exit_subscriber()
     logging.warning('topic '+ packet.topic)
     logging.warning('topic '+packet.topic)
     logging.warning('Watch out!')
```

```
myMQTTClient = AWSIoTMQTTClient(CLIENT_ID)
myMQTTClient.configureEndpoint(ENDPOINT, 8883)
myMQTTClient.configureCredentials(PATH_TO_AMAZON_ROOT_C
A_1, PATH_TO_PRIVATE_KEY, PATH_TO_CERTIFICATE)
myMQTTClient.configureOfflinePublishQueueing(-1) #
Infinite offline Publish queueing
myMQTTClient.configureDrainingFrequency(2) # Draining:
2 Hz
myMQTTClient.configureConnectDisconnectTimeout(10) # 10
sec
myMQTTClient.configureMQTTOperationTimeout(5) # 5 sec
myMQTTClient.connect()
myMQTTClient.subscribe("test/testing", 1,
read_msg_struct)
while (True):
     print("in while")
     time.sleep(5)
device.end();
GPIO.cleanup()
```

- **Subprogram: RunScript.py**

```
import time
import os
import logging
from AWSIoTPythonSDK.MQTTLib import AWSIoTMQTTClient
GPIO.setmode(GPIO.BOARD)
GPIO.setwarnings(False)
import RPi.GPIO as GPIO
from time import sleep
```

```
#run commands
def action(command):
 command_type = command[0]
 command_param = command[1:-1]
 if command_type == 'o':
  print("open " + command_param)
  GPIO.output(channel_pin[int(command_param)-1],
GPIO.HIGH)
 elif command_type == 'c':
  print("close " + command_param)
  GPIO.output(channel_pin[int(command_param)-1],
GPIO.LOW)
 elif command_type == 'w':
  print("wait " + command_param)
  time.sleep(float(int(command_param))/1000)
 else:
  print("invalid command type")

#(recursively) read and run functions
#in future if there is performance issue, this code can
be optimized by locating
#  the function bodies first so we don't have to find
start and end points every
#  time.
def run_function(items):
 #print(items) #show func params(debug purpose)
 iteration = 1 #by default it runs once.
 if len(items) > 2:
  iteration = int(items[2])
 #find where the function starts and ends
  for i, func_line in enumerate(file_lines):
   if func_line[0:-1] == items[1]: #items[1] = function
name
    start_line = i
   for i, func_line in
enumerate(file_lines[start_line:]):
```

```
     if func_line[0:3] == "end":
          end_line = i + start_line
          break
      break
#function start executing here
 funclines = file_lines[start_line+1:end_line] #does
not include the function name
  #function iteration:
 for i in range(iteration):
  print("instance " + str(i+1) + " of function " +
items[1])
  for command in funclines:
   #if it calls a function
   if command[0:4] == "call":
    run_function(command.split())
   #else it must be a command
   else:
    action(command)
#run main til end
def run_main(content):
 for i, lines in enumerate(content):
  if lines == "main\n":
   start = i
 global file_lines
 file_lines = content
 print("starting main")
 for main_line in file_lines[start+1:]:
  if main_line == "end\n": #end of the main
   print("end of main")
   break;
 elif main_line[0:4] == "call": # go to function
     items = main_line.split()
```

```
      run_function(items)
      pass
   else:
    action(main_line)
#start here
def run_script(script_name):
 print("Start executing" + script_name)
 filename = script_name
 file = open(filename)
 file_content = file.readlines()
 file.close()
 run_main(file_content)
```

Bibliography

[1] D. G. Moriel, D. Piccioli, M. M. Raso, and M. Pizza, “The overlooked bacterial pandemic,” *Semin. Immunopathol.*, no. 0123456789, Dec. 2023, doi: 10.1007/s00281-023-00997-1.

[2] P. Bhadoria, G. Gupta, and A. Agarwal, “Viral pandemics in the past two decades: An overview,” *J. Fam. Med. Prim. Care*, vol. 10, no. 8, p. 2745, 2021, doi: 10.4103/jfmpc.jfmpc_2071_20.

[3] R. Sanjuán and P. Domingo-Calap, “Mechanisms of viral mutation,” *Cell. Mol. Life Sci.*, vol. 73, no. 23, pp. 4433–4448, Dec. 2016, doi: 10.1007/s00018-016-2299-6.

[4] K. K. Kumarasamy *et al.*, “Emergence of a new antibiotic resistance mechanism in India, Pakistan, and the UK: A molecular, biological, and epidemiological study,” *Lancet Infect. Dis.*, vol. 10, no. 9, pp. 597–602, 2010, doi: 10.1016/S1473-3099(10)70143-2.

[5] A. Qureshi and J. H. Niazi, “Biosensors for detecting viral and bacterial infections using host biomarkers: A review,” *Analyst*, vol. 145, no. 24. pp. 7825–7848, 2020, doi: 10.1039/d0an00896f.

[6] I. M. Mackay, K. E. Arden, and A. Nitsche, “Real-time PCR in virology,” *Nucleic Acids Res.*, vol. 30, no. 6, pp. 1292–1305, 2002, doi: 10.1093/nar/30.6.1292.

[7] A. Borst, A. T. A. Box, and A. C. Fluit, “False-positive results and contamination in nucleic acid amplification assays: Suggestions for a prevent and destroy strategy,” *Eur. J. Clin. Microbiol. Infect. Dis.*, vol. 23, no. 4, pp. 289–299, 2004, doi: 10.1007/s10096-004-1100-1.

[8] H. Schmidt and A. R. Hawkins, “The photonic integration of non-solid media using optofluidics,” *Nat. Photonics*, vol. 5, no. 10, pp. 598–604, Aug. 2011, doi: 10.1038/nphoton.2011.163.

[9] X. Fan and I. M. White, “Optofluidic microsystems for chemical and biological analysis,” *Nat. Photonics*, vol. 5, no. 10, pp. 591–597, Sep. 2011, doi: 10.1038/nphoton.2011.206.

[10] C. Monat, P. Domachuk, and B. J. Eggleton, “Integrated optofluidics: A new river of light,” *Nature Photonics*, vol. 1, no. 2. pp. 106–114, Feb. 2007, doi: 10.1038/nphoton.2006.96.

[11] A. Stambaugh, J. W. Parks, M. A. Stott, G. G. Meena, A. R. Hawkins, and H. Schmidt, “Optofluidic multiplex detection of single SARS-CoV-2 and influenza A antigens using a novel bright fluorescent probe assay,” *Proc. Natl. Acad. Sci. U. S. A.*, vol. 118, no. 20, pp. 2–7, 2021, doi: 10.1073/pnas.2103480118.

[12] D. Yin, H. Schmidt, J. P. Barber, and A. R. Hawkins, “Integrated ARROW waveguides with hollow cores,” *Opt. Express*, vol. 12, no. 12, p. 2710, Jun. 2004, doi: 10.1364/opex.12.002710.

[13] D. Ozcelik *et al.*, “Optofluidic wavelength division multiplexing for single-virus detection.,” *Proc. Natl. Acad. Sci. U. S. A.*, vol. 112, no. 42, pp. 12933–12937, Oct. 2015, doi: 10.1073/pnas.1511921112.

[14] K. D. Leake, B. S. Phillips, T. D. Yuzvinsky, A. R. Hawkins, and H. Schmidt, “Optical particle sorting on an optofluidic chip,” *Opt. Express*, vol. 21, no. 26, p. 32605, Dec. 2013, doi: 10.1364/OE.21.032605.

[15] S. Kühn, E. J. Lunt, B. S. Phillips, A. R. Hawkins, and H. Schmidt, “Optofluidic particle concentration by a long-range dual-beam trap,” *Opt. Lett.*, vol. 34, no. 15, p. 2306, 2009, doi: 10.1364/ol.34.002306.

[16] V. Ganjalizadeh, A. R. Hawkins, and H. Schmidt, “Adaptive time modulation technique for multiplexed on-chip particle detection across scales,” *Optica*, vol. 10, no. 7, p. 812, 2023, doi: 10.1364/optica.489068.

[17] M. J. N. Sampad, M. N. Amin, A. R. Hawkins, and H. Schmidt, “FPGA Integrated Optofluidic Biosensor for Real-Time Single Biomarker Analysis,” *IEEE Photonics J.*, vol. 14, no. 1, pp. 1–6, 2022, doi: 10.1109/JPHOT.2021.3127484.

[18] V. Ganjalizadeh, G. G. Meena, T. A. Wall, M. A. Stott, A. R. Hawkins, and H. Schmidt, “Fast custom wavelet analysis technique for single molecule detection and identification,” *Nat. Commun.*, vol. 13, no. 1, p. 1035, Feb. 2022, doi: 10.1038/s41467-022-28703-z.

[19] H. Cai *et al.*, “Optofluidic analysis system for amplification-free, direct detection of Ebola infection,” *Sci. Rep.*, vol. 5, no. 1, p. 14494, Nov. 2015, doi: 10.1038/srep14494.

[20] S. Liu, Y. Zhao, J. W. Parks, D. W. Deamer, A. R. Hawkins, and H. Schmidt, “Correlated electrical and optical analysis of single nanoparticles and biomolecules on a nanopore-gated optofluidic chip,” *Nano Lett.*, vol. 14, no. 8, pp. 4816–4820, 2014, doi: 10.1021/nl502400x.

[21] D. K. Singh *et al.*, “Animal Models of COVID-19: Nonhuman Primates,” *Methods Mol. Biol.*, vol. 2452, pp. 227–258, 2022, doi: 10.1007/978-1-0716-2111-0_15/COVER.

[22] C. Y. Chiu *et al.*, “Experimental Zika Virus Inoculation in a New World Monkey Model Reproduces Key Features of the Human Infection,” *Sci. Rep.*, vol. 7, no. 1, p. 17126, Dec. 2017, doi: 10.1038/s41598-017-17067-w.

[23] M. Hofer and M. P. Lutolf, “Engineering organoids,” *Nature Reviews Materials*, vol. 6, no. 5. pp. 402–420, 2021, doi: 10.1038/s41578-021-00279-y.

[24] Z. Zhao *et al.*, “Organoids,” *Nat. Rev. Methods Prim.*, vol. 2, no. 94, Dec. 2022, doi: 10.1038/s43586-022-00174-y.

[25] A. K. Singh, S. Mittal, M. Das, A. Saharia, and M. Tiwari, “Optical biosensors: a decade in review,” *Alexandria Engineering Journal*, vol. 67. pp. 673–691, 2023, doi: 10.1016/j.aej.2022.12.040.

[26] C. Chen and J. Wang, “Optical biosensors: An exhaustive and comprehensive review,” *Analyst*, vol. 145, no. 5. pp. 1605–1628, 2020, doi: 10.1039/c9an01998g.

[27] E. Betzig and J. K. Trautman, “Near-Field Optics: Microscopy, Spectroscopy, and Surface Modification Beyond the Diffraction Limit,” *Science (80-.).*, vol. 257, no. 5067, 1992, doi: 10.1126/science.257.5067.189.

[28] W. E. Moerner and D. P. Fromm, “Methods of single-molecule fluorescence spectroscopy and microscopy,” *Rev. Sci. Instrum.*, vol. 74, no. 8, p. 3597, Jul. 2003, doi: 10.1063/1.1589587.

[29] D. R. Walt, “Optical methods for single molecule detection and analysis,” *Anal. Chem.*, vol. 85, no. 3, pp. 1258–1263, Feb. 2013, doi: 10.1021/AC3027178/ASSET/IMAGES/LARGE/AC-2012-027178_0003.JPEG.

[30] S. Weiss, “Fluorescence spectroscopy of single biomolecules,” *Science (80-.).*, vol. 283, no. 5408, pp. 1676–1683, 1999, doi: 10.1126/science.283.5408.1676.

[31] G. M. Whitesides, “The origins and the future of microfluidics,” *Nature*, vol. 442, no. 7101. pp. 368–373, Jul. 2006, doi: 10.1038/nature05058.

[32] Y. K. Cho, J. G. Lee, J. M. Park, B. S. Lee, Y. Lee, and C. Ko, “One-step pathogen specific DNA extraction from whole blood on a centrifugal microfluidic device,” *Lab Chip*, vol. 7, no. 5, pp. 565–573, 2007, doi:

10.1039/b616115d.

[33] A. Manz, N. Graber, and H. M. Widmer, “Miniaturized total chemical analysis systems: A novel concept for chemical sensing,” *Sensors Actuators B. Chem.*, vol. 1, no. 1–6, pp. 244–248, 1990, doi: 10.1016/0925-4005(90)80209-I.

[34] P. S. Dittrich and A. Manz, “Lab-on-a-chip: microfluidics in drug discovery,” *Nat. Rev. Drug Discov.*, vol. 5, no. 3, pp. 210–218, Mar. 2006, doi: 10.1038/nrd1985.

[35] D. Figeys and D. Pinto, “Lab-on-a-chip: A revolution in biological and medical sciences,” *Analytical Chemistry*, vol. 72, no. 9. pp. 330 A–335 A, 2000, doi: 10.1021/ac002800y.

[36] D. Psaltis, S. R. Quake, and C. Yang, “Developing optofluidic technology through the fusion of microfluidics and optics,” *Nature*, vol. 442, no. 7101. Nature Publishing Group, pp. 381–386, Jul. 2006, doi: 10.1038/nature05060.

[37] X. Fan and I. M. White, “Optofluidic microsystems for chemical and biological analysis,” *Nature Photonics*, vol. 5, no. 10. pp. 591–597, Oct. 2011, doi: 10.1038/nphoton.2011.206.

[38] J. W. Parks *et al.*, “Hybrid optofluidic integration,” *Lab Chip*, vol. 13, no. 20, p. 4118, Sep. 2013, doi: 10.1039/c3lc50818h.

[39] D. Brennan, J. Justice, B. Corbett, T. McCarthy, and P. Galvin, “Emerging optofluidic technologies for point-of-care genetic analysis systems: A review,”

Analytical and Bioanalytical Chemistry, vol. 395, no. 3. pp. 621–636, 2009, doi: 10.1007/s00216-009-2826-5.

[40] S. O. Kasap, "Optoelectronics and Photonics: Principles and Practices," *Prentice Hall, 1st edition*. 2001.

[41] L. B. Soldano and E. C. M. Pennings, "Optical Multi-Mode Interference Devices Based on Self-Imaging: Principles and Applications," *J. Light. Technol.*, vol. 13, no. 4, pp. 615–627, 1995, doi: 10.1109/50.372474.

[42] H. Schmidt and A. R. Hawkins, "Optofluidic waveguides: I. Concepts and implementations," *Microfluid. Nanofluidics*, vol. 4, no. 1–2, pp. 3–16, Jan. 2008, doi: 10.1007/s10404-007-0199-7.

[43] J. W. Parks, "Hybrid Optofluidic Biosensors," UC Santa Cruz, 2016.

[44] G. G. Meena *et al.*, "3× Multiplexed Detection of Antibiotic Resistant Plasmids With Single Molecule Sensitivity," *Lab Chip*, vol. 20, no. 20, pp. 3763–3771, 2020, doi: 10.1039/d0lc00640h.

[45] G. G. Meena *et al.*, "7X multiplexed, optofluidic detection of nucleic acids for antibiotic-resistance bacterial screening," *Opt. Express*, vol. 28, no. 22, p. 33019, 2020, doi: 10.1364/oe.402311.

[46] G. G. Meena, A. M. Stambaugh, V. Ganjalizadeh, M. A. Stott, A. R. Hawkins, and H. Schmidt, "Ultrasensitive detection of SARS-CoV-2 RNA and antigen using single-molecule optofluidic chip," *APL Photonics*, vol. 6, no. 6, pp. 1–7,

2021, doi: 10.1063/5.0049735.

[47] K. K. W. To *et al.*, “Temporal profiles of viral load in posterior oropharyngeal saliva samples and serum antibody responses during infection by SARS-CoV-2: an observational cohort study,” *Lancet Infect. Dis.*, vol. 20, no. 5, pp. 565–574, 2020, doi: 10.1016/S1473-3099(20)30196-1.

[48] D. C. Duffy, J. C. McDonald, O. J. A. Schueller, and G. M. Whitesides, “Rapid prototyping of microfluidic systems in poly(dimethylsiloxane),” *Anal. Chem.*, vol. 70, no. 23, pp. 4974–4984, 1998, doi: 10.1021/ac980656z.

[49] J. R. Anderson *et al.*, “Fabrication of topologically complex three-dimensional microfluidic systems in PDMS by rapid prototyping,” *Anal. Chem.*, vol. 72, no. 14, pp. 3158–3164, 2000, doi: 10.1021/ac9912294.

[50] J. Kim, M. Kang, E. C. Jensen, and R. A. Mathies, “Lifting gate polydimethylsiloxane microvalves and pumps for microfluidic control,” *Anal. Chem.*, vol. 84, no. 4, pp. 2067–2071, 2012, doi: 10.1021/ac202934x.

[51] W. H. Grover, A. M. Skelley, C. N. Liu, E. T. Lagally, and R. A. Mathies, “Monolithic membrane valves and diaphragm pumps for practical large-scale integration into glass microfluidic devices,” *Sensors Actuators, B Chem.*, vol. 89, no. 3, pp. 315–323, 2003, doi: 10.1016/S0925-4005(02)00468-9.

[52] M. A. Unger, H. P. Chou, T. Thorsen, A. Scherer, and S. R. Quake, “Monolithic microfabricated valves and pumps by multilayer soft lithography,” *Science (80-*

.)., vol. 288, no. 5463, pp. 113–116, 2000, doi: 10.1126/science.288.5463.113.

[53] K. W. Oh and C. H. Ahn, “A review of microvalves,” *J. Micromechanics Microengineering*, vol. 16, no. 5, pp. R13–R39, 2006, doi: 10.1088/0960-1317/16/5/R01.

[54] J. W. Parks and H. Schmidt, “Flexible optofluidic waveguide platform with multi-dimensional reconfigurability,” *Sci. Rep.*, vol. 6, 2016, doi: 10.1038/srep33008.

[55] Z. Cai, W. Qiu, G. Shao, and W. Wang, “A new fabrication method for all-PDMS waveguides,” *Sensors Actuators, A Phys.*, vol. 204, pp. 44–47, 2013, doi: 10.1016/j.sna.2013.09.019.

[56] G. G. Meena *et al.*, “Integration of sample preparation and analysis into an optofluidic chip for multi-target disease detection,” *Lab Chip*, vol. 18, no. 23, pp. 3678–3686, 2018, doi: 10.1039/c8lc00966j.

[57] T. Sano, J. Black, S. Mitchell, H. Zhang, and H. Schmidt, “Pneumatically tunable optofluidic DFB dye laser using corrugated sidewalls,” *Opt. Lett.*, vol. 45, no. 21, p. 5978, 2020, doi: 10.1364/ol.404303.

[58] T. Sano, H. Zhang, R. Losakul, and H. Schmidt, “All-in-One Optofluidic Chip for Molecular Biosensing Assays,” *Biosensors*, vol. 12, no. 7, p. 501, Jul. 2022, doi: 10.3390/bios12070501.

[59] A. Tong *et al.*, “Research priorities for COVID-19 sensor technology,” *Nat.*

Biotechnol., vol. 39, no. 2, pp. 144–147, 2021, doi: 10.1038/s41587-021-00816-8.

[60] B. Udugama *et al.*, "Diagnosing COVID-19: The Disease and Tools for Detection," *ACS Nano*, vol. 14, no. 4, pp. 3822–3835, 2020, doi: 10.1021/acsnano.0c02624.

[61] K. Du *et al.*, "Multiplexed efficient on-chip sample preparation and sensitive amplification-free detection of Ebola virus," *Biosens. Bioelectron.*, vol. 91, no. January, pp. 489–496, 2017, doi: 10.1016/j.bios.2016.12.071.

[62] A. Stambaugh, J. W. Parks, M. A. Stott, G. G. Meena, A. R. Hawkins, and H. Schmidt, "Optofluidic multiplex detection of single SARS-CoV-2 and influenza A antigens using a novel bright fluorescent probe assay," *Proc. Natl. Acad. Sci. U. S. A.*, vol. 118, no. 20, p. e2103480118, 2021, doi: 10.1073/pnas.2103480118.

[63] P. A. Simpson, *FPGA Design, Best Practices for Team Based Reuse*, 2nd Ed. Springer International Publishing, 2015.

[64] E. S. Hamilton, V. Ganjalizadeh, J. G. Wright, H. Schmidt, and A. R. Hawkins, "3D Hydrodynamic Focusing in Microscale Optofluidic Channels Formed with a Single Sacrificial Layer," *Micromachines*, vol. 11, no. 4, p. 349, Mar. 2020, doi: 10.3390/mi11040349.

[65] G. G. Meena, J. G. Wright, A. R. Hawkins, and H. Schmidt, "Greatly Enhanced Single Particle Fluorescence Detection Using High Refractive Index Liquid-

Core Waveguides," *IEEE J. Sel. Top. Quantum Electron.*, vol. 27, no. 5, pp. 1–7, 2021, doi: 10.1109/JSTQE.2021.3055078.

[66] A. Whitmore, A. Agarwal, and L. Da Xu, "The Internet of Things—A survey of topics and trends," *Inf. Syst. Front.*, vol. 17, no. 2, pp. 261–274, 2015, doi: 10.1007/s10796-014-9489-2.

[67] J. Gubbi, R. Buyya, S. Marusic, and M. Palaniswami, "Internet of Things (IoT): A vision, architectural elements, and future directions," *Futur. Gener. Comput. Syst.*, vol. 29, no. 7, pp. 1645–1660, 2013, doi: 10.1016/j.future.2013.01.010.

[68] M. C. Domingo, "An overview of the Internet of Things for people with disabilities," *Journal of Network and Computer Applications*, vol. 35, no. 2. pp. 584–596, 2012, doi: 10.1016/j.jnca.2011.10.015.

[69] A. F. Hussein, N. Arun Kumar, M. Burbano-Fernandez, G. Ramirez-Gonzalez, E. Abdulhay, and V. H. C. De Albuquerque, "An automated remote cloud-based heart rate variability monitoring system," *IEEE Access*, vol. 6, pp. 77055–77064, 2018, doi: 10.1109/ACCESS.2018.2831209.

[70] F. Firouzi, B. Farahani, M. Ibrahim, and K. Chakrabarty, "Keynote paper: From EDA to IoT eHealth: Promises, challenges, and solutions," *IEEE Trans. Comput. Des. Integr. Circuits Syst.*, vol. 37, no. 12, pp. 2965–2978, 2018, doi: 10.1109/TCAD.2018.2801227.

[71] P. K. Yong and E. T. W. Ho, "Streaming brain and physiological signal

acquisition system for IoT neuroscience application," in *IECBES 2016 - IEEE-EMBS Conference on Biomedical Engineering and Sciences*, 2016, pp. 752–757, doi: 10.1109/IECBES.2016.7843551.

[72] Z. Yang, Q. Zhou, L. Lei, K. Zheng, and W. Xiang, "An IoT-cloud Based Wearable ECG Monitoring System for Smart Healthcare," *J. Med. Syst.*, vol. 40, p. 286, 2016, doi: 10.1007/s10916-016-0644-9.

[73] A. A. P. Wai, H. Dajiang, and N. S. Huat, "IoT-enabled multimodal sensing headwear system," in *IEEE World Forum on Internet of Things, WF-IoT 2018 - Proceedings*, 2018, vol. 2018-Janua, pp. 286–290, doi: 10.1109/WF-IoT.2018.8355103.

[74] A. K. Dhawale, R. Poddar, S. B. E. Wolff, V. A. Normand, E. Kopelowitz, and B. P. Ölveczky, "Automated long-Term recording and analysis of neural activity in behaving animals," *Elife*, vol. 6, p. e27702, 2017, doi: 10.7554/eLife.27702.

[75] K. Hasham, K. Munir, and R. McClatchey, "Cloud infrastructure provenance collection and management to reproduce scientific workflows execution," *Futur. Gener. Comput. Syst.*, vol. 86, pp. 799–820, 2018, doi: 10.1016/j.future.2017.07.015.

[76] B. R. Schudel, C. J. Choi, B. T. Cunningham, and P. J. A. Kenis, "Microfluidic chip for combinatorial mixing and screening of assays," *Lab Chip*, vol. 9, no. 12, pp. 1676–1680, 2009, doi: 10.1039/b901999e.

[77] J. Kim, E. C. Jensen, M. Megens, B. Boser, and R. A. Mathies, “Integrated microfluidic bioprocessor for solid phase capture immunoassays,” *Lab Chip*, vol. 11, no. 18, pp. 3106–3112, 2011, doi: 10.1039/c1lc20407f.

[78] E. C. Jensen, B. P. Bhat, and R. A. Mathies, “A digital microfluidic platform for the automation of quantitative biomolecular assays,” *Lab Chip*, vol. 10, no. 6, pp. 685–691, 2010, doi: 10.1039/b920124f.

[79] K. Du *et al.*, “Microfluidic System for Detection of Viral RNA in Blood Using a Barcode Fluorescence Reporter and a Photocleavable Capture Probe Graphical abstract HHS Public Access,” *Anal Chem*, vol. 89, no. 22, pp. 12433–12440, 2017, doi: 10.1021/acs.anal-chem.7b03527.

[80] J. Kim, E. C. Jensen, A. M. Stockton, and R. A. Mathies, “Universal microfluidic automaton for autonomous sample processing: Application to the mars organic analyzer,” *Anal. Chem.*, vol. 85, no. 16, pp. 7682–7688, 2013, doi: 10.1021/ac303767m.

[81] E. C. Jensen, A. M. Stockton, T. N. Chiesl, J. Kim, A. Bera, and R. A. Mathies, “Digitally programmable microfluidic automaton for multiscale combinatorial mixing and sample processing,” *Lab Chip*, vol. 13, no. 2, pp. 288–296, 2013, doi: 10.1039/c2lc40861a.

[82] M. Ibrahim, M. Gorlatova, and K. Chakrabarty, “The internet of microfluidic things: Perspectives on system architecture and design challenges: Invited

paper," in *IEEE/ACM International Conference on Computer-Aided Design, Digest of Technical Papers, ICCAD*, 2019, vol. 2019-Novem, doi: 10.1109/ICCAD45719.2019.8942080.

[83] J. J. Wietsma, J. T. Van Der Veen, W. Buesink, A. Van Den Berg, and M. Odijk, "Lab-on-a-Chip: Frontier Science in the Classroom," *J. Chem. Educ.*, vol. 95, no. 2, pp. 267–275, 2018, doi: 10.1021/acs.jchemed.7b00506.

[84] Z. Hossain *et al.*, "Interactive and scalable biology cloud experimentation for scientific inquiry and education," *Nat. Biotechnol.*, vol. 34, no. 12, pp. 1293–1298, 2016, doi: 10.1038/nbt.3747.

[85] Y. Fintschenko, "Education: A modular approach to microfluidics in the teaching laboratory," *Lab Chip*, vol. 11, no. 20, pp. 3394–3400, 2011, doi: 10.1039/c1lc90069b.

[86] H. Bridle, J. Morton, P. Cameron, M. P. Y. Desmulliez, and M. Kersaudy-Kerhoas, "Design of problem-based learning activities in the field of microfluidics for 12- to 13-year-old participants—Small Plumbing!: empowering the next generation of microfluidic engineers," *Microfluid. Nanofluidics*, vol. 20, no. 7, p. 103, 2016, doi: 10.1007/s10404-016-1770-x.

[87] T. Sano *et al.*, "Open-loop lab-on-a-chip technology enables remote computer science training in Latinx life sciences students," *bioRxiv*, p. 2023.04.28.538776, Jan. 2023, doi: 10.1101/2023.04.28.538776.

[88] “Raspberry Pi website.” https://www.raspberrypi.com/.

[89] T. H. Team, “Introducing the MQTT Protocol – MQTT Essentials: Part 1,” 2015. https://www.hivemq.com/blog/mqtt-essentials-part-1-introducing-mqtt/.

[90] “MQTT website.” https://mqtt.org/.

[91] “AWS IoT Core website.” https://aws.amazon.com/iot-core/.

[92] S. Rufener, D. Mäusezahl, H. J. Mosler, and R. Weingartner, “Quality of drinking-water at source and point-of consumption-Drinking cup as a high potential recontamination risk: A field study in Bolivia,” *J. Heal. Popul. Nutr.*, vol. 28, no. 1, pp. 34–41, 2010, doi: 10.3329/jhpn.v28i1.4521.

[93] P. J. Kolbeck *et al.*, “Molecular structure, DNA binding mode, photophysical properties and recommendations for use of SYBR Gold,” *Nucleic Acids Res.*, vol. 49, no. 9, pp. 5143–5158, 2021, doi: 10.1093/nar/gkab265.

[94] W. E. Moerner and D. P. Fromm, “Methods of single-molecule fluorescence spectroscopy and microscopy,” *Rev. Sci. Instrum.*, vol. 74, no. 8, pp. 3597–3619, Aug. 2003, doi: 10.1063/1.1589587.

[95] R. J. Nichols and S. J. Higgins, “Single-Molecule Electronics: Chemical and Analytical Perspectives,” *Annu. Rev. Anal. Chem.*, vol. 8, no. 1, pp. 389–417, Jul. 2015, doi: 10.1146/annurev-anchem-071114-040118.

[96] C. Gu, C. Jia, and X. Guo, “Single-Molecule Electrical Detection with Real-

Time Label-Free Capability and Ultrasensitivity," *Small Methods*, vol. 1, no. 5, p. 1700071, May 2017, doi: 10.1002/smtd.201700071.

[97] P. R. Selvin and T. Ha, *Single-molecule Techniques: A Laboratory Manual*. 2008.

[98] M. Rahman *et al.*, "A Critical Review on the Sensing, Control, and Manipulation of Single Molecules on Optofluidic Devices," *Micromachines*, vol. 13, no. 6, p. 968, 2022, doi: 10.3390/mi13060968.

[99] J. J. Gooding and K. Gaus, "Single-Molecule Sensors: Challenges and Opportunities for Quantitative Analysis," *Angew. Chemie Int. Ed.*, vol. 55, no. 38, pp. 11354–11366, Sep. 2016, doi: 10.1002/ANIE.201600495.

[100] Y. L. Ying *et al.*, "Nanopore-based technologies beyond DNA sequencing," *Nat. Nanotechnol.*, vol. 17, no. 11, pp. 1136–1146, 2022, doi: 10.1038/s41565-022-01193-2.

[101] F. Rivas *et al.*, "Label-free analysis of physiological hyaluronan size distribution with a solid-state nanopore sensor," *Nat. Commun.*, vol. 9, no. 1, p. 1037, Mar. 2018, doi: 10.1038/s41467-018-03439-x.

[102] Y. Wang *et al.*, "Nanolock–Nanopore Facilitated Digital Diagnostics of Cancer Driver Mutation in Tumor Tissue," *ACS Sensors*, vol. 2, no. 7, pp. 975–981, Jul. 2017, doi: 10.1021/acssensors.7b00235.

[103] A. K. Thakur and L. Movileanu, "Single-molecule protein detection in a biofluid

using a quantitative nanopore sensor," *ACS Sensors*, vol. 4, no. 9, pp. 2320–2326, 2019, doi: 10.1021/acssensors.9b00848.

[104] Y. Wang, D. Zheng, Q. Tan, M. X. Wang, and L. Q. Gu, "Nanopore-based detection of circulating microRNAs in lung cancer patients," *Nat. Nanotechnol.*, vol. 6, no. 10, pp. 668–674, 2011, doi: 10.1038/nnano.2011.147.

[105] W. H. Pitchford *et al.*, "Synchronized Optical and Electronic Detection of Biomolecules Using a Low Noise Nanopore Platform," *ACS Nano*, vol. 9, no. 2, pp. 1740–1748, Feb. 2015, doi: 10.1021/nn506572r.

[106] E. Angeli *et al.*, "Simultaneous Electro-Optical Tracking for Nanoparticle Recognition and Counting," *Nano Lett.*, vol. 15, no. 9, pp. 5696–5701, Sep. 2015, doi: 10.1021/acs.nanolett.5b01243.

[107] D. V. Verschueren, S. Pud, X. Shi, L. De Angelis, L. Kuipers, and C. Dekker, "Label-Free Optical Detection of DNA Translocations through Plasmonic Nanopores," *ACS Nano*, vol. 13, no. 1, pp. 61–70, 2019, doi: 10.1021/acsnano.8b06758.

[108] P. Measor, S. Kühn, E. J. Lunt, B. S. Phillips, A. R. Hawkins, and H. Schmidt, "Multi-mode mitigation in an optofluidic chip for particle manipulation and sensing," *Opt. Express*, vol. 17, no. 26, p. 24342, 2009, doi: 10.1364/oe.17.024342.

[109] K. D. Leake, M. A. B. Olson, D. Ozcelik, A. R. Hawkins, and H. Schmidt,

"Spectrally reconfigurable integrated multi-spot particle trap," *Opt. Lett.*, vol. 40, no. 23, p. 5435, Dec. 2015, doi: 10.1364/OL.40.005435.

[110] S. Kühn *et al.*, "Loss-based optical trap for on-chip particle analysis," *Lab Chip*, vol. 9, no. 15, p. 2212, Aug. 2009, doi: 10.1039/b900555b.

[111] M. J. N. Sampad, H. Zhang, T. D. Yuzvinsky, M. A. Stott, A. R. Hawkins, and H. Schmidt, "Optical trapping assisted label-free and amplification-free detection of SARS-CoV-2 RNAs with an optofluidic nanopore sensor," *Biosens. Bioelectron.*, vol. 194, no. July, p. 113588, 2021, doi: 10.1016/j.bios.2021.113588.

[112] M. Rahman *et al.*, "On demand delivery and analysis of single molecules on a programmable nanopore-optofluidic device," *Nat. Commun.*, vol. 10, no. 1, p. 3712, Aug. 2019, doi: 10.1038/s41467-019-11723-7.

[113] D. Deamer, M. Akeson, and D. Branton, "Three decades of nanopore sequencing," *Nature Biotechnology*, vol. 34, no. 5. Nature Publishing Group, pp. 518–524, May 2016, doi: 10.1038/nbt.3423.

[114] M. Rahman, M. J. N. Sampad, A. Hawkins, and H. Schmidt, "Recent advances in integrated solid-state nanopore sensors," *Lab Chip*, vol. 21, no. 16, pp. 3030–3052, Aug. 2021, doi: 10.1039/D1LC00294E.

[115] M. Muthukumar, "Theory of capture rate in polymer translocation," *J. Chem. Phys.*, vol. 132, no. 19, p. 195101, May 2010, doi: 10.1063/1.3429882.

[116] A. Y. Grosberg and Y. Rabin, “DNA capture into a nanopore: Interplay of diffusion and electrohydrodynamics,” *J. Chem. Phys.*, vol. 133, no. 16, p. 165102, 2010, doi: 10.1063/1.3495481.

[117] A. Han *et al.*, “Label-free detection of single protein molecules and protein-protein interactions using synthetic nanopores,” *Anal. Chem.*, vol. 80, no. 12, pp. 4651–4658, Jun. 2008, doi: 10.1021/ac7025207.

[118] H. Yamazaki *et al.*, “Label-Free Single-Molecule Thermoscopy Using a Laser-Heated Nanopore,” *Nano Lett.*, vol. 17, no. 11, pp. 7067–7074, 2017, doi: 10.1021/acs.nanolett.7b03752.

[119] S. Rauf, L. Zhang, A. Ali, Y. Liu, and J. Li, “Label-Free Nanopore Biosensor for Rapid and Highly Sensitive Cocaine Detection in Complex Biological Fluids,” *ACS Sensors*, vol. 2, no. 2, pp. 227–234, 2017, doi: 10.1021/acssensors.6b00627.

[120] S. Zhou, L. Wang, X. Chen, and X. Guan, “Label-Free Nanopore Single-Molecule Measurement of Trypsin Activity,” *ACS Sensors*, vol. 1, no. 5, pp. 607–613, 2016, doi: 10.1021/acssensors.6b00043.

[121] J. J. Kasianowicz, E. Brandin, D. Branton, and D. W. Deamer, “Characterization of individual polynucleotide molecules using a membrane channel.,” *Proc. Natl. Acad. Sci. U. S. A.*, vol. 93, no. 24, pp. 13770–3, Nov. 1996, doi: 10.1073/pnas.93.24.13770.

[122] D. Branton and D. Deamer, *Nanopore Sequencing: An Introduction*. 2019.

[123] L. Song, M. R. Hobaugh, C. Shustak, S. Cheley, H. Bayley, and J. E. Gouaux, "Structure of staphylococcal α-hemolysin, a heptameric transmembrane pore," *Science (80-.).*, vol. 274, no. 5294, pp. 1859–1866, Dec. 1996, doi: 10.1126/science.274.5294.1859.

[124] A. H. Laszlo, I. M. Derrington, and J. H. Gundlach, "MspA nanopore as a single-molecule tool: From sequencing to SPRNT," *Methods*, vol. 105. pp. 75–89, 2016, doi: 10.1016/j.ymeth.2016.03.026.

[125] J. Clarke, H. C. Wu, L. Jayasinghe, A. Patel, S. Reid, and H. Bayley, "Continuous base identification for single-molecule nanopore DNA sequencing," *Nat. Nanotechnol. 2009 44*, vol. 4, no. 4, pp. 265–270, Feb. 2009, doi: 10.1038/nnano.2009.12.

[126] A. Meller, L. Nivon, E. Brandin, J. Golovchenko, and D. Branton, "Rapid nanopore discrimination between single polynucleotide molecules," *Proc. Natl. Acad. Sci. U. S. A.*, vol. 97, no. 3, pp. 1079–1084, 2000, doi: 10.1073/pnas.97.3.1079.

[127] S. Benner *et al.*, "Sequence-specific detection of individual DNA polymerase complexes in real time using a nanopore," *Nat. Nanotechnol.*, vol. 2, no. 11, pp. 718–724, 2007, doi: 10.1038/nnano.2007.344.

[128] L.-Q. Gu and J. W. Shim, "Single molecule sensing by nanopores and nanopore

devices," *Analyst*, vol. 135, no. 3, pp. 441–451, Feb. 2010, doi: 10.1039/B907735A.

[129] "Roche sequencing solutions." https://sequencing.roche.com/global/en/article-listing/nanopore-sequencing.html.

[130] "Oxford Nanopore Technologies." https://nanoporetech.com/.

[131] "Nabsys." https://nabsys.com/nanodetector/.

[132] W. Shi, A. K. Friedman, and L. A. Baker, "Nanopore Sensing," *Analytical Chemistry*, vol. 89, no. 1. American Chemical Society, pp. 157–188, Jan. 2017, doi: 10.1021/acs.analchem.6b04260.

[133] C. Dekker, "Solid-state nanopores," *Nat. Nanotechnol.*, vol. 2, pp. 209–215, 2007.

[134] L. Xue, H. Yamazaki, R. Ren, M. Wanunu, A. P. Ivanov, and J. B. Edel, "Solid-state nanopore sensors," *Nature Reviews Materials*, vol. 5, no. 12. Nature Research, pp. 931–951, Dec. 2020, doi: 10.1038/s41578-020-0229-6.

[135] J. Li, D. Stein, C. McMullan, D. Branton, M. J. Aziz, and J. A. Golovchenko, "Ion-beam sculpting at nanometre length scales," *Nature*, vol. 412, no. 6843, pp. 166–169, Jul. 2001, doi: 10.1038/35084037.

[136] A. J. Storm, J. H. Chen, X. S. Ling, H. W. Zandbergen, and C. Dekker, "Fabrication of solid-state nanopores with single-nanometre precision," *Nature*

Materials, vol. 2, no. 8. pp. 537–540, 2003, doi: 10.1038/nmat941.

[137] M. S. Khan and J. D. Williams, "Fabrication of solid state nanopore in thin silicon membrane using low cost multistep chemical etching," *Materials (Basel).*, vol. 8, no. 11, pp. 7389–7400, 2015, doi: 10.3390/ma8115390.

[138] H. Kwok, K. Briggs, and V. Tabard-Cossa, "Nanopore fabrication by controlled dielectric breakdown," *PLoS One*, vol. 9, no. 3, p. e92880, Mar. 2014, doi: 10.1371/journal.pone.0092880.

[139] M. Karhanek, J. T. Kemp, N. Pourmand, R. W. Davis, and C. D. Webb, "Single DNA molecule detection using nanopipettes and nanoparticles," *Nano Lett.*, vol. 5, no. 2, pp. 403–407, Feb. 2005, doi: 10.1021/nl0480464.

[140] J. K. Rosenstein, M. Wanunu, C. A. Merchant, M. Drndic, and K. L. Shepard, "Integrated nanopore sensing platform with sub-microsecond temporal resolution," *Nat. Methods*, vol. 9, no. 5, pp. 487–492, May 2012, doi: 10.1038/nmeth.1932.

[141] A. Ivankin, R. Y. Henley, J. Larkin, S. Carson, M. L. Toscano, and M. Wanunu, "Label-free optical detection of biomolecular translocation through nanopore arrays," *ACS Nano*, vol. 8, no. 10, pp. 10774–10781, Oct. 2014, doi: 10.1021/nn504551d.

[142] R. Tahvildari, E. Beamish, V. Tabard-Cossa, and M. Godin, "Integrating nanopore sensors within microfluidic channel arrays using controlled

breakdown," *Lab Chip*, vol. 15, no. 6, pp. 1407–1411, Mar. 2015, doi: 10.1039/c4lc01366b.

[143] D. Han, L. P. Zaino, K. Fu, and P. W. Bohn, "Redox Cycling in Nanopore-Confined Recessed Dual-Ring Electrode Arrays," *J. Phys. Chem. C*, vol. 120, no. 37, pp. 20634–20641, 2016, doi: 10.1021/acs.jpcc.6b01287.

[144] A. Arima *et al.*, "Selective detections of single-viruses using solid-state nanopores," *Sci. Rep.*, vol. 8, no. 1, p. 16305, Nov. 2018, doi: 10.1038/s41598-018-34665-4.

[145] C. Shasha, R. Y. Henley, D. H. Stoloff, K. D. Rynearson, T. Hermann, and M. Wanunu, "Nanopore-based conformational analysis of a viral RNA drug target," *ACS Nano*, vol. 8, no. 6, pp. 6425–6430, Jun. 2014, doi: 10.1021/nn501969r.

[146] S. W. Kowalczyk, M. W. Tuijtel, S. P. Donkers, and C. Dekker, "Unraveling single-stranded DNA in a solid-state nanopore," *Nano Lett.*, vol. 10, no. 4, pp. 1414–1420, 2010, doi: 10.1021/nl100271c.

[147] L. Zhan, T. Jin, J. Zhou, W. Xu, Y. Chen, and R. Mezzenga, "Fast Probing Amyloid Polymorphism via Nanopore Translocation," *Nano Lett.*, vol. 23, no. 21, pp. 9912–9919, 2023, doi: 10.1021/acs.nanolett.3c02860.

[148] C. C. Chien, S. Shekar, D. J. Niedzwiecki, K. L. Shepard, and M. Drndić, "Single-Stranded DNA Translocation Recordings through Solid-State Nanopores on Glass Chips at 10 MHz Measurement Bandwidth," *ACS Nano*,

vol. 13, no. 9, pp. 10545–10554, Sep. 2019, doi: 10.1021/acsnano.9b04626.

[149] W. Li *et al.*, "Single protein molecule detection by glass nanopores," *ACS Nano*, vol. 7, no. 5, pp. 4129–4134, 2013, doi: 10.1021/nn4004567.

[150] D. Fologea, M. Gershow, B. Ledden, D. S. McNabb, J. A. Golovchenko, and J. Li, "Detecting single stranded DNA with a solid state nanopore," *Nano Lett.*, vol. 5, no. 10, pp. 1905–1909, Oct. 2005, doi: 10.1021/nl051199m.

[151] M. I. Rudenko *et al.*, "Controlled gating and electrical detection of single 50S ribosomal subunits through a solid-state nanopore in a microfluidic chip," *Biosens. Bioelectron.*, vol. 29, no. 1, pp. 34–39, Nov. 2011, doi: 10.1016/j.bios.2011.07.047.

[152] M. R. Holmes, T. Shang, A. R. Hawkins, M. Rudenko, P. Measor, and H. Schmidt, "Micropore and nanopore fabrication in hollow antiresonant reflecting optical waveguides.," *J. Micro. Nanolithogr. MEMS. MOEMS*, vol. 9, no. 2, p. 23004, 2010, doi: 10.1117/1.3378152.

[153] Z. Walker, T. Wells, K. Lay, M. J. N. Sampad, H. Schmidt, and A. Hawkins, "Solid-state membranes formed on natural menisci," *Nanotechnology*, vol. 31, no. 44, p. 445303, Oct. 2020, doi: 10.1088/1361-6528/aba711.

[154] Z. J. Walker *et al.*, "Optofluidic Particle Manipulation Platform with Nanomembrane," *Micromachines*, vol. 13, no. 5, p. 721, 2022, doi: 10.3390/mi13050721.

[155] Z. J. Walker *et al.*, "Optofluidic Particle Manipulation: Optical Trapping in a Thin-Membrane Microchannel," *Biosensors*, vol. 12, no. 9, p. 690, Aug. 2022, doi: 10.3390/bios12090690.

[156] A. Ashkin, "Optical trapping and manipulation of neutral particles using lasers," *Proc. Natl. Acad. Sci. U. S. A.*, vol. 94, no. 10, pp. 4853–4860, 1997, doi: 10.1073/pnas.94.10.4853.

[157] D. G. Grier, "A revolution in optical manipulation," *Nature*, vol. 424, no. 6950. pp. 810–816, 2003, doi: 10.1038/nature01935.

[158] M. M. Rahman, "Nanopore Optofluidic Devices for Single Molecule Analysis and Manipulation," 2019.

[159] J. Li and D. S. Talaga, "The distribution of DNA translocation times in solid-state nanopores," *J. Phys. Condens. Matter*, vol. 22, no. 45, p. 454129, Nov. 2010, doi: 10.1088/0953-8984/22/45/454129.

[160] Y. Pan, D. Zhang, P. Yang, L. L. M. Poon, and Q. Wang, "Viral load of SARS-CoV-2 in clinical samples," *The Lancet Infectious Diseases*, vol. 20, no. 4. pp. 411–412, 2020, doi: 10.1016/S1473-3099(20)30113-4.

[161] J. W. Parks *et al.*, "Integration of programmable microfluidics and on-chip fluorescence detection for biosensing applications," *Biomicrofluidics*, vol. 8, no. 5, p. 054111, Sep. 2014, doi: 10.1063/1.4897226.

[162] H. Cai, M. A. Stott, D. Ozcelik, J. W. Parks, A. R. Hawkins, and H. Schmidt,

"On-chip wavelength multiplexed detection of cancer DNA biomarkers in blood," *Biomicrofluidics*, vol. 10, no. 6, p. 064116, Nov. 2016, doi: 10.1063/1.4968033.

[163] H. C. Berg, *Random Walks in Biology*. Princeton University Press, 1993.

[164] B. Lu *et al.*, "Pressure-controlled motion of single polymers through solid-state nanopores," *Nano Lett.*, vol. 13, no. 7, pp. 3048–3052, Jul. 2013, doi: 10.1021/nl402052v.

[165] M. Wanunu, W. Morrison, Y. Rabin, A. Y. Grosberg, and A. Meller, "Electrostatic focusing of unlabelled DNA into nanoscale pores using a salt gradient," *Nat. Nanotechnol.*, vol. 5, no. 2, pp. 160–165, 2010, doi: 10.1038/nnano.2009.379.

[166] F. Nicoli, D. Verschueren, M. Klein, C. Dekker, and M. P. Jonsson, "DNA translocations through solid-state plasmonic nanopores," *Nano Lett.*, vol. 14, no. 12, pp. 6917–6925, 2014, doi: 10.1021/nl503034j.

[167] K. J. Freedman, L. M. Otto, A. P. Ivanov, A. Barik, S.-H. Oh, and J. B. Edel, "Nanopore sensing at ultra-low concentrations using single-molecule dielectrophoretic trapping," *Nat. Commun.*, vol. 7, no. 1, p. 10217, Jan. 2016, doi: 10.1038/ncomms10217.

[168] J. D. Spitzberg, X. F. van Kooten, M. Bercovici, and A. Meller, "Microfluidic device for coupling isotachophoretic sample focusing with nanopore single-

molecule sensing," *Nanoscale*, vol. 12, no. 34, pp. 17805–17811, 2020, doi: 10.1039/D0NR05000H.

[169] M. Rahman *et al.*, "Optical trapping assisted detection rate enhancement of single molecules on a nanopore optofluidic chip," *Optica*, vol. 6, no. 9, p. 1130, Sep. 2019, doi: 10.1364/OPTICA.6.001130.

[170] W. R. de Araujo, H. Lukas, M. D. T. Torres, W. Gao, and C. de la Fuente-Nunez, "Low-Cost Biosensor Technologies for Rapid Detection of COVID-19 and Future Pandemics," *ACS Nano*, vol. 18, no. 3, pp. 1757–1777, Jan. 2024, doi: 10.1021/acsnano.3c01629.

[171] R. Samson, G. R. Navale, and M. S. Dharne, "Biosensors: frontiers in rapid detection of COVID-19," *3 Biotech*, vol. 10, no. 385. 2020, doi: 10.1007/s13205-020-02369-0.

[172] Y. Zhou, L. Zhang, Y. H. Xie, and J. Wu, "Advancements in detection of SARS-CoV-2 infection for confronting COVID-19 pandemics," *Lab. Investig.*, vol. 102, no. 1, pp. 4–13, 2022, doi: 10.1038/s41374-021-00663-w.

[173] N. N. Y. Tsang, H. C. So, K. Y. Ng, B. J. Cowling, G. M. Leung, and D. K. M. Ip, "Diagnostic performance of different sampling approaches for SARS-CoV-2 RT-PCR testing: a systematic review and meta-analysis," *Lancet Infect. Dis.*, vol. 21, no. 9, pp. 1233–1245, 2021, doi: 10.1016/S1473-3099(21)00146-8.

[174] T. Pinheiro *et al.*, "Paper-Based Biosensors for COVID-19: A Review of

Innovative Tools for Controlling the Pandemic," *ACS Omega*, vol. 6, no. 44. pp. 29268–29290, 2021, doi: 10.1021/acsomega.1c04012.

[175] R. Nouri, Y. Jiang, Z. Tang, X. L. Lian, and W. Guan, "Detection of SARS-CoV-2 with Solid-State CRISPR-Cas12a-Assisted Nanopores," *Nano Lett.*, vol. 21, no. 19, pp. 8393–8400, 2021, doi: 10.1021/acs.nanolett.1c02974.

[176] L. Liu *et al.*, "Gold Nanoparticle-Labeled CRISPR-Cas13a Assay for the Sensitive Solid-State Nanopore Molecular Counting," *Adv. Mater. Technol.*, vol. 7, no. 3, pp. 1–9, 2022, doi: 10.1002/admt.202101550.

[177] R. Pu *et al.*, "The screening value of RT-LAMP and RT-PCR in the diagnosis of COVID-19: systematic review and meta-analysis," *J. Virol. Methods*, vol. 300, p. 114392, 2022, doi: 10.1016/j.jviromet.2021.114392.

[178] Z. Tang *et al.*, "Rapid detection of novel coronavirus SARS-CoV-2 by RT-LAMP coupled solid-state nanopores," *Biosens. Bioelectron.*, vol. 197, p. 113759, 2022, doi: 10.1016/j.bios.2021.113759.

[179] M. De Felice, M. De Falco, D. Zappi, A. Antonacci, and V. Scognamiglio, "Isothermal amplification-assisted diagnostics for COVID-19," *Biosensors and Bioelectronics*, vol. 205. p. 114101, 2022, doi: 10.1016/j.bios.2022.114101.

[180] M. M. Islam and D. Koirala, "Toward a next-generation diagnostic tool: A review on emerging isothermal nucleic acid amplification techniques for the detection of SARS-CoV-2 and other infectious viruses," *Anal. Chim. Acta*, vol.

1209, p. 339338, 2022, doi: 10.1016/j.aca.2021.339338.

[181] Z. Zhang *et al.*, "Multiplex quantitative detection of SARS-CoV-2 specific IgG and IgM antibodies based on DNA-assisted nanopore sensing," *Biosens. Bioelectron.*, vol. 181, p. 113134, 2021, doi: 10.1016/j.bios.2021.113134.

[182] E. Valera *et al.*, "COVID-19 Point-of-Care Diagnostics: Present and Future," *ACS Nano*, vol. 15, no. 5, pp. 7899–7906, 2021, doi: 10.1021/acsnano.1c02981.

[183] A. S. Fauci and D. M. Morens, "The Perpetual Challenge of Infectious Diseases," *N. Engl. J. Med.*, vol. 366, no. 5, pp. 454–461, 2012, doi: 10.1056/nejmra1108296.

[184] "Infectious diseases kill over 17 million people a year: WHO warns of global crisis," *https://www.who.int/news/item/01-01-1996-infectious-diseases-kill-over-17-million-people-a-year-who-warns-of-global-crisis*. https://www.who.int/news/item/01-01-1996-infectious-diseases-kill-over-17-million-people-a-year-who-warns-of-global-crisis.

[185] B. S. Graham and N. J. Sullivan, "Emerging viral diseases from a vaccinology perspective: Preparing for the next pandemic," *Nat. Immunol.*, vol. 19, no. 1, pp. 20–28, 2018, doi: 10.1038/s41590-017-0007-9.

[186] D. Malvy, A. K. McElroy, H. de Clerck, S. Günther, and J. van Griensven, "Ebola virus disease," *Lancet*, vol. 393, no. 10174, pp. 936–948, Mar. 2019, doi: 10.1016/S0140-6736(18)33132-5.

[187] M. T. Osterholm, “Ebola and Zika: Cautionary tales,” *Science (80-.).*, vol. 353, no. 6304, pp. 1073–1073, Sep. 2016, doi: 10.1126/science.aai9078.

[188] “WHO Coronavirus (COVID-19) Dashboard,” *https://covid19.who.int/*. https://covid19.who.int/.

[189] H. Harpaldas, S. Arumugam, C. Campillo Rodriguez, B. A. Kumar, V. Shi, and S. K. Sia, “Point-of-care diagnostics: Recent developments in a pandemic age,” *Lab on a Chip*, vol. 21, no. 23. Royal Society of Chemistry, pp. 4517–4548, Nov. 25, 2021, doi: 10.1039/d1lc00627d.

[190] N. Pardi and D. Weissman, “Development of vaccines and antivirals for combating viral pandemics,” *Nat. Biomed. Eng.*, vol. 4, no. 12, pp. 1128–1133, Dec. 2020, doi: 10.1038/s41551-020-00658-w.

[191] D. K. Singh *et al.*, “Responses to acute infection with SARS-CoV-2 in the lungs of rhesus macaques, baboons and marmosets,” *Nat. Microbiol.*, vol. 6, no. 1, pp. 73–86, 2021, doi: 10.1038/s41564-020-00841-4.

[192] O. Faye, O. Faye, D. Diallo, M. Diallo, M. Weidmann, and A. A. Sall, “Quantitative real-time PCR detection of Zika virus and evaluation with field-caught Mosquitoes,” *Virol. J.*, vol. 10, no. 1, p. 311, Oct. 2013, doi: 10.1186/1743-422X-10-311/TABLES/5.

[193] L. Barzon *et al.*, “Infection dynamics in a traveller with persistent shedding of Zika virus RNA in semen for six months after returning from Haiti to Italy,

January 2016," *Eurosurveillance*, vol. 21, no. 32, p. 30316, Aug. 2016, doi: 10.2807/1560-7917.ES.2016.21.32.30316.

[194] A. Natarajan *et al.*, "Gastrointestinal symptoms and fecal shedding of SARS-CoV-2 RNA suggest prolonged gastrointestinal infection," *Med*, vol. 3, no. 6, pp. 371–387, Jun. 2022, doi: 10.1016/j.medj.2022.04.001.

[195] M. Huch and B. K. Koo, "Modeling mouse and human development using organoid cultures," *Development (Cambridge)*, vol. 142, no. 18. pp. 3113–3125, 2015, doi: 10.1242/dev.118570.

[196] P. Saglam-Metiner, E. Yildirim, C. Dincer, O. Basak, and O. Yesil-Celiktas, "Humanized brain organoids-on-chip integrated with sensors for screening neuronal activity and neurotoxicity," *Microchim. Acta*, vol. 191, no. 1, p. 71, Jan. 2024, doi: 10.1007/s00604-023-06165-4.

[197] E. Jeong, S. Choi, and S. W. Cho, "Recent Advances in Brain Organoid Technology for Human Brain Research," *ACS Applied Materials and Interfaces*, vol. 15, no. 1. pp. 200–219, 2023, doi: 10.1021/ACSAMI.2C17467.

[198] J. Kim, B. K. Koo, and J. A. Knoblich, "Human organoids: model systems for human biology and medicine," *Nature Reviews Molecular Cell Biology*, vol. 21, no. 10. pp. 571–584, 2020, doi: 10.1038/s41580-020-0259-3.

[199] M. Mathieu, L. Martin-Jaular, G. Lavieu, and C. Théry, "Specificities of secretion and uptake of exosomes and other extracellular vesicles for cell-to-cell

communication," *Nature Cell Biology*, vol. 21, no. 1. pp. 9–17, 2019, doi: 10.1038/s41556-018-0250-9.

[200] M. Yáñez-Mó *et al.*, "Biological properties of extracellular vesicles and their physiological functions," *Journal of Extracellular Vesicles*, vol. 4, no. 2015. pp. 1–60, 2015, doi: 10.3402/jev.v4.27066.

[201] H. Valadi, K. Ekström, A. Bossios, M. Sjöstrand, J. J. Lee, and J. O. Lötvall, "Exosome-mediated transfer of mRNAs and microRNAs is a novel mechanism of genetic exchange between cells," *Nat. Cell Biol.*, vol. 9, no. 6, pp. 654–659, 2007, doi: 10.1038/ncb1596.

[202] G. van Niel, D. R. F. Carter, A. Clayton, D. W. Lambert, G. Raposo, and P. Vader, "Challenges and directions in studying cell–cell communication by extracellular vesicles," *Nat. Rev. Mol. Cell Biol.*, vol. 23, no. 5, pp. 369–382, 2022, doi: 10.1038/s41580-022-00460-3.

[203] I. Tatischeff, "Extracellular Vesicle-DNA: The Next Liquid Biopsy Biomarker for Early Cancer Diagnosis?," *Cancers*, vol. 15, no. 5. p. 1456, 2023, doi: 10.3390/cancers15051456.

[204] W. Yu *et al.*, "Exosome-based liquid biopsies in cancer: opportunities and challenges," *Annals of Oncology*, vol. 32, no. 4. pp. 466–477, 2021, doi: 10.1016/j.annonc.2021.01.074.

[205] À. Díaz-Ramos, A. Roig-Borrellas, A. García-Melero, and R. López-Alemany,

"α-enolase, a multifunctional protein: Its role on pathophysiological situations," *J. Biomed. Biotechnol.*, vol. 2012, p. 156795, 2012, doi: 10.1155/2012/156795.

[206] M. Principe *et al.*, "Alpha-enolase (ENO1) controls alpha v/beta 3 integrin expression and regulates pancreatic cancer adhesion, invasion, and metastasis," *J. Hematol. Oncol.*, vol. 10, no. 1, pp. 1–13, 2017, doi: 10.1186/s13045-016-0385-8.

[207] K. Jiang *et al.*, "Exosome-derived ENO1 regulates integrin α6β4 expression and promotes hepatocellular carcinoma growth and metastasis," *Cell Death Dis.*, vol. 11, no. 11, p. 972, 2020, doi: 10.1038/s41419-020-03179-1.

[208] G. Raposo and W. Stoorvogel, "Extracellular vesicles: Exosomes, microvesicles, and friends," *Journal of Cell Biology*, vol. 200, no. 4. pp. 373–383, 2013, doi: 10.1083/jcb.201211138.

[209] E. van der Pol, A. N. Böing, P. Harrison, A. Sturk, and R. Nieuwland, "Classification, functions, and clinical relevance of extracellular vesicles," *Pharmacol. Rev.*, vol. 64, no. 3, pp. 676–705, 2012, doi: 10.1124/pr.112.005983.

[210] M. Li, L. Huang, J. Chen, F. Ni, Y. Zhang, and F. Liu, "Isolation of Exosome Nanoparticles from Human Cerebrospinal Fluid for Proteomic Analysis," *ACS Appl. Nano Mater.*, vol. 4, no. 4, pp. 3351–3359, 2021, doi: 10.1021/acsanm.0c02622.

[211] J. M. Lee, E. Garon, and D. T. Wong, "Salivary diagnostics," *Orthod.*

Craniofacial Res., vol. 12, no. 3, pp. 206–211, 2009, doi: 10.1111/j.1601-6343.2009.01454.x.

[212] H. Wei *et al.*, "Regulation of exosome production and cargo sorting," *Int. J. Biol. Sci.*, vol. 17, no. 1, pp. 163–177, 2020, doi: 10.7150/ijbs.53671.

[213] M. C. Deregibus *et al.*, "Charge-based precipitation of extracellular vesicles," *Int. J. Mol. Med.*, vol. 38, no. 5, pp. 1359–1366, 2016, doi: 10.3892/ijmm.2016.2759.

[214] G. Midekessa *et al.*, "Zeta Potential of Extracellular Vesicles: Toward Understanding the Attributes that Determine Colloidal Stability," *ACS Omega*, vol. 5, no. 27, pp. 16701–16710, 2020, doi: 10.1021/acsomega.0c01582.

[215] B. J. Tauro *et al.*, "Comparison of ultracentrifugation, density gradient separation, and immunoaffinity capture methods for isolating human colon cancer cell line LIM1863-derived exosomes," *Methods*, vol. 56, no. 2, pp. 293–304, 2012, doi: 10.1016/j.ymeth.2012.01.002.

[216] J. C. Contreras-Naranjo, H. J. Wu, and V. M. Ugaz, "Microfluidics for exosome isolation and analysis: Enabling liquid biopsy for personalized medicine," *Lab on a Chip*, vol. 17, no. 21. pp. 3558–3577, 2017, doi: 10.1039/c7lc00592j.

[217] B. H. Wunsch *et al.*, "Nanoscale lateral displacement arrays for the separation of exosomes and colloids down to 20nm," *Nat. Nanotechnol.*, vol. 11, no. 11, pp. 936–940, 2016, doi: 10.1038/nnano.2016.134.

[218] K. Lee, H. Shao, R. Weissleder, and H. Lee, “Acoustic purification of extracellular microvesicles,” *ACS Nano*, vol. 9, no. 3, pp. 2321–2327, 2015, doi: 10.1021/nn506538f.

[219] M. Zhang *et al.*, “Methods and Technologies for Exosome Isolation and Characterization,” *Small Methods*, vol. 2, no. 9. p. 1800021, 2018, doi: 10.1002/smtd.201800021.

[220] Y. Wan *et al.*, “Rapid magnetic isolation of extracellular vesicles via lipid-based nanoprobes,” *Nat. Biomed. Eng.*, vol. 1, no. 0058, 2017, doi: 10.1038/s41551-017-0058.

[221] Z. Song, J. Mao, R. A. Barrero, P. Wang, F. Zhang, and T. Wang, “Development of a cd63 aptamer for efficient cancer immunochemistry and immunoaffinity-based exosome isolation,” *Molecules*, vol. 25, no. 23, p. 5585, 2020, doi: 10.3390/molecules25235585.

[222] R. A. Dragovic *et al.*, “Sizing and phenotyping of cellular vesicles using Nanoparticle Tracking Analysis,” *Nanomedicine Nanotechnology, Biol. Med.*, vol. 7, no. 6, pp. 780–788, 2011, doi: 10.1016/j.nano.2011.04.003.

[223] P. Carnell-Morris, D. Tannetta, A. Siupa, P. Hole, and R. Dragovic, “Analysis of Extracellular Vesicles Using Fluorescence Nanoparticle Tracking Analysis,” *Methods Mol. Biol.*, vol. 1660, pp. 153–173, 2017, doi: 10.1007/978-1-4939-7253-1_13.

[224] D. Bachurski *et al.*, “Extracellular vesicle measurements with nanoparticle tracking analysis–An accuracy and repeatability comparison between NanoSight NS300 and ZetaView,” *J. Extracell. Vesicles*, vol. 8, no. 1, p. 1596016, 2019, doi: 10.1080/20013078.2019.1596016.

[225] J. Ko, E. Carpenter, and D. Issadore, “Detection and isolation of circulating exosomes and microvesicles for cancer monitoring and diagnostics using micro-/nano-based devices,” *Analyst*, vol. 141, no. 2. pp. 450–460, 2016, doi: 10.1039/c5an01610j.

[226] T. Young and S. C. Jacobson, “Characterization of Extracellular Vesicles by Resistive-Pulse Sensing on In-Plane Multipore Nanofluidic Devices,” 2021.

[227] F. A. W. Coumans *et al.*, “Reproducible extracellular vesicle size and concentration determination with tunable resistive pulse sensing,” *J. Extracell. Vesicles*, vol. 3, no. 1, p. 25922, 2014, doi: 10.3402/jev.v3.25922.

[228] J. L. Fraikin, T. Teesalu, C. M. McKenney, E. Ruoslahti, and A. N. Cleland, “A high-throughput label-free nanoparticle analyser,” *Nat. Nanotechnol.*, vol. 6, no. 5, pp. 308–313, 2011, doi: 10.1038/nnano.2011.24.

[229] S. Ryuzaki *et al.*, “Rapid Discrimination of Extracellular Vesicles by Shape Distribution Analysis,” *Anal. Chem.*, vol. 93, no. 18, pp. 7037–7044, 2021, doi: 10.1021/acs.analchem.1c00258.

[230] S. Vaidyanathan *et al.*, “High Sensitivity Extended Nano-Coulter Counter for

Detection of Viral Particles and Extracellular Vesicles," *Anal. Chem.*, vol. 95, no. 26, 2023, doi: 10.1021/acs.analchem.3c00855.

[231] F. Momen-Heravi *et al.*, "Current methods for the isolation of extracellular vesicles," *Biological Chemistry*, vol. 394, no. 10. pp. 1253–1262, 2013, doi: 10.1515/hsz-2013-0141.

[232] M. Rahman, M. A. Stott, Y. Li, A. R. Hawkins, and H. Schmidt, "Single-particle analysis with 2D electro-optical trapping on an integrated optofluidic device," *Optica*, vol. 5, no. 10, p. 1311, 2018, doi: 10.1364/optica.5.001311.

[233] A. Faria-Pereira, M. Temido-Ferreira, and V. A. Morais, "BrainPhys Neuronal Media Support Physiological Function of Mitochondria in Mouse Primary Neuronal Cultures," *Front. Mol. Neurosci.*, vol. 15, 2022, doi: 10.3389/fnmol.2022.837448.

[234] C. Bardy *et al.*, "Neuronal medium that supports basic synaptic functions and activity of human neurons in vitro," *Proc. Natl. Acad. Sci. U. S. A.*, vol. 112, no. 20, pp. E2725–E2734, 2015, doi: 10.1073/pnas.1504393112.

[235] A. A. Pollen *et al.*, "Establishing Cerebral Organoids as Models of Human-Specific Brain Evolution," *Cell*, vol. 176, no. 4, pp. 743-756.e17, 2019, doi: 10.1016/j.cell.2019.01.017.

[236] A. Bhaduri *et al.*, "Cell stress in cortical organoids impairs molecular subtype specification," *Nature*, vol. 578, no. 7793, pp. 142–148, 2020, doi:

10.1038/s41586-020-1962-0.

[237] D. Ozcelik *et al.*, “Signal-to-noise enhancement in optical detection of single viruses with multispot excitation,” *IEEE J. Sel. Top. Quantum Electron.*, vol. 22, no. 4, pp. 6–11, 2016, doi: 10.1109/JSTQE.2015.2503321.

[238] M. N. Amin, V. Ganjalizadeh, M. Hamblin, A. R. Hawkins, and H. Schmidt, “Free-Space Excitation of Optofluidic Devices for Pattern-Based Single Particle Detection,” *IEEE Photonics Technol. Lett.*, vol. 33, no. 16, pp. 884–887, Aug. 2021, doi: 10.1109/LPT.2021.3069673.

[239] T. Wells, H. Schmidt, and A. Hawkins, “Nano/microfluidic device for high-throughput passive trapping of nanoparticles,” *Biomicrofluidics*, vol. 17, no. 6, p. 064101, Dec. 2023, doi: 10.1063/5.0176323.